THE UNIVERSITY OF OKLAHOMA

GRADUATE COLLEGE

MAGNETIC SUSCEPTIBILITIES OF PARAMAGNETIC IONS IN HOST CRYSTALS

A DISSERTATION

SUBMITTED TO THE GRADUATE FACULTY

in partial fulfillment of the requirements for the

degree of

DOCTOR OF PHILOSOPHY

BY

WILLIAM HARRY BRUMAGE

Norman, Oklahoma

1964

MAGNETIC SUSCEPTIBILITIES OF PARAMAGNETIC

IONS IN HOST CRYSTALS

APPROVED BY

Charles C. Torrance

Sylvan Brocerme

J. Rud Nielsen

Robert M. St. John

William N. Tuffy

DISSERTATION COMMITTEE

ACKNOWLEDGEMENTS

The author wishes to express his sincere appreciation to Professor Chun C. Lin for suggesting the research problems considered in this work and for his many enlightening discussions on the experimental and theoretical aspects of the problems.

It is also a pleasure to acknowledge Professor J. H. Van Vleck for suggesting the garnet problem, Professor C. R. Quade for his theoretical work on the vanadium crystals, and Mr. E. E. Sanmann for his work on the cobalt crystal.

Thanks are due Professor D. S. McClure for furnishing the vanadium crystals; Dr. T. L. Estle, Dr. M. DeWit, and Dr. H. A. Weakliem for supplying the cobalt and nickel crystals; Professor R. V. Jones for supplying the garnet crystals; and Mr. C. F. Dorman, Mr. C. R. Yarger, and Mr. E. C. Segraves for their assistance in the magnetic measurements and the computer work.

It is also desirable to express appreciation for the constant encouragement received from my wife, Audrey, and from Professor H. E. Ruff.

TABLE OF CONTENTS

LIST OF TABLES

LIST OF ILLUSTRATIONS

MAGNETIC SUSCEPTIBILITIES OF PARAMAGNETIC IONS IN HOST CRYSTALS

By William Harry Brumage

Major Professor: Dr. Chun C. Lin

A Faraday balance and a torsion balance have been constructed to measure the magnetic susceptibilities and the magnetic anisotropy of host crystals which have been doped with small amounts of paramagnetic ions. The magnetic susceptibilities have been measured, along and perpendicular to the trigonal axis, over the temperature range from 5.7 to 1100°K that is appropriate to each crystal.

Theoretical expressions for the magnetic susceptibilities as functions of temperature are obtained by employing the crystal-field theory. By using the magnetic data of $V^{3+}:Al_2O_3$, in conjunction with the ESR and optical data, the zero field splitting of the ground $^3A_2$ level is found to be 8.4 cm^{-1} while the trigonal field splitting of the ground state $^3T_1$ is 1100 cm^{-1}. From the ratio of the slopes of the graphs for χ, it is found that $g_\perp = 1.72$. The spin-orbit coupling constant is estimated to be about 95 cm^{-1} and the two trigonal field parameters are also estimated and compared with the point charge calculations.

The first two excited levels of Ni^{2+}:ZnO (160 and 260 cm^{-1}) and Ni^{2+}:CdS (230 and 240 cm^{-1}) are determined from the Van Vleck temperature independent susceptibilities. The spin orbit coupling constant for the nickel ion in both ZnO and CdS is reduced by about 50%. The two trigonal field parameters, as determined from experiment, are found to be in reasonable agreement with point charge calculations if small displacements of the ions are considered.

The magnetic data indicate a zero field splitting of 4 ± 0.3 cm^{-1} for cobalt doped zinc oxide. Calculations of the spin-orbit coupling constant show that it is reduced by about 40% from the free ion value. Values of the trigonal field parameters are estimated. Discrepancies between the magnetic susceptibility data and ESR data are discussed.

The paramagnetic susceptibility of ytterbium gallium garnet (YbGaG) is utilized to determine the splittings of the $^2F_{7/2}$ level. From the Van Vleck temperature independent susceptibility it is inferred that the Γ_8 level lies about 515 cm^{-1} above the Γ_7 level. From these measurements it is also estimated that the Γ_6 level lies about 800 cm^{-1} above the Γ_7 level. High precision cannot be claimed for the Γ_6 level as the analysis of the magnetic data is made on the assumption of a perfectly cubic crystalline field.

MAGNETIC SUSCEPTIBILITIES OF PARAMAGNETIC IONS IN HOST CRYSTALS

CHAPTER I

INTRODUCTION

In the study of transition elements in different host crystals there are several experimental methods that can be utilized to determine such quantities as energy levels, g-factors, crystal field parameters, and spin-orbit coupling constants. Electron Spin Resonance (ESR) data[1], when they can be obtained, are most useful in the study of the lowest lying levels and are particularly suited for determination of the g-factors and the energy level splittings of the ground state in a magnetic field. Optical absorption spectra[2] can be used to determine the higher lying levels between about 2000 cm^{-1} and 30,000 cm^{-1}. The cubic field parameter, the Slater-Condon parameters, and in some cases the spin-orbit coupling constants can be estimated quite well. Magnetic susceptibility[3,4] studies in conjunction with ESR and optical data are useful in energy level determinations intermediate between those obtainable from ESR and optical techniques. In certain cases it is also possible to obtain such quantities as the ratio of

the g-factors, the trigonal field parameters, and the spin orbit coupling constant.

The study of doped crystals increased rapidly in the 1950's with the advent of many new techniques for growing very pure single crystals and for doping these crystals with controlled amounts of impurities. While the major emphasis has been on ESR studies of these impurities it has been found advantageous to make use of other data to arrive at a more complete description of the impurity ion in the crystal. Magnetic susceptibility measurements along with optical studies have proven to be one of the major tools in implementing the knowledge gained through the use of the ESR data.

Crystal field theory[2,4] has been utilized in the interpretation of many of the results and, while it does have some deficiencies, it has proven to be a very useful model in giving a rather simple explanation of the experimental results. This theory along with the quantum mechanical treatment of the magnetic susceptibility by Van Vleck[3] is used in these studies.

The approach that will be used corresponds to the so-called weak-field approximation in which the electrostatic energy between the electrons of the impurity ion is included in the unperturbed Hamiltonian (H_o) of the free ion and in which the interaction between different configurations has been neglected.[2,4] The classical Hamiltonian H_o is given by

$$H_o = \sum_{i=1}^{n} \left[(\vec{p}_i^{\,2}/2m) - (Ze^2/r_i) \right] + \sum_{i<j}^{n} (e^2/r_{ij}) \qquad (I\text{-}1)$$

where $\vec{p}_i$ is the momentum of the ith electron, m the mass of the electron, -e its charge, r_i its distance from the nucleus, Ze the charge of the nucleus, and r_{ij} the distance from the ith to the jth electron.

The electron has a magnetic moment $\vec{\mu}$ which has a magnitude of $\frac{eh}{4\pi mc}$. $\vec{\mu}$ is found to be proportional to the spin angular momentum $\vec{s}$ where

$$\vec{\mu} = -(e/mc)\ \vec{s}\ .$$

Because of the relative motion of the electron and the nucleus it is found that there is a coupling between the orbital angular momentum $\vec{l}$ of the electron and its spin $\vec{s}$ given by $\xi(r)\ \vec{l}_i \cdot \vec{s}_i$. For several electrons this is given by[4]

$$H_{so} = \sum_{i=1}^{n} \xi(r)\vec{l}_i \cdot \vec{s}_i \qquad \text{(I-2)}$$

For Russell-Saunders coupling this expression can be written approximately as

$$H_{so} = \lambda \vec{L} \cdot \vec{S}$$

where the radial integration has already been included in λ.

For an ion in a crystal it will be assumed that the potential energy of the ith electron can be decomposed into two terms[2] corresponding to the cubic potential and trigonal potential, i.e.,

$$V(\vec{r}_i) = (V_i)_c + (V_i)_t, \qquad \text{(I-3)}$$

where V_t is much smaller than V_c and V_c, as an operator, commutes with the elements of the cubic group (O_h or T_d). The surrounding ions of the crystal are considered to be point charges and, since the electrostatic potential obeys Laplace's equation, $V(\vec{r}_i)$ can be expanded in terms of the generalized Legendre polynomials which are solutions of the Laplace equation[1], hence

$$V(\vec{r}) = \sum_n \sum_{m=n}^{-n} \sum_k A_n^m \, r_k^n \, Y_n^m \, (\theta_k, \varphi_k). \qquad \text{(I-4)}$$

For d electrons the triangle rule of spherical harmonics rules out $n > 4$ and inversion symmetry rules out odd n. For $n = 0$ the term is a constant and will shift all levels in a given configuration by the same amount. Since only relative energies are significant for the magnetic properties it will be neglected. For the iron group only $n = 2$ and $n = 4$ need be considered. This leads to

$$V_c = \sum_{i=1}^{n} A_4^o r_i^4 \left\{ Y_4^o(\theta_i, \varphi_i) + (10/7)^{\frac{1}{2}} \left[Y_4^3(\theta_i, \varphi_i) - Y_4^{-3}(\theta_i, \varphi_i) \right] \right\} \qquad \text{(I-5)}$$

and

$$V_t = \sum_{i=1}^{n} \left[B_2^o r_i^2 \, Y_2^o(\theta_i, \varphi_i) + B_4^o r_i^4 \, Y_4^o(\theta_i, \varphi_i) \right] \qquad \text{(I-6)}$$

with the z axis along the crystal C axis.

The magnetic interaction of an external magnetic field with the orbital and spin magnetic moments of the

electron is given by

$$H_m = -\vec{\mu}\cdot\vec{H} = \mu_o|\vec{l} + g_s\vec{s}|\cdot\vec{H} \qquad \text{(I-7)}$$

and can be easily obtained by writing the Hamiltonian in the presence of a magnetic field as[4]

$$H = H_1 + \sum_{i=1}^{n}\Big\{(1/2m)(\vec{p}_i + e\vec{A}_i/c)^2 - (1/2m)(\vec{p}_i)^2 + (e/mc)\vec{s}_i\cdot\vec{H}$$

$$+ (e/c)\xi(r_i)\vec{r}_i \times \vec{A}_i\cdot\vec{s}_i\Big\} \qquad \text{(I-8)}$$

where $H_1 = H_o + V_c + V_t + \lambda\vec{L}\cdot\vec{S}$.

Neglecting the last term Equation (I-8) becomes

$$H = H_1 + \sum_{i=1}^{n} (e/mc)\vec{A}_i\cdot\vec{p}_i + (e^2/2mc^2)(\vec{A}_i)^2 + (e/mc)\vec{H}\cdot\vec{s}_i$$

since the div $\vec{A} = 0$. Assuming the magnetic field $\vec{H}$ is described by the vector potential $\frac{1}{2}\vec{H} \times \vec{r}$ and that $\mu_o = \left(\frac{eh}{4\pi mc}\right)$, H becomes

$$H = H_1 + \sum_{i=1}^{n} (e/2mc)\vec{H} \times \vec{r}_i\cdot\vec{p}_i + (e^2/8mc^2)|\vec{H} \times \vec{r}_i|^2$$

$$+ (e/mc)\vec{H}\cdot\vec{s}_i$$

which upon collecting terms is now

$$H = H_1 + \mu_o(\vec{L} + g_s\vec{S})\cdot\vec{\mathcal{H}}$$

if the diamagnetic term $\sum_{i=1}^{n} (e^2/8mc^2)|\vec{\mathcal{H}} \times \vec{r}_i|^2$ is neglected.

The magnetic moment of an ion in the magnetic field is given by

$$\mu = -\frac{\partial E}{\partial \mathcal{H}} . \qquad \text{(I-9)}$$

The magnetic moment per gram ion is then obtained by averaging over all states, weighted with the Boltzman factor, thus[4]

$$M = \frac{N \sum_i \mu_i \exp\left(\frac{-E_i}{kT}\right)}{\sum_i \exp\left(\frac{-E_i}{kT}\right)} \qquad \text{(I-10)}$$

and, therefore, the magnetic susceptibility is given by

$$\chi = \frac{M}{\mathcal{H}} = \frac{N \sum_i \mu_i \exp\left(\frac{-E_i}{kT}\right)}{\mathcal{H} \sum_i \exp\left(\frac{-E_i}{kT}\right)} \qquad \text{(I-11)}$$

If it is assumed that E can be expanded as a power series in $\mathcal{H}$ such that

$$E = W^o + \mathcal{H} W^{(1)} + \mathcal{H}^2 W^{(2)} + \ldots \qquad \text{(I-12)}$$

then the paramagnetic susceptibility is given quantum mechanically by[3]

$$\chi = \frac{N \sum \omega_n \left\{ \left[W^{(1)}(n;n) \right]^2 / kT - 2W^{(2)}(n;n) \right\} \exp(W^o(n;n)/kT)}{\sum \omega_n \exp(-W^o(n;n)/kT)} \qquad \text{(I-13)}$$

where ω_n is the degeneracy of the state n.

The wave functions of the free ion are taken as the Clebsch-Gordan combinations of the one-electron orbitals and the wave functions for the cubic field, trigonal field, and $\vec{L}\cdot\vec{S}$ representations are obtained by appropriate methods that depend on the particular crystal and impurity.

Group theory[5,6] is very useful in determining how the different levels will split. In Appendix I the character table for the O and T_d groups is given along with the reducible representations for L = 0 to L = 4. The characters for the reducible representations were obtained by the use of the formula[6]

$$\chi_c(L) = \frac{\sin(L + \frac{1}{2})\omega_c}{\sin \frac{1}{2}\omega_c}$$

where ω_c is the rotation associated with the particular group operation (C_n) and

$$\omega_c = \left(\frac{2\pi}{n} \right) .$$

CHAPTER II

THE FARADAY BALANCE

General Information

A schematic diagram of the Faraday balance[7,8] designed and constructed for these studies of magnetic susceptibilities is shown in Figure 1. The upper portion (A, B, and C) is made of glass with two O-ring seals and one ground glass seal placed at several positions for easy assembly. The lower segment (D) is constructed of stainless steel tubing with a thick copper tube (E) at the very bottom to which two copper-Constanan thermocouples are attached. The entire system is usually evacuated and helium exchange gas admitted at a pressure of 2-4 cm of Hg. A small heater coil (G) is placed around the copper tube and this in turn is surrounded by a stainless steel jacket. A calibrated quartz spring (K) is attached to a hook (L) at the top end and the sample is attached to the lower end by means of a sample holder (J) made of a thin quartz fiber. A measuring microscope (M) is used to determine the extension of the spring.

The non-homogeneous magnetic field is supplied by a 2700 gauss General Electric magnet assembly (F). The magnet is moved past the sample in the vertical direction by the use

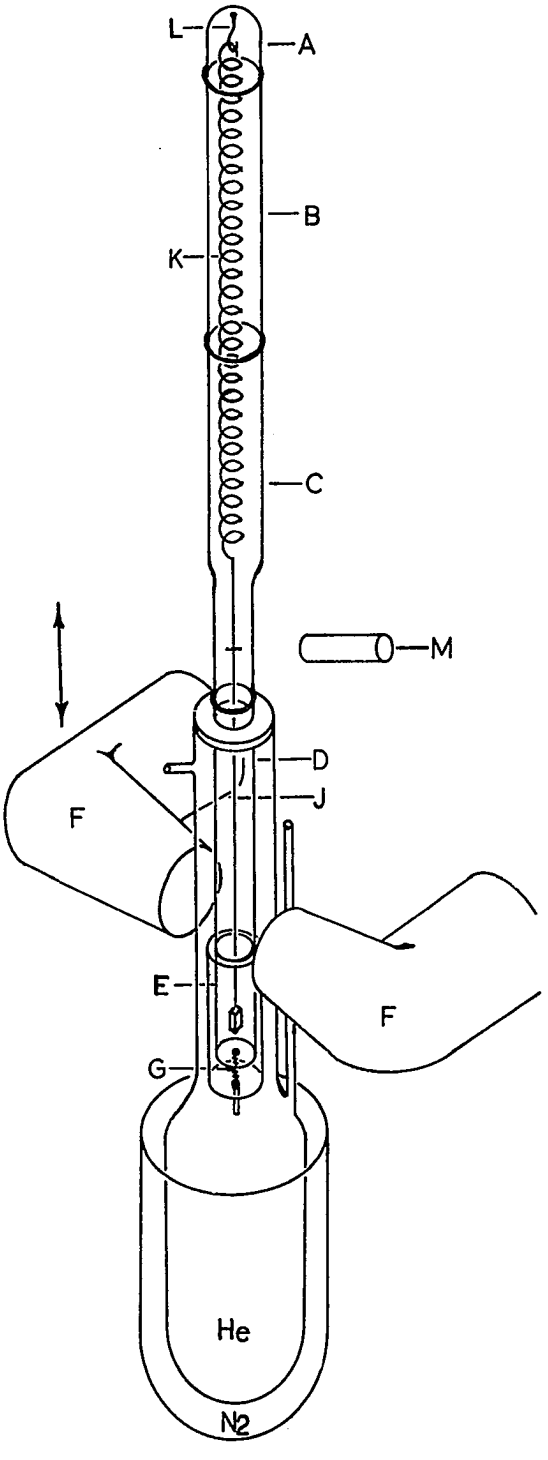

Figure 1. Diagram of the Faraday Balance

of a motor driven lift to which the base of the magnet has been bolted. A reversing switch allows the magnet to move up and down.

A specially designed helium Dewar was constructed for low temperature work. The helium, liquid or cold helium gas, is admitted through a side tube from a 15 or 25 liter storage Dewar by means of a helium transfer tube. Liquid nitrogen is used from 77-300°K. In order to obtain temperatures in the range 300-1000°K, the bottom part of the balance is removed and a heater is attached at one of the joints. Two different heaters have been built. One, constructed of copper tubing and wound with resistance wire, covers the range 300-500°K and the other, built by Segraves, extends the range to 1000°K and uses a platinum vs platinum +10% rhodium thermocouple.

The temperature is measured by the use of the thermocouples in conjunction with a calibrated Leeds and Northrup K-3 Potentiometer which utilizes a L & N D-C Null Detector and a Weston standard cell. The thermocouple voltage gives the temperature of the copper tube (E in Figure 1) which is assumed to be at the same temperature as the crystal. That the crystal and the copper tube are in thermal equilibrium with each other has been demonstrated by Stout and Griffel in a similar apparatus.[9] As a further check of the accuracy of the temperature measurements, the magnetic susceptibilities of Cr^{3+}:MgO over the range of 6°-293°K and of Cr_2O_3:Al_2O_3 from 293°-500°K have been measured. The furnace built by

Segraves has been calibrated by the use of Gd_2O_3. A plot of χ versus T^{-1} gave a straight line in each case.

In calibrating the magnetic field it was not necessary to obtain H, but instead $H(dH/dz)$. A piece of pure platinum (86.5 mg), 1 mm diameter and 5 mm long, was placed horizontally on the balance in place of the sample. The deflection (d) of the spring was determined as the magnet swept past at millimeter intervals. Using the equation

$$kd = m\chi H(dH/dz) \qquad \text{(II-1)}$$

where k is the force constant of the spring, m the mass of the sample, and a value of 0.969×10^{-6} for the mass susceptibility of the platinum,[10] $H(dH/dz)$ could be determined for a sample of any length. To check the consistency of these values the piece of platinum was placed in the balance in a vertical position and the susceptibility measured. This was also repeated with another piece of platinum. The results of this measurement differed from the accepted value only in the fourth place which is within the uncertainty of the readings of the spring deflection. Other known samples such as copper sulfate and glycerin were tried and the susceptibilities were determined to be within one percent of the accepted values. For the standard spring the mass susceptibility of a sample was given by

$$\chi_s = (0.56)(d_s/m_s) \times 10^{-9}$$

for a one mm high sample with d_s in scale divisions and m_s

in grams.

In measuring the susceptibility of a single crystal the sample was placed in the holder and then the apparatus assembled. One of the magnetic axes of the crystal was lined up parallel to the magnetic field. The magnet was then moved vertically until a maximum deflection was observed. The fixed cross hair in the microscope was aligned with a fixed mark on the sample holder. The magnet was then moved until a maximum deflection was observed in the opposite direction. The deflection was read from the scale of the microscope. From the known values of k, d, m, and $\mathcal{H}(d\mathcal{H}/dz)$ along with Equation (1), the susceptibility at this temperature could be determined. By varying the amount of heater current, the flow of liquid, or the flow of the cooled gas, a new temperature was obtained and the process repeated to measure the susceptibility at that temperature.

Operation

Calibration Of Springs And Measurement Of Deflection

In the calibration of one of the quartz springs, which were obtained from The Worden Company, it is picked up by the hook (L) located inside the top section (A). Section (A) is then placed on section (B) so that the spring is suspended inside (B). A piece of pure (99.999%) platinum is mounted on the bottom end of a 45 cm thin quartz fiber and is aligned parallel to an axial reference fiber located near the top of the holder. The holder is attached to the lower hook of the

spring, and additional weights are added at this point until the sample is 95 cm below the bottom of section (B). The sample is then centered in the magnetic field. Section (C) is clamped in position and, finally, the lower part (D and E) is placed in position. Minor alignment of all the sections is made to insure that the sample is not in contact with the copper tube (E). The region inside the sections is evacuated by a vacuum pump, and helium gas is then admitted until the pressure rises to 4 cm of Hg. Section (A) is rotated until the reference fiber is parallel to the magnetic field. The microscope is focused on the reference fiber. The reversing switch, which controls the direction in which the magnet moves, is placed in the up position and the magnet brought to a position so that the deflection is close to a minimum value. The fixed cross hair is moved to this position. By use of the reversing switch the minimum value of the deflection is located and the fixed cross hair placed at that position. The reversing switch is then placed in the down position and the magnet moved until a maximum deflection is obtained. The movable cross hair is placed in this position. In this manner the total deflection (d_p) from maximum to minimum can be measured. This should be repeated at least five times. The same procedure is followed with the reference fiber at 45, 90, and 135 degrees with respect to the magnetic field. None of the readings should differ from the average over about 10 scale divisions which is only twice the width of the cross

hair. By the use of Equation (1) the mass susceptibility of a sample can be found using this spring as

$$\chi_s = (83.8/d_p)(d_s/m_s) \times 10^{-6}$$

where m_s is measured in mgs.

Temperature Measurement

The temperature is measured by the use of the copper-Constanan and the platinum vs platinum +10% rhodium thermocouples in conjunction with a calibrated Leeds and Northrup K-3 potentiometer. Figure (2) shows a block diagram of the temperature measuring apparatus. The K-3 is operated in accordance with the operating instructions contained in the L. & N. Operation Manual 177016.

The ice bath, in which one junction of each thermocouple is placed, is a double walled Dewar container filled with crushed ice. That the ice bath is at 0°C is established by measuring the emf of a thermocouple which has one junction in the ice bath and the other in a Trans-Sonics Equiphase Cell (triple point cell). The difference in temperature between the triple point and the freezing point of water is 0.01°C.

Following the recommendation of Scott[11] a chart, on which emf versus temperature is plotted, was drawn using data collected by Bunch, Powell, and Carruccini[12] for the Leeds and Northrup copper-Constantan thermocouple wire. A plot of this data was considered to be a base line. For temperatures

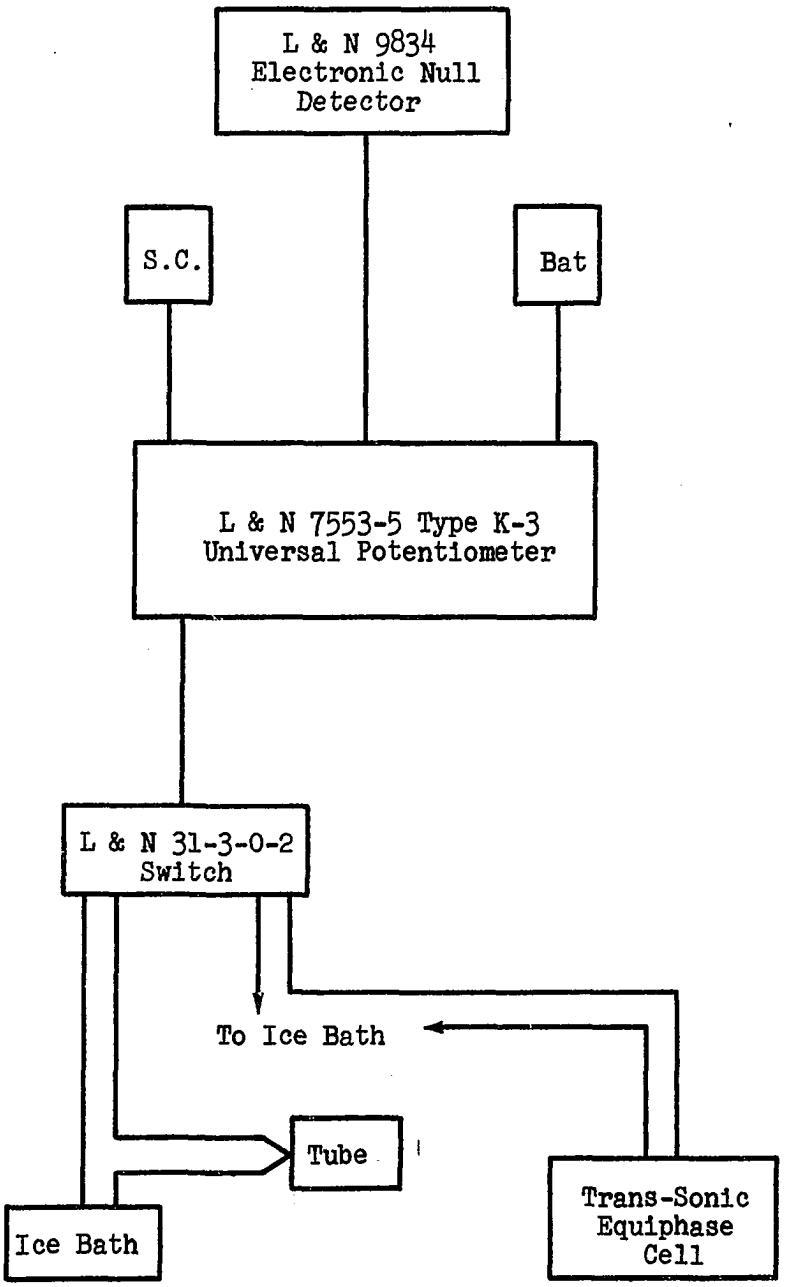

Figure 2. Temperature Measuring Apparatus

above 77°K the base line is more than adequate for susceptibility purposes. This was, of course, checked by measuring the magnetic susceptibility of substances such as Cr^{3+}:MgO and then plotting deflection versus (1/T) to ascertain if the equation

$$\chi = (C'/T) + \alpha'$$

was satisfied. The error in the temperature measurement was less than the error in the deflection measurement corresponding to twice the width of the cross-hair of the measuring microscope.

For temperatures less than 77°K an additional thermocouple has been constructed and the emf is measured for the liquid nitrogen and the liquid helium boiling point. A deviation graph is constructed assuming a uniform change between the two temperatures. The readings of the thermocouples attached to the copper tube are assumed to follow this same curve. Initially, this procedure was checked by using Cr^{3+}:MgO as a calibrating substance down to 6°K. Later, other substances such as Yb^{3+}:YGG were also measured and the procedure was found to give correct results within an error of ± 0.2°K.

In the case of the platinum vs platinum +10% rhodium thermocouple the thermocouple is guaranteed to 1% but again this was checked by using Gd_2O_3 as the calibrating substance and assuming that a Curie-Weiss law is followed with θ = 18.4°. It was found that the accuracy of the calibration was

limited by the deflection measurement and that the accuracy of the temperature measurement was better than 1%.

Mounting Of Sample

A holder is constructed for each sample from thin fibers of quartz. Each holder should be 45 cm in length from the top hook to the middle of the sample and for the single crystals an axial reference fiber is placed about 3 cm from the top. The bottom part of the holder is constructed to hold the crystals so that rotation of the holder about the vertical direction will bring, first, one magnetic axis and then the other into a position which is parallel to the magnetic field.

The holder is then attached to the spring and additional weights added until the sample is 95 cm below the bottom of Section (B). The sample is centered in the magnetic field and Section (C) is then clamped in position. For a low temperature run the lower segment (D and E) is positioned and the Dewar system elevated into position. The balance is evacuated and helium exchange gas is admitted through a stopcock until the pressure reaches 2-4 cm of Hg at which time the system is closed off by another stopcock at Section (B). For a high temperature run one of the furnaces is raised into position and the vacuum pump is run continuously.

Temperature Control

For the 77-300°K temperature range a copper tube was

wound in the shape of a coil with one end connected by means of rubber tubing to a tank of nitrogen gas. A piece of stainless steel tubing was connected to the other end and bent so as to slip inside the side tube of the Dewar system. The copper tubing is placed inside another nitrogen Dewar and this is, in turn, filled with liquid nitrogen. The warm nitrogen gas from the tank is forced through the copper tubing where it is cooled and then through the special Dewar, cooling the copper tube (E) in the process, and then out through the exhaust tube. The temperature of the copper tube is controlled by the rate of flow of the nitrogen gas through the cooling apparatus. The temperature can be maintained to within $\pm$ 0.2°K almost indefinitely. Nitrogen temperature is attained by filling the Dewar with liquid nitrogen. The temperature between 77 and about 90°K cannot be reached by this method and it is necessary that liquid nitrogen be added by small amounts to the Dewar system raising the temperature by a few degrees at a time or by filling the bottom part of the Dewar with liquid nitrogen and then forcing nitrogen gas through the liquid. It is not possible to maintain the temperature in this range for over about a minute or so. The estimated uncertainty in this range is $\pm$ 1°K.

Below 77°K it is necessary to make use of liquid helium. The helium is transferred from a 15 or 25 liter storage Dewar to the balance Dewar by means of a Hofman double walled liquid helium transfer tube. The liquid helium is

forced through the transfer tube by means of gaseous helium at a pressure slightly in excess of atmospheric. This pressure is variable but it can also be kept constant by a pressure regulator. By careful adjustment of a manual control and the pressure regulator the temperature of the tube (E) can be kept constant for considerable lengths of time. Rubber tubing connects the regulator to the liquid helium storage Dewar and also to the tank of gaseous helium.

In the temperature range 300-1000°K the temperature of the furnace is controlled by means of a 15 ampere variable auto transformer. By allowing different values of current to flow through the glow bars of the furnace different temperatures can be attained. The temperature can be maintained within ± 1°K almost indefinitely.

CHAPTER III

THE ANISOTROPY TORSION BALANCE

General Information

To measure the difference in susceptibility of a sample at low temperatures, a torsion balance[7] (shown in Figure 3) was constructed. The homogeneous magnetic field is supplied by a rotating Varian 6 in. magnet (M) and its regulated power supply. The gap is set at 2.85 in. to accommodate a liquid helium assembly used in ESR measurements. The helium Dewar (B) and the nitrogen Dewar (A) are used as supplied, but in place of the wave guide assembly, a different unit is used. It has the same dimensions as the wave guide assembly but the rectangular waveguide itself is replaced by a round tube. The upper portion (C) of the tube is made of stainless steel while the bottom is a thick copper tube (D) to which a copper-constanan thermocouple and a gold-cobalt versus silver-gold thermocouple are cemented directly opposite the sample.

A magnetically anisotropic sample in a homogeneous field experiences a torque which is proportional to $\chi_{\perp} - \chi_{\parallel}$. Instead of finding this torque from the angle of torsional rotation, a counter torque is applied to bring the crystal back to the original orientation. The counter torque is

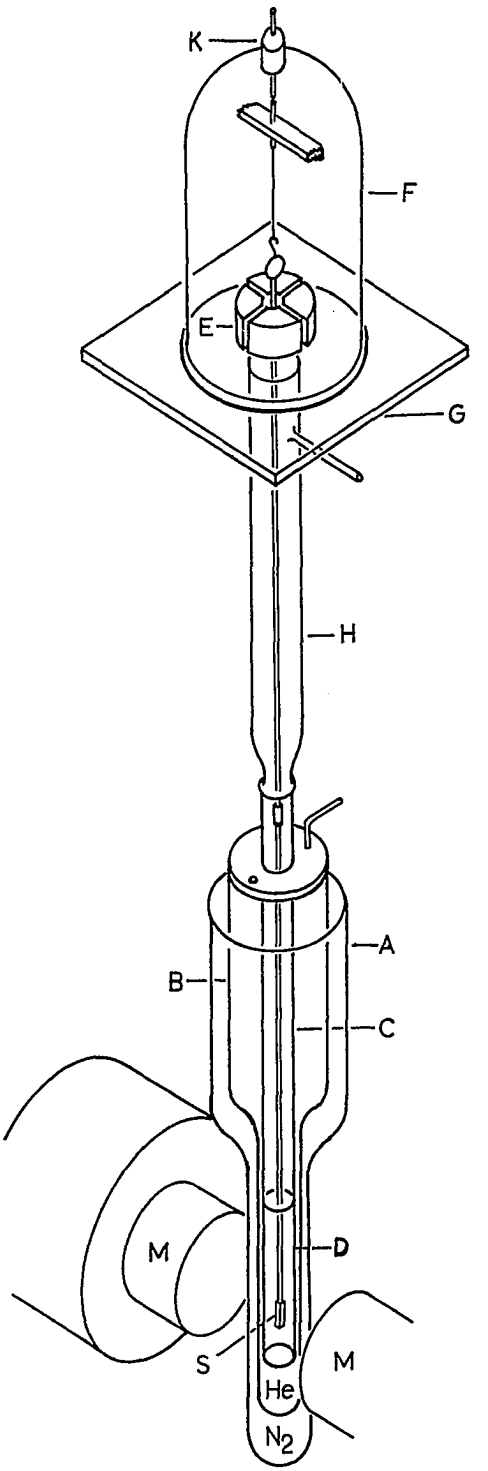

Figure 3. Diagram of the Anisotropy Torsion Balance

supplied by a quadrant electrometer (E). The zero of the electrometer can be changed by means of a ball and socket joint (K) at the top of the bell jar (F) which is placed over the electrometer. A telescope and scale are used to detect the deflection of the vane. The bell jar rests on a rubber pad which, in turn, is supported by an aluminum plate (G). Electrical leads to the electrometer pass through the aluminum plate from two different batteries. The sensitivity of the balance can be varied by changing the potential of the vane and batteries of 1.4, 6, 22, 45, 90, and 300 volts were available for this purpose. Either a fixed or variable potential difference could be applied to the quadrants so that it was possible to either keep the voltage applied to the quadrants constant and change the magnetic field to produce zero deflection or to fix the magnetic field and vary the voltage applied to the quadrants.

The aluminum plate is connected to the Dewar assembly by means of a glass tube (H) which has O-ring seals on both ends. The glass tube also has an opening for evacuation purposes and helium gas can be admitted at any desired pressure. The sample (S) is supported by a very thin quartz holder. The holder is connected to the bottom of a very long quartz rod (2-mm diameter). The upper end of the quartz rod is, in turn, cemented to the vane of the electrometer. The quartz rod consists of two parts for ease of handling.

Bates gives the equation for the torque acting on a

sample in a homogeneous magnet field as[8]

$$L = m(\Delta\chi)\mathcal{H}^2 \sin 2\theta, \qquad \text{(III-1)}$$

where θ is the angle between the principal crystalline axis and the magnet field. If the voltages applied to the electrometer are kept constant, then the counter torque should be the same for each measurement. Since the sample is always rotated to the same position, θ is the same in each case. Therefore, $\mathcal{H}^2\Delta\chi$ should be constant. A plot of current versus $\mathcal{H}$ for the magnet gives a straight line, within the accuracy of the gaussmeter, for the gap and magnetic fields used. It follows that

$$(\Delta\chi_{T_1}/\Delta\chi_{T_2}) = (I^2_{T_2}/I^2_{T_1})$$

Using the value of $\Delta\chi$ as measured by the Faraday balance at a particular temperature, $\Delta\chi$ can be determined for the other temperatures.

When the magnetic field is kept constant, the voltage applied to the quadrants is varied until a zero deflection is observed. The voltage is measured by a voltmeter. Since the field and the angle θ in Equation (III-1) is kept constant the counter torque is directly proportional to $\Delta\chi$. For an electrometer

$$L = c\, V_q\, (V_v - \tfrac{1}{2}V_q)$$

where V_q is the voltage applied to the quadrants, and V_v is

the voltage applied to the vane and c is a constant. It follows that

$$(\Delta\chi)_{T_1}/(\Delta\chi)_{T_2} = V_q(V_v - \tfrac{1}{2}V_q)_{T_1}/V_q(V_v - \tfrac{1}{2}V_q)_{T_2} .$$

Operation

Assembly of Apparatus

The liquid helium assembly is mounted on the Varian magnet (M) in accordance with the operating instructions of Varian. The sample is placed in the holder so that the crystal can be rotated about the vertical with, first, the magnetic z-axis being parallel to the magnet field and then after a rotation of 90 degrees the x-axis would be parallel to $\vec{H}$. The holder, which is fastened on to part of the 2 mm quartz support rod, and the support rod are then placed inside sections (C) and (D). The upper portion of the support rod is fastened to the vane of the electrometer which is resting on the rubber pad and the plate (G). The glass tube (H) is clamped to plate (G). The magnet is moved to a position so that the lower section of the support rod is almost underneath the upper position; after which, the two were fastened together. The magnet assembly is raised vertically until section (C) makes contact with the tube (H). The two are then clamped together. A thin copper ribbon is attached to the vane and both are raised by a screw mechanism until the vane is free to rotate inside the quadrants. Leveling

screws located on the electrometer, on the support for the aluminum plate (G), and on the magnet assembly are utilized to center the sample inside the copper tube (D). The bell jar (F) is placed over the electrometer. A ball and socket joint (K) at the top of the bell jar was devised so that on rotating the joint the zero of the electrometer could be changed. This is done by a glass rod connecting the joint and the zeroing mechanism of the electrometer.

The system is evacuated by a pump and He gas admitted until a pressure of about 4 cm of Hg is reached at which time the system is closed off by the stopcock located on the glass tube (H). The socket joint (K) is rotated until the electrometer is zeroed.

Temperature Measurement And Control

The temperature of the copper tube (D) is determined by a copper-Constanan thermocouple and a gold-cobalt versus silver-gold thermocouple in conjunction with the K-3 Potentiometer and the Null Detector. The same auxiliary equipment is used as for the Faraday balance. A calibration chart was set up and the thermocouples calibrated at the N_2 and He boiling points as before.

The temperature is controlled ($\pm$ 0.2°K) by adjusting the flow of cold helium gas from a storage Dewar. Measurements are also taken at the He point and, upon part of the liquid He boiling away, as the copper tube warms up. The warm up of the copper tube is quite slow and the temperature

is considered to be accurate within ± 0.2°K.

Fixed Voltage Measurements

Depending on the sensitivity desired a battery is chosen and then connected to the electrometer terminals so as to give the vane a certain potential. A difference of potential is applied to the quadrants by means of another battery. The magnetic field is then adjusted until a zero deflection is observed by means of the telescope system. The current through the magnet is determined by the meter on the regulated power supply. Care should be taken that the electrometer deflection is never allowed to exceed about 20 degrees and that it is properly zeroed.

Fixed Field Measurements

A battery is connected to the vane terminals of the electrometer so as to give the electrometer the desired sensitivity. The magnetic field is set at a particular value and is not changed during a set of measurements. The difference of potential applied to the quadrants is then varied until the electrometer is brought back to the zero position. When the temperature is changed it is necessary to keep the electrometer approximately zeroed in order to keep the electrometer properly zeroed.

CHAPTER IV

Ni^{2+} IN THE TETRAHEDRAL SITES OF CdS AND ZnO

The electron configuration of the Ni^{2+} ions is $(3d)^8$ and this configuration in octahedral fields has been studied extensively.[13,14,15] It was found that the orbital levels of the nickel ion (^3F) are split so that the orbital singlet is lowest in a cubic field.

The atoms in the two-molecule hexagonal unit of the wurtzite arrangement are in the positions[16]

$$\begin{aligned} R:&\quad 0\ 0\ 0\ ;\quad 1/3,\ 2/3,\ 1/2 \\ X:&\quad 0\ 0\ u\ ;\quad 1/3,\ 2/3,\ u + \tfrac{1}{2}\ . \end{aligned} \qquad \text{(IV-1)}$$

The axial ratio of the CdS crystal with this type structure is $c/a = 1.62$ and the parameter u is 0.375 while for ZnO the axial ratio[17] $c/a = 1.60$ and $u = 0.378$. Under these conditions each atom has about it a tetrahedron of atoms of the opposite sort and the point symmetry is C_{3v}. The cubic field potential for an ion in tetrahedral symmetry is about (-4/9) times the corresponding term for octahedral symmetry[17] with the same R-X distances. Since the sign of the cubic field parameter for a tetrahedron is opposite that of an octahedron it is expected that the level schemes would be

inverted for T_d symmetry. This is indeed the case in studies of the optical spectra[18,19] where it was found that the $^3T_1$ level of ^3F was lowest.

In the case of $V^{3+}:Al_2O_3$ which has a $(3d)^2$ configuration in an octahedral field it was found[20,21] that the $^3T_1$ level was lowest and, in fact, through the cubic field splittings the level schemes for $(3d)^2$ in octahedral and $(3d)^8$ in tetrahedral fields should be the same.

The spin orbit coupling constant for a free Ni^{2+} ion is quite large ($-340\ cm^{-1}$) and it is only natural to take the $\vec{L}\cdot\vec{S}$ splittings as being larger than the trigonal. This turns out to be a good approximation in the case of the CdS crystal[18] where the trigonal splittings are quite small but in the case of the ZnO crystal the trigonal matrix elements are of the same order of magnitude as the spin-orbit elements. The energy level diagram of the Ni^{2+} ions in a tetrahedral site is shown in Figure (4) assuming cubic $>\vec{L}\cdot\vec{S}>$ trigonal splittings.

Experiment

The crystals of Ni^{2+}:CdS were furnished by Dr. T. L. Estle of Texas Instruments, Inc., and the Ni^{2+}:ZnO by Dr. H. A. Weakliem of the RCA Laboratories. The measurements of the magnetic susceptibility were made by means of the Faraday balance. In Tables 1 and 2 are shown the magnetic susceptibilities of Ni^{2+}:CdS and Ni^{2+}:ZnO crystals along and perpendicular to the trigonal axis over the temperature range

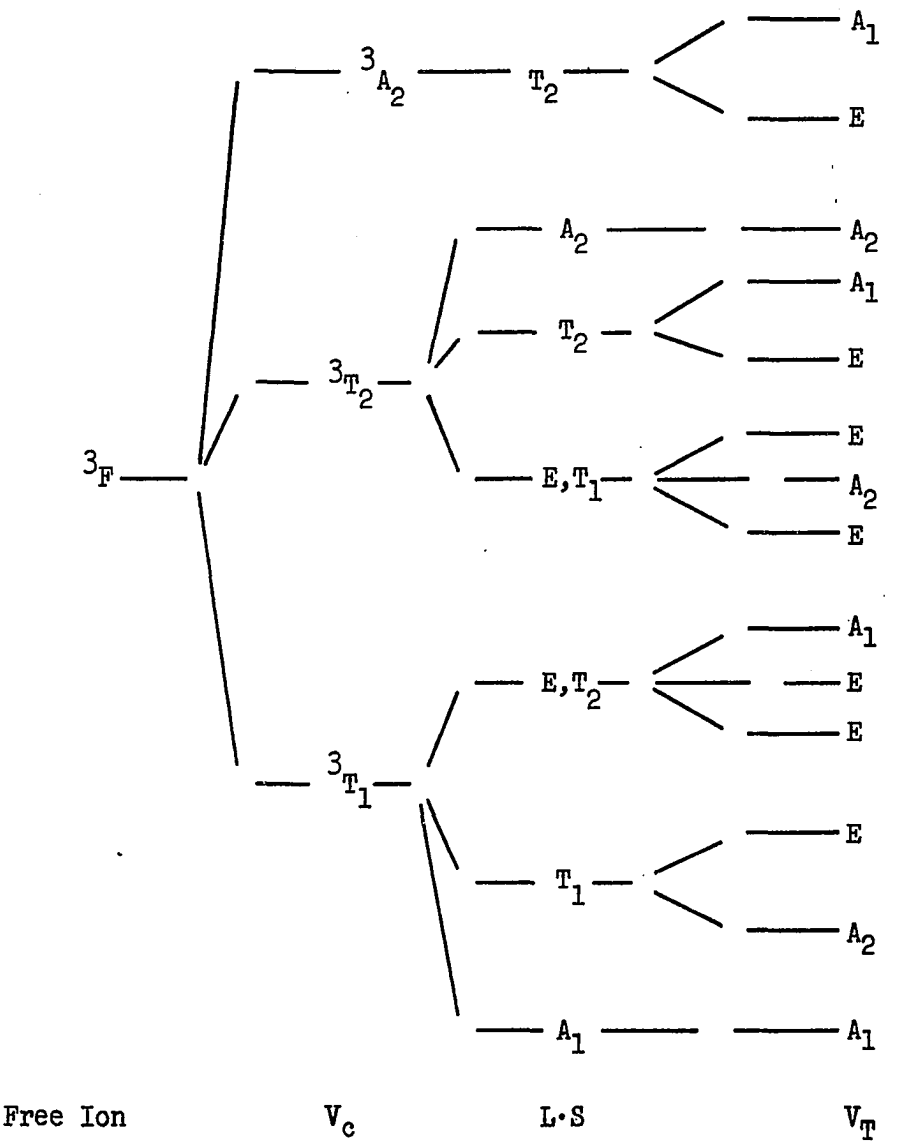

Figure 4. Energy Level Diagram of Ni^{2+} in a Tetrahedral Field

TABLE 1

MAGNETIC SUSCEPTIBILITIES (PER GRAM SAMPLE) OF Ni^{2+} - DOPED CdS CRYSTAL. CONCENTRATION: 0.84%

T (°K)	$\chi_{\parallel} \times 10^7$ (cgs-emu)	T (°K)	$\chi_{\perp} \times 10^7$ (cgs-emu)
77.3	8.30	77.3	7.90
94	7.75	86	7.60
108	7.12	101	7.18
128	6.32	121	6.35
154	5.40	134	5.85
174	4.68	164	4.80
202	3.86	184	4.16
217	3.51	203	3.72
232	3.11	219	3.48
255	2.63	249	2.77
296	1.98	294	1.98
391	0.90	389	0.80
489	0.21	448	0.37

TABLE 2

MAGNETIC SUSCEPTIBILITIES (PER GRAM SAMPLE) OF Ni^{2+} - DOPED ZnO CRYSTAL. CONCENTRATION: 0.076%

T (°K)	$\chi_{\parallel} \times 10^7$ (cgs-emu)	T (°K)	$\chi_{\perp} \times 10^7$ (cgs-emu)
28.0	0.00	28.0	-1.85
77.3	-0.27	77.3	-1.85
97	-0.53	107	-1.85
108	-0.75	114	-1.95
130	-1.08	118	-2.00
140	-1.30	151	-2.10
203	-1.90	167	-2.13
253	-2.16	201	-2.35
273	-2.22	250	-2.46
300	-2.33	300	-2.57
335	-2.42	330	-2.73
403	-2.66	401	-2.86
501	-2.90	501	-2.90

of 77-500°K. The concentration of the nickel ions in ZnO and CdS are 0.076% and 0.84%, respectively, as determined from the analysis of the magnetic data. The accuracy of the measured susceptibility in ZnO (± 4%) is somewhat lower than in CdS (± 2%) because of the smaller concentration of Ni^{2+} in the former.

Theory And Analysis Of Data

The Hamiltonian for a Ni^{2+} ion is taken as

$$H = H_o + V_c + \lambda \vec{L}\cdot\vec{S} + V_t + \mu_o(\vec{L} + g_s\vec{S})\cdot\vec{H} \quad . \qquad \text{(IV-2)}$$

The general procedure will be to take each term of the Hamiltonian in order and diagonalize the appropriate energy matrix. In the case of H_o the eigenfunctions can be obtained by the use of step-down operators[22] or by the use of Clebsch-Gordan coefficients[20,23] to combine the one electron wave functions in the (lm) representation to form the (LM) representation. The energy matrix of H_o in the (LM) representation, for the $(3d)^8$ configuration only, is diagonal and is split into the following levels for the free ion[24]

$$\begin{aligned} {}^3F &= F_o - 8F_2 - 9F_4 \\ {}^3P &= F_o + 7F_2 - 84F_4 \\ {}^1G &= F_o + 4F_2 + F_4 \\ {}^1D &= F_o - 3F_2 + 36F_4 \\ {}^1S &= F_o + 14F_2 + 126F_4 \end{aligned} \qquad \text{(IV-3)}$$

where the F_k's are the Slater-Condon-Shortley integrals.[25]

These levels are easily obtainable using Table 1^6 of Reference (25). The eigenfunctions of H_o are listed in Appendix II.

The free ion levels are split by a cubic field in the following manner (see Appendix I)

$$\begin{aligned} {}^3F &\rightarrow {}^3T_1 + {}^3T_2 + {}^3A_2 & {}^1D &\rightarrow {}^1E + {}^1T_2 \\ {}^3P &\rightarrow {}^3T_1 & {}^1S &\rightarrow {}^1A_1 \quad . \\ {}^1G &\rightarrow {}^1A_1 + {}^1T_1 + {}^1E + {}^1T_2 \end{aligned} \tag{IV-4}$$

The cubic crystal potential term is taken as

$$V_c = \sum_{i=1,2} r_i^4 \, A_4^o \left\{ Y_4^o(\theta_i\varphi_i) + (10/7)^{\frac{1}{2}} \left[Y_4^3(\theta_i\varphi_i) - Y_4^{-3}(\theta_i\varphi_i) \right] \right\} \tag{IV-5}$$

and the cubic crystal field parameter is defined as

$$\beta = A_4^o \langle r^4 \rangle / 14\sqrt{\pi} \tag{IV-6}$$

The matrix elements of V_c in the (LM) representation are listed in Appendix III along with the eigenvalues. Upon diagonalizing these matrices the eigenvectors for the cubic representation can be obtained.[20] These are listed in Appendix IV.

Since V_c has matrix elements connecting ${}^3T_1({}^3F)$ and ${}^3T_1({}^3P)$ a transformation

$$\begin{matrix} {}^3F \\ {}^3P \end{matrix} \begin{pmatrix} a_1 & a_2 \\ -a_2 & a_1 \end{pmatrix} \tag{IV-7}$$

must be applied to these two states in order to diagonalize $H_o + V_c$. This results in a mixing of the F and P states.

Spin orbit interaction gives further splittings into components that are shown in Figure 4. For the triplet states

$$\begin{aligned} {}^3T_1 &\rightarrow A_1 + T_1 + E + T_2 \\ {}^3T_2 &\rightarrow A_2 + T_1 + E + T_2 \\ {}^3A_2 &\rightarrow T_2 \end{aligned} \qquad \text{(IV-8)}$$

The nine functions associated with the ${}^3T_1$ (and ${}^3T_2$) levels must be re-grouped in such a way as to exhibit the decomposition shown in (IV-8). This can be done by diagonalizing the (9 X 9) matrix of $\lambda\vec{L}\cdot\vec{S}$ and then consider the new wave functions associated with each energy level. It turns out that the wave function of the singlet state (3λ) transforms like A_1 and the three associated with the triplet state ($\frac{3}{2}\lambda$) transform like T_1. The five functions associated with the quintiplet state ($-\frac{3}{2}\lambda$) do not show explicitly the transformation properties of E and T_2. It is found that if these five functions are treated formally the same as the five basis functions in the (LM) representation with L = 2 and M = 2, 1, 0, -1, -2, and then mixed in accordance with the same sort of transformation as given in Appendix IV to form the cubic functions, then two of the resulting wave functions do transform like E and the other three like T_2. The matrix elements of $\vec{L}\cdot\vec{S}$ in the cubic representation are obtained by

the use of the formulas[26]

$$(M_L M_S|\vec{L}\cdot\vec{S}|M_L M_S) = M_L M_S$$

$$(M_L M_S|\vec{L}\cdot\vec{S}|M_L-1\ M_S+1) = \tfrac{1}{2}\{[L(L+1) - M_L(M_L - 1)][S(S+1) - M_S(M_S+1)]\}^{\frac{1}{2}}$$

$$(M_L M_S|\vec{L}\cdot\vec{S}|M_L+1\ M_S-1) = \tfrac{1}{2}\{[L(L+1) - M_L(M_L + 1)][S(S+1) - M_S(M_S-1)]\}^{\frac{1}{2}}$$

for the (LM) representation. The matrix elements of $\lambda\vec{L}\cdot\vec{S}$ in the cubic representation are listed in Appendix V.[21] Table 3 contains the wave functions for the L·S representation.

The Hamiltonian

$$H' = H_o + V_c + \lambda\vec{L}\cdot\vec{S} \qquad \text{(IV-9)}$$

is not completely diagonal using the $\vec{L}\cdot\vec{S}$ representation since there are matrix elements of $\lambda\vec{L}\cdot\vec{S}$ connecting the different levels. All the matrix elements of H' in the $\vec{L}\cdot\vec{S}$ representation are listed in Table 4 which also contains the trigonal elements.

When the trigonal field is introduced the T_1 level splits into A_2 and E levels while T_2 splits into an A_1 and E level which are the correlated levels in C_{3v} symmetry. The trigonal potential term is taken as

$$V_t = \sum_{i=1,2}\left\{r_i^2\, B_2^o\, Y_2^o\,(\theta_i\varphi_i) + r_i^4\, B_4^o\, Y_4^o\,(\theta_i\varphi_i)\right\} \qquad \text{(IV-10)}$$

TABLE 3

SPIN ORBIT WAVE FUNCTIONS OF ^3F AND ^3P*

$^3F^3T_1$

$$\Psi(^3F^3T_1A_1A_1) = [\Psi(^3F^3T_1^-S_{-1}) - \Psi(^3F^3T_1^oS_o) + \Psi(^3F^3T_1^+S_1)]/\sqrt{3}$$

$$\Psi(^3F^3T_1T_1A_2) = [\Psi(^3F^3T_1^-S_{-1}) - \Psi(^3F^3T_1^+S_1)]/\sqrt{2}$$

$$\Psi(^3F^3T_1T_1E_1) = [\Psi(^3F^3T_1^-S_o) - \Psi(^3F^3T_1^oS_1)]/\sqrt{2}$$

$$\Psi(^3F^3T_1T_1E_2) = [\Psi(^3FT_1^oS_{-1}) - \Psi(^3FT_1^+S_o)]/\sqrt{2}$$

$$\Psi(^3F^3T_1EE_1) = [\Psi(^3F^3T_1^-S_o) + \Psi(^3F^3T_1^oS_1) - \Psi(^3F^3T_1^+S_{-1})]/\sqrt{3}$$

$$\Psi(^3F^3T_1EE_2) = [\Psi(^3F^3T_1^+S_o) + \Psi(^3F^3T_1^oS_{-1}) + \Psi(^3F^3T_1^-S_1)]/\sqrt{3}$$

$$\Psi(^3F^3T_1T_2A_1) = [\Psi(^3F^3T_1^-S_{-1}) + 2\Psi(^3F^3T_1^oS_o) + \Psi(^3F^3T_1^+S_1)]/\sqrt{6}$$

$$\Psi(^3F^3T_1T_2E_1) = [2\Psi(^3F^3T_1^-S_1) - \Psi(^3F^3T_1^+S_o) - \Psi(^3F^3T_1^oS_{-1})]/\sqrt{6}$$

$$\Psi(^3F^3T_1T_2E_2) = [-2\Psi(^3F^3T_1^+S_{-1}) - \Psi(^3F^3T_1^-S_o) - \Psi(^3F^3T_1^oS_1)]/\sqrt{6}$$

$^3F^3T_2$

$$\Psi(^3F^3T_2A_2A_2) = [-\Psi(^3F^3T_2^oS_o) + \Psi(^3F^3T_2^+S_1) + \Psi(^3F^3T_2^-S_-)]/\sqrt{3}$$

$$\Psi(^3F^3T_2T_2A_1) = [\Psi(^3F^3T_2^-S_{-1}) - \Psi(^3F^3T_2^+S_1)]/\sqrt{2}$$

$$\Psi(^3F^3T_2T_2E_1) = [\Psi(^3F^3T_2^-S_o) - \Psi(^3F^3T_2^oS_1)]/\sqrt{2}$$

$$\Psi(^3F^3T_2T_2E_2) = [\Psi(^3F^3T_2^oS_{-1}) - \Psi(^3F^3T_2^+S_o)]/\sqrt{2}$$

TABLE 3 (continued)

$$\Psi(^3F^3T_2EE_1) = [\Psi(^3F^3T_2^+S_{-1}) + \Psi(^3F^3T_2^oS_1) + \Psi(^3F^3T_2^-S_o)]/\sqrt{3}$$

$$\Psi(^3F^3T_2EE_2) = [\Psi(^3F^3T_2^-S_1) + \Psi(^3F^3T_2^oS_{-1}) + \Psi(^3F^3T_2^+S_o)]/\sqrt{3}$$

$$\Psi(^3F^3T_2T_1A_2) = [2\Psi(^3F^3T_2^oS_o) + \Psi(^3F^3T_2^+S_1) + \Psi(^3F^3T_2^-S_{-1})]/\sqrt{6}$$

$$\Psi(^3F^3T_2T_1E_1) = [2\Psi(^3F^3T_2^-S_1) - \Psi(^3F^3T_2^oS_{-1}) - \Psi(^3F^3T_2^+S_o)]/\sqrt{6}$$

$$\Psi(^3F^3T_2T_1E_2) = [-2\Psi(^3F^3T_2^+S_{-1}) - \Psi(^3F^3T_2^oS_1) - \Psi(^3F^3T_2^-S_o)]/\sqrt{6}$$

$^3F^3A_2$

$$\Psi(^3F^3A_2A_1) = \Psi(^3F^3A_2S_o)$$

$$\Psi(^3F^3A_2E_1) = \Psi(^3F^3A_2S_1)$$

$$\Psi(^3F^3A_2E_2) = \Psi(^3F^3A_2S_{-1})$$

$^3P^3T_1$

$$\Psi(^3P^3T_1A_1A_1) = [\Psi(^3P^3T_1^+S_{-1}) - \Psi(^3P^3T_1^oS_o) + \Psi(^3P^3T_1^-S_1)]/\sqrt{3}$$

$$\Psi(^3P^3T_1T_1A_2) = [\Psi(^3P^3T_1^+S_{-1}) - \Psi(^3P^3T_1^-S_1)]/\sqrt{2}$$

$$\Psi(^3P^3T_1T_1E_1) = [\Psi(^3P^3T_1^+S_o) - \Psi(^3P^3T_1^oS_1)]/\sqrt{2}$$

$$\Psi(^3P^3T_1T_1E_2) = [\Psi(^3P^3T_1^oS_{-1}) - \Psi(^3P^3T_1^-S_o)]/\sqrt{2}$$

$$\Psi(^3P^3T_1EE_1) = [-\Psi(^3P^3T_1^-S_{-1}) + \Psi(^3P^3T_1^+S_o) + \Psi(^3P^3T_1^oS_1)]/\sqrt{3}$$

$$\Psi(^3P^3T_1EE_2) = [\Psi(^3P^3T_1^+S_1) + \Psi(^3P^3T_1^oS_{-1}) + \Psi(^3P^3T_1^-S_o)]/\sqrt{3}$$

TABLE 3 (continued)

$$\Psi(^3P^3T_1T_2A_1) = [\Psi(^3P^3T_1^+S_{-1}) + 2\Psi(^3P^3T_1^oS_o) + \Psi(^3P^3T_1^-S_1)]/\sqrt{6}$$

$$\Psi(^3P^3T_1T_2E_1) = [2\Psi(^3P^3T_1^+S_1) - \Psi(^3P^3T_1^oS_{-1}) - \Psi(^3P^3T_1^-S_1)]/\sqrt{6}$$

$$\Psi(^3P^3T_1T_2E_2) = [-2\Psi(^3P^3T_1^-S_{-1}) - \Psi(^3P^3T_1^+S_o) - \Psi(^3P^3T_1^oS_1)]/\sqrt{6}$$

---

*The four subscripts describing the wave functions are associated with the decomposition of the levels when H_o, V_c, $\lambda\vec{L}\cdot\vec{S}$, and V_t are considered.

TABLE 4

ENERGY MATRIX OF H' FOR Ni^{2+} IN THE $\vec{L}\cdot\vec{S}$ REPRESENTATION*

E

$^3T_1T_1(^3F)$	$^3T_1E(^3F)$	$^3T_1T_2(^3F)$	$^3T_2T_2(^3F)$	$^3T_2E(^3F)$
$-9\beta + \frac{3}{2}\lambda - 2\gamma + \frac{1}{2}\tau$	$\sqrt{6}\ (-5\gamma - \frac{1}{2}\tau)$	$+\sqrt{3}\ (5\gamma - \frac{1}{2}\tau)$	$-2\sqrt{5}\ \gamma + \frac{\sqrt{5}\,\tau}{2}$	$-\frac{\sqrt{30}}{6}\ (4\gamma - \tau)$
	$-9\beta - \frac{3}{2}\lambda - 7\gamma$	$\sqrt{2}\ (-5\gamma - \frac{1}{2}\tau)$	$\frac{\sqrt{30}}{6}\ (-4\gamma + \tau)$	$\frac{3}{2}\sqrt{5}\ \lambda$
		$-9\beta - \frac{3}{2}\lambda - 12\gamma - \frac{\tau}{2}$	$\frac{\sqrt{15}}{2}\lambda + \frac{\sqrt{15}}{6}\ (4\gamma - \tau)$	$\frac{\sqrt{10}}{2}\ (4\gamma - \tau)$
			$3\beta - \frac{\lambda}{2} + 4\gamma + \frac{5\tau}{2}$	$\frac{\sqrt{6}}{6}\ (-10\gamma - 15\tau)$
				$3\beta + \frac{\lambda}{2} + \frac{7\gamma}{3}$

TABLE IV (continued)

$^3T_2T_1(^3F)$	$^3A_2T_2(^3F)$	$^3T_1T_1(^3P)$	$^3T_1E(^3P)$	$^3T_1T_2(^3P)$
$\frac{\sqrt{15}}{2}\lambda + \frac{\sqrt{15}}{6}(4\gamma - \tau)$	$\sqrt{10}(-\gamma + 2\tau)$	$-6\beta - \frac{11\gamma}{2} - 4\tau$	$\sqrt{6}(-\frac{5\gamma}{6} - 4\tau)$	$\sqrt{3}(\frac{5\gamma}{6} + 4\tau)$
$\frac{\sqrt{10}}{2}(4\gamma - \tau)$	$\frac{\sqrt{15}}{3}(2\gamma - 4\tau)$	$\sqrt{6}(-\frac{5\gamma}{6} - 4\tau)$	$-6\beta - \frac{14\gamma}{3}$	$-\frac{5\gamma\sqrt{2}}{6} - 4\tau\sqrt{2}$
$\sqrt{5}(2\gamma - \frac{\tau}{2})$	$\frac{\sqrt{30}}{6}(-2\gamma + 4\tau)$	$\sqrt{3}(\frac{5\gamma}{6} + 4\tau)$	$\sqrt{2}(-\frac{5\gamma}{6} - 4\tau)$	$-6\beta + \frac{\sqrt{2}}{6}(-23\gamma - 24\tau)$
$\frac{\sqrt{3}}{6}(10\gamma + 15\tau)$	$2\sqrt{2}\lambda$	$\frac{\sqrt{5}}{2}(3\gamma + 8\tau)$	$\sqrt{\frac{5}{6}}(3\gamma + 8\tau)$	$\sqrt{\frac{5}{12}}(-3\gamma - 8\tau)$
$\frac{\sqrt{2}}{6}(-10\gamma - 15\tau)$		$\sqrt{\frac{5}{6}}(+3\gamma + 8\tau)$		$\frac{\sqrt{10}}{2}(-3\gamma - 8\tau)$
$3\beta + \frac{\lambda}{2} + \frac{2\gamma}{3} - \frac{5\tau}{2}$		$\sqrt{\frac{5}{12}}(-3\gamma - 8\tau)$	$\frac{\sqrt{10}}{2}(-3\gamma - 8\tau)$	$\frac{\sqrt{5}}{2}(-3\gamma - 8\tau)$
	$18\beta + 14\gamma$	$\sqrt{2}(6\gamma - 30\tau)$	$\sqrt{3}(-4\gamma + 20\tau)$	$\sqrt{6}(2\gamma - 10\tau)$
		$\Delta_p - \lambda + 7\tau$	$-7\sqrt{6}\tau$	$+7\sqrt{3}\tau$
			$\Delta_p + \lambda$	$-7\sqrt{2}\tau$
				$\Delta_p + \lambda - 7\tau$

TABLE IV (continued)

A_1

$^3T_1A(^3F)$	$^3T_1T_2(^3F)$	$^3T_2T_2(^3F)$	$^3A_2T_2(^3F)$	$^3T_1A(^3P)$	$^3T_1T_2(^3P)$
$-9\beta + 3\lambda - 7\gamma$	$\sqrt{2}\ (-10\gamma - \tau)$	$-\frac{\sqrt{30}}{3}\ (4\gamma - \tau)$	$-\frac{2\sqrt{15}}{3}\ (\gamma - 2\tau)$	$-6\beta - \frac{14\gamma}{3}$	$\frac{5\gamma\sqrt{2}}{3} - 8\tau\sqrt{2}$
	$-9\beta - \frac{3\lambda}{2} + 3\gamma + \tau$	$\frac{\lambda\sqrt{15}}{2} - \frac{\sqrt{15}}{3}\ (4\gamma - \tau)$	$-\frac{2\sqrt{30}}{3}\ (\gamma - 2\tau)$	$\frac{5\gamma\sqrt{2}}{3} - 8\tau\sqrt{2}$	$-6\beta - \frac{11\gamma}{3} + \frac{8\tau}{3}$
		$3\beta - \frac{\lambda}{2} - \gamma - 5\tau$	$2\sqrt{2}\ \lambda$	$2\sqrt{\frac{5}{6}}\ (3\gamma - 8\tau)$	$\sqrt{\frac{5}{3}}\ (3\gamma - 8\tau)$
			$18\beta + 14\gamma$	$\sqrt{3}\ (4\gamma - 20\tau)$	$\sqrt{6}\ (-4\gamma + 15\tau)$
				$\Delta_p - 2\lambda$	$-14\sqrt{2}\ \tau$
					$\Delta_p + \lambda + 14\tau$

TABLE IV (continued)

A_2

$^3T_1T_1(^3F)$	$^3T_2A(^3F)$	$^3T_2T_1(^3F)$	$^3T_1T_1(^3P)$
$-9\beta + \frac{3\lambda}{2} - 17\gamma - \tau$	$-\frac{\sqrt{30}}{3}(4\gamma - \tau)$	$\frac{\sqrt{15}}{2}\lambda - \frac{\sqrt{15}}{3}(4\gamma - \tau)$	$-6\beta - 3\gamma - 8\tau$
	$3\beta - \lambda + \frac{7\gamma}{3}$	$\frac{\sqrt{2}}{3}(-10\gamma - 15\tau)$	$-\frac{\sqrt{30}}{3}(-3\gamma - 8\tau)$
		$3\beta + \frac{\lambda}{2} + \frac{7\gamma}{3}$	$-\frac{\sqrt{15}}{3}(-3\gamma - 8\tau)$
			$\Delta_p - \lambda - 14\tau$

*In this table $\gamma = -\frac{1}{3}D_4$ and $\tau = -\frac{\sqrt{5}}{10}D_2$

where the trigonal field parameters are defined as

$$D_4 = B_4^0 \langle r^4 \rangle / 14\sqrt{\pi}$$
$$D_2 = B_2^0 \langle r^2 \rangle / 14\sqrt{\pi} \qquad \text{(IV-11)}$$

The matrix elements of V_t in the (lm) representation are obtained using Table 1^6 of Reference (23). It is then a relatively easy task to calculate the matrix elements of V_t in the $\vec{L}\cdot\vec{S}$ representation and these are listed in Table 4. The energy matrix (in the absence of an external magnetic field) factorizes into blocks corresponding to A_1, A_2, and E. For magnetic susceptibilities below 500°K the contribution of the highly excited states is insignificant and will be neglected except for the mixing of the wave functions.

Up to this point the development is the same for CdS and ZnO crystals but because of the difference in magnitude of the trigonal matrix elements each of the host crystals will be considered separately.

Ni^{2+}:CdS

The optical studies reported by Weakliem[18] suggest that the environment of the Ni^{2+} ion in CdS is very nearly cubic because of the apparent isotropy of the optical spectrum. The same conclusion can also be reached from the small observed magnetic anisotropy (Table 1). The Hamiltonian

$$H' = H_o + V_c + \lambda\vec{L}\cdot\vec{S} \qquad \text{(IV-12)}$$

will first be diagonalized and then V_t will be treated by

first order perturbation. In order to diagonalize H' it is necessary to assign numerical values to β and to Δ_p ($^3F - {}^3P$ spacing). These values are obtainable from the optical spectra[18] and are taken as $\beta = -257\ cm^{-1}$ and $\Delta_p = 8550\ cm^{-1}$. This gives the F-P mixing coefficients as

$$a_1 = 0.991, \quad a_2 = 0.138 \qquad \text{(IV-13)}$$

The wave functions after considering this mixing can be written as

$$\Psi^o(^3F^3T_1A_1) = a_1\Psi(^3F^3T_1AA_1) + a_2\Psi(^3P^3T_1AA_1),$$

etc. The proper wave functions which eliminate $\lambda\vec{L}\cdot\vec{S}$ matrix elements between $^3T_1$ and $^3T_2$ can be expressed as a linear combination of the functions listed in Table 3, e.g.,

$$\Psi'(^3F^3T_1T_1A_2) = c\Psi^o(^3F^3T_1T_1A_2) + d\Psi^o(^3F^3T_2T_1A_2)$$

or

$$\Psi'(^3F^3T_1T_1A_2) = c[a_1\Psi(^3F^3T_1T_1A_2) + a_2\Psi(^3P^3T_1T_1A_2)] + d\Psi(^3F^3T_2T_1A_2)$$

since one element connects at most two of the functions. These wave functions are listed in Table 5 for the $^3T_1$ and $^3T_2$ levels.

In order to calculate the magnetic susceptibility using the standard formula of Van Vleck[3] (Equation I-13) it is necessary to calculate the matrix elements of the Hamiltonian

TABLE 5

PROPER WAVE FUNCTIONS (Ni^{2+}:CdS) FOR $^3T_1(^3F)$ AND $^3T_2(^3F)$

$^3T_1$

$$\Psi'(^3F^3T_1A_1) = \Psi^o(^3F^3T_1A_1)$$

$$\Psi'(^3F^3T_1T_1A_2) = c\Psi^o(^3F^3T_1T_1A_2) + d\Psi^o(^3F^3T_2T_1A_2)$$

$$\Psi'(^3F^3T_1T_1E_1) = c\Psi^o(^3F^3T_1T_1E_1) + d\Psi^o(^3F^3T_2T_1E_2)$$

$$\Psi'(^3F^3T_1T_1E_2) = c\Psi^o(^3F^3T_1T_1E_2) + d\Psi^o(^3F^3T_2T_1E_1)$$

$$\Psi'(^3F^3T_1EE_1) = p\Psi^o(^3F^3T_1EE_1) + q\Psi^o(^3F^3T_2EE_1)$$

$$\Psi'(^3F^3T_1EE_2) = p\Psi^o(^3F^3T_1EE_2) - q\Psi^o(^3F^3T_2EE_2)$$

$$\Psi'(^3F^3T_1T_2A_1) = m\Psi^o(^3F^3T_1T_2A_1) + n\Psi^o(^3F^3T_2T_2A_1)$$

$$\Psi'(^3F^3T_1T_2E_1) = m\Psi^o(^3F^3T_1T_2E_1) + n\Psi^o(^3F^3T_2T_2E_2)$$

$$\Psi'(^3F^3T_1T_2E_1) = m\Psi^o(^3F^3T_1T_2E_2) + n\Psi^o(^3F^3T_2T_2E_1)$$

$^3T_2$

$$\Psi'(^3F^3T_2A_2) = \Psi^o(^3F^3T_2A_2)$$

$$\Psi'(^3F^3T_2T_1A_2) = d\Psi^o(^3F^3T_1T_1A_2) - c\Psi^o(^3F^3T_2T_1A_2)$$

$$\Psi'(^3F^3T_2T_1E_1) = d\Psi^o(^3F^3T_1T_1E_1) - c\Psi^o(^3F^3T_2T_1E_2)$$

$$\Psi'(^3F^3T_2T_1E_2) = d\Psi^o(^3F^3T_1T_1E_2) - c\Psi^o(^3F^3T_2T_1E_1)$$

$$\Psi'(^3F^3T_2EE_1) = q\Psi^o(^3F^3T_1EE_1) - p\Psi^o(^3F^3T_2EE_1)$$

TABLE 5 (continued)

$$\Psi'(^3F^3T_2EE_2) = -q\Psi^o(^3F^3T_1EE_2) - p\Psi^o(^3F^3T_2EE_2)$$

$$\Psi'(^3F^3T_2T_2A_1) = n\Psi^o(^3F^3T_1T_2A_1) - m\Psi^o(^3F^3T_2T_2A_1)$$

$$\Psi'(^3F^3T_2T_2E_1) = n\Psi^o(^3F^3T_1T_2E_1) - m\Psi^o(^3F^3T_2T_2E_2)$$

$$\Psi'(^3F^3T_2T_2E_2) = n\Psi^o(^3F^3T_1T_2E_2) - m\Psi^o(^3F^3T_2T_2E_1)$$

$c = 0.995$

$d = 0.098$

$p = 0.981$

$q = 0.194$, for $\lambda = -170\ cm^{-1}$

$m = 0.994$

$n = 0.110$

$$H_m = \mu_o(\vec{L} + g_s\vec{S})\cdot\vec{H}$$

The matrix elements of the components of the angular momentum $\vec{L}$ can be calculated with the use of the equations[27]

$$(LM|L_z|LM) = Mh/2\pi$$

$$(L\ M+1\ |L_x|\ L\ M) = \tfrac{1}{2}\{(L-M)(L+M+1)\}^{\frac{1}{2}}h/2\pi$$

$$(L\ M-1\ |L_x|\ L\ M) = \tfrac{1}{2}\{(L+M)(L-M+1)\}^{\frac{1}{2}}h/2\pi$$

in the (LM) representation. These matrix elements for the orbital angular momentum $\vec{L}$ and the spin angular momentum $\vec{S}$ are listed in Appendix VI for the ^3P and the ^3F levels in the (LM) and the cubic representation. Matrix elements of $|\vec{L} + 2\vec{S}|$ in the $\vec{L}\cdot\vec{S}$ representation are listed in Table 6.

To calculate the mixing coefficients for the proper wave functions it is necessary to solve the two by two matrices where the $^3T_1$ levels are connected to the $^3T_2$ through $\lambda\vec{L}\cdot\vec{S}$. This requires that a numerical value be given to λ. Values of λ between -150 and -300 cm^{-1} were taken. The solution of the 2 X 2 matrices gave the eigenvalues and the eigenvectors. The components of the eigenvectors, of course, gave the mixing coefficients and the eigenvalues gave the energy levels before the trigonal components are considered. The magnetic susceptibilities for a magnetic field parallel to the trigonal axis ($\chi_{\parallel}$) and perpendicular ($\chi_{\perp}$) to it were calculated using Equation (I-13) for each value of λ and K = A + B which measured the trigonal splitting. Values

TABLE 6

MATRIX ELEMENTS OF $|\vec{L} + 2\vec{S}|$ IN THE $\vec{L}\cdot\vec{S}$ REPRESENTATION

$|L_z + 2S_z|$

^3F

$^3T_1T_1E_1$	$^3T_1EE_1$	$^3T_1T_2E_2$	$^3T_2T_2E_1$	$^3T_2EE_1$	$^3T_2T_1E_2$	$^3A_2E_1$
1/4	$-7(6)^{\frac{1}{2}}/12$	$7(3)^{\frac{1}{2}}/3$	$(5)^{\frac{1}{2}}/4$	$-(30)^{\frac{1}{2}}/4$	$(15)^{\frac{1}{2}}/4$	
		$-(2)^{\frac{1}{2}}/4$	$-(30)^{\frac{1}{2}}/4$		$-(10)^{\frac{1}{2}}/4$	
		$-1/4$	$(15)^{\frac{1}{2}}/4$	$-(10)^{\frac{1}{2}}/4$	$-(5)^{\frac{1}{2}}/4$	
			$5/4$	$-(6)^{\frac{1}{2}}/4$	$(3)^{\frac{1}{2}}/4$	$(2)^{\frac{1}{2}}$
					$-5(2)^{\frac{1}{2}}/4$	$-2(6)^{\frac{1}{2}}/3$
					$5/4$	$(6)^{\frac{1}{2}}/3$
						2

	$^3T_1AA_1$	$^3T_1T_2A_1$	$^3T_2T_2A_1$	$^3A_2T_2A_1$
$^3T_1T_1A_2$	$-7(6)^{\frac{1}{2}}/6$			
$^3T_2AA_2$		$-(10)^{\frac{1}{2}}/2$	$-(6)^{\frac{1}{2}}/2$	$2(3)^{\frac{1}{2}}/3$
$^3T_2T_1A_2$	$-(10)^{\frac{1}{2}}/2$	$(5)^{\frac{1}{2}}/2$	$-(3)^{\frac{1}{2}}/2$	$-2(6)^{\frac{1}{2}}/6$

TABLE 6 (continued)

^3P

$^3T_1T_1E_1$	$^3T_1EE_1$	$^3T_1T_2E_2$
3/2	$-(6)^{\frac{1}{2}}/6$	$(3)^{\frac{1}{2}}/6$
		$-3(2)^{\frac{1}{2}}/2$
		-3/2

	$^3T_1AA_1$	$^3T_1T_2A_1$
$^3T_1T_1A_2$	$-(6)^{\frac{1}{2}}/3$	$-(3)^{\frac{1}{2}}/3$

$|L_x + 2S_x|$

^3P

	$^3T_1A_1A_1$	$^3T_1T_1A_2$	$^3T_1T_2A_1$	$^3T_1T_1E_2$	$^3T_1EE_2$	$^3T_1T_2E_1$
$^3T_1T_1E_1$	$(3)^{\frac{1}{2}}/3$	$3(2)^{\frac{1}{2}}/4$	$-(6)^{\frac{1}{2}}/12$		$(3)^{\frac{1}{2}}/6$	$(6)^{\frac{1}{2}}/6$
$^3T_1EE_1$		$(3)^{\frac{1}{2}}/6$	3/2	$(3)^{\frac{1}{2}}/6$		3/2
$^3T_1T_2E_2$		$-(6)^{\frac{1}{2}}/12$	$-3(2)^{\frac{1}{2}}/4$	$(6)^{\frac{1}{2}}/6$	-3/2	

TABLE 6 (continued)

	^3F						
	$^3T_1T_1E_1$	$^3T_1EE_1$	$^3T_1T_2E_2$	$^3T_2T_2E_1$	$^3T_2EE_1$	$^3T_2T_1E_2$	$^3A_2E_1$
$^3T_1AA_1$	$7(3)^{\frac{1}{2}}/6$					$(5)^{\frac{1}{2}}/2$	
$^3T_1T_1A_2$	$(2)^{\frac{1}{2}}/8$	$7(3)^{\frac{1}{2}}/12$	$-7(6)^{\frac{1}{2}}/24$	$-(10)^{\frac{1}{2}}/8$	$(15)^{\frac{1}{2}}/4$	$(30)^{\frac{1}{2}}/8$	
$^3T_1T_2A_1$	$-7(6)^{\frac{1}{2}}/24$	$1/4$	$-(2)^{\frac{1}{2}}/8$	$(30)^{\frac{1}{2}}/8$	$(5)^{\frac{1}{2}}/4$	$(10)^{\frac{1}{2}}/8$	
$^3T_2A_2A_2$			$(5)^{\frac{1}{2}}/2$	$(3)^{\frac{1}{2}}/3$			$-(6)^{\frac{1}{2}}/3$
$^3T_2T_2A_1$	$-(10)^{\frac{1}{2}}/8$	$(15)^{\frac{1}{2}}/4$	$(30)^{\frac{1}{2}}/8$	$5(2)^{\frac{1}{2}}/8$	$(3)^{\frac{1}{2}}/4$	$-(6)^{\frac{1}{2}}/8$	1
$^3T_2T_1A_2$	$(30)^{\frac{1}{2}}/8$			$-(6)^{\frac{1}{2}}/8$	$5/4$		$-(3)^{\frac{1}{2}}/3$
$^3A_2A_1$				1	$(6)^{\frac{1}{2}}/3$	$(3)^{\frac{1}{2}}/3$	$(2)^{\frac{1}{2}}$
$^3T_1T_1E_2$		$7(3)^{\frac{1}{2}}/12$	$7(6)^{\frac{1}{2}}/12$	$(10)^{\frac{1}{2}}/4$	$(15)^{\frac{1}{2}}/4$		
$^3T_1EE_2$	$7(3)^{\frac{1}{2}}/12$		$-1/4$	$-(15)^{\frac{1}{2}}/4$		$(5)^{\frac{1}{2}}/4$	
$^3T_1T_2E_1$	$7(6)^{\frac{1}{2}}/12$	$1/4$			$(5)^{\frac{1}{2}}/4$	$-(10)^{\frac{1}{2}}/4$	
$^3T_2T_2E_2$	$(10)^{\frac{1}{2}}/4$	$(15)^{\frac{1}{2}}/4$			$(3)^{\frac{1}{2}}/4$	$-(6)^{\frac{1}{2}}/4$	
$^3T_2EE_2$	$-(15)^{\frac{1}{2}}/4$		$(5)^{\frac{1}{2}}/4$	$(3)^{\frac{1}{2}}/4$		$-5/4$	$(6)^{\frac{1}{2}}/3$
$^3T_2T_1E_1$		$(5)^{\frac{1}{2}}/4$	$-(10)^{\frac{1}{2}}/4$	$-(6)^{\frac{1}{2}}/4$			$2(3)^{\frac{1}{2}}/3$
$^3A_2E_2$					$-(6)^{\frac{1}{2}}/3$	$2(3)^{\frac{1}{2}}/3$	

of $\lambda = -170\ cm^{-1}$ and $K = -20\ cm^{-1}$ were found to fit the magnetic data best and a graph of χ versus $(1/T)$ using these parameters is shown in Figure 5.

At low temperatures both $\chi_{\parallel}$ and $\chi_{\perp}$ approach asymptotic values which are determined by the Van Vleck temperature independent part of the paramagnetic susceptibility. Since the ground state is A_1 and since μ_z connects this state with only the A_2 states then $\chi_{\parallel}$ at low temperatures is determined by

$$\chi_{\parallel} = \frac{2N\mu_o^2 \mid (A_1 \mid \mu_z \mid A_2) \mid^2}{E_{A_2} - E_{A_1}}$$

where, of course, matrix elements to levels outside the ground manifold are ignored since they are extremely small. Similarly, μ_x connects A_1 with only the T_1E states and

$$\chi_{\perp} = \frac{4N\mu_o^2 \mid (A_1 \mid \mu_x \mid T_1E) \mid^2}{E_{T_1E} - E_{A_1}}$$

As the temperature is increased the higher levels become populated which results in χ being temperature dependent and enables one to obtain the trigonal splitting of the T_1 level.

An analysis of the magnetic data is, therefore, instrumental in determining certain of the crystal parameters. First, the spin orbit coupling constant was determined to be $-170\ cm^{-1} \pm 10\ cm^{-1}$ which is considerably less than the free ion value of $-340\ cm^{-1}$. With this value of λ and the

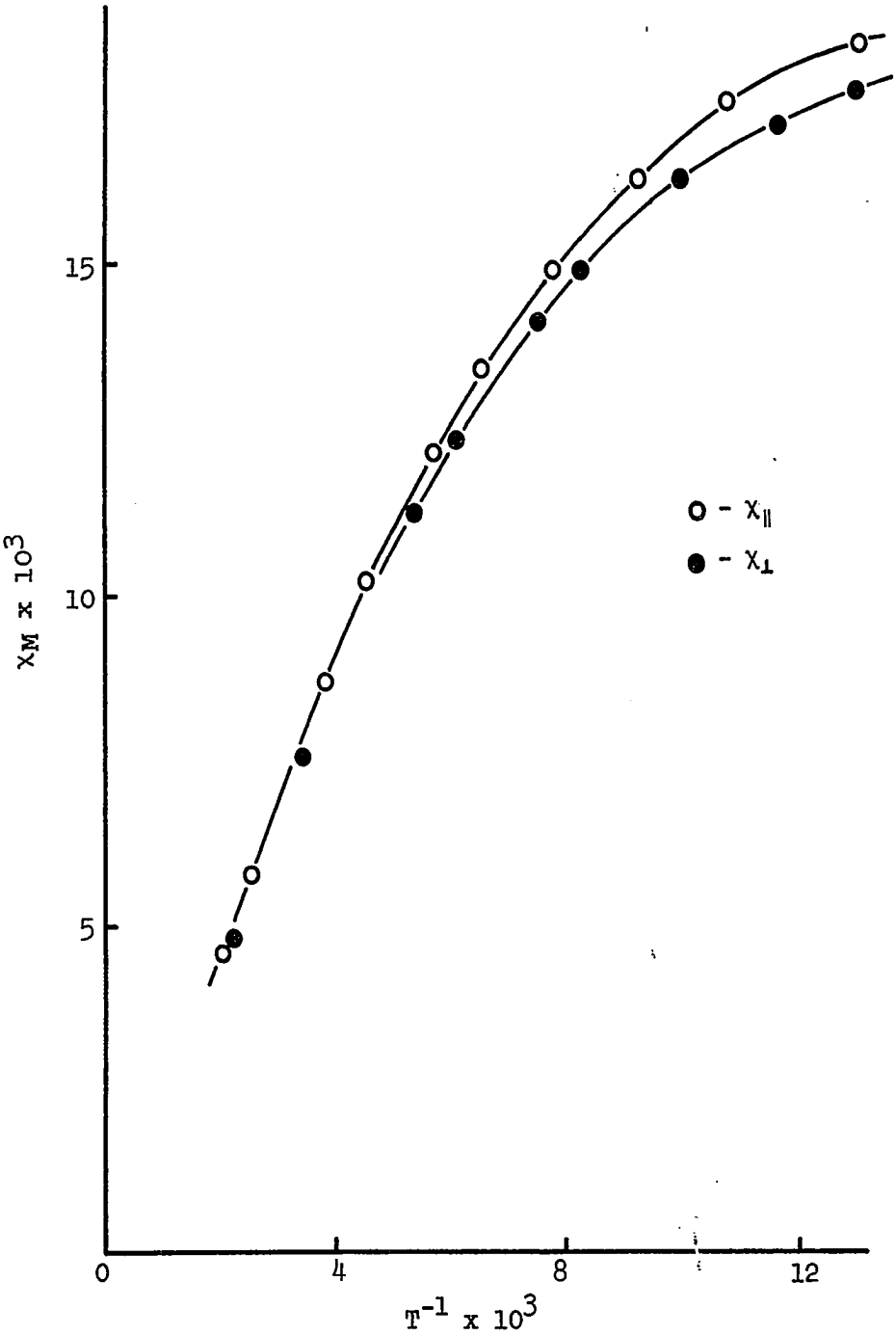

Figure 5. Magnetic Susceptibilities (Per Gm-Ion) of Ni^{2+}:CdS

trigonal splittings the energy levels of the ground state can be calculated. Since $K \cong -20\ cm^{-1}$ and since

$$K = 10D_4 + (3/10)(5)^{\frac{1}{2}}D_2 \qquad \text{(IV-15)}$$

then $D_4 \cong -2\ cm^{-1}$ if $D_2 \cong 0$ as appears to be the case from the optical spectra.[18]

$$Ni^{2+}:ZnO$$

The optical studies of Weakliem[18] indicate that the trigonal component of Ni^{2+} in ZnO is considerably larger than in the case of Ni^{2+} in CdS. The magnetic data (Table 2) show that this is indeed the case. The crystal structure also indicates a larger trigonal component for the ZnO crystal. Preliminary estimates showed that the trigonal component was of the same order of magnitude as the spin orbit component and, therefore, the same type of scheme used in solving the CdS energy matrix could not be used.

In setting up the energy matrix (excluding the magnetic field terms) the $\vec{L}\cdot\vec{S}$ representation is used but the ^3P states are not included, primarily, because of the greater difficulty in setting up the computer program. Even in the case of Ni^{2+} in CdS, where the mixing is larger, the contribution from the ^3P-^3F mixing to the magnetic susceptibility was found to be extremely small. Also, the accuracy of the magnetic data for the ZnO is not as great as for the CdS crystal and the mixing of the ground levels through V_t is so great that it completely overshadows the ^3P-^3F mixing.

The complete computer program, which was set up and run by Segraves, consisted of several smaller programs. First, a program to calculate the elements of the energy matrix, which was factorized into a (3 X 3), a (4 X 4), and two (7 X 7) matrices, was set up; second, a program was used to calculate the eigenvectors and the eigenvalues of the energy matrix; third, an extremely long program was set up to calculate μ_x and μ_z which in the case of the E states contained 49 terms; and, finally, a program was set up to calculate $\chi_{\|}$ and $\chi_{\perp}$ for the temperatures between 20°K and 1000°K. The program was designed so that λ, K, and D_2 could be varied but it was found that D_2 alone did not change the theoretical calculations significantly as long as K was kept constant. D_2 was kept at 6 cm^{-1} for these calculations. It was found that λ = -175 cm^{-1} and K = -225 cm^{-1} gave the best fit to the magnetic data and a graph of χ versus (1/T) using these parameters is shown in Figure 6. The proper wave functions for the $^3T_1$ levels are given in Table 7. The matrix elements and susceptibility equations are given in Appendix IX. As with the case of CdS it is found that $\chi_{\|}$ and $\chi_{\perp}$ approach constant values for low temperatures and as the difference in these values is quite large it is expected that the T_1 level is split considerably. For the above values of λ and K it turns out that the T_1 splitting is about 100 cm^{-1} as compared to 10 cm^{-1} for CdS. The error in λ and K is estimated to be about $\pm$ 25 cm^{-1}. From the experimental value of K and its definition in terms of D_4 and D_2 it is found that D_4 = -23 cm^{-1}.

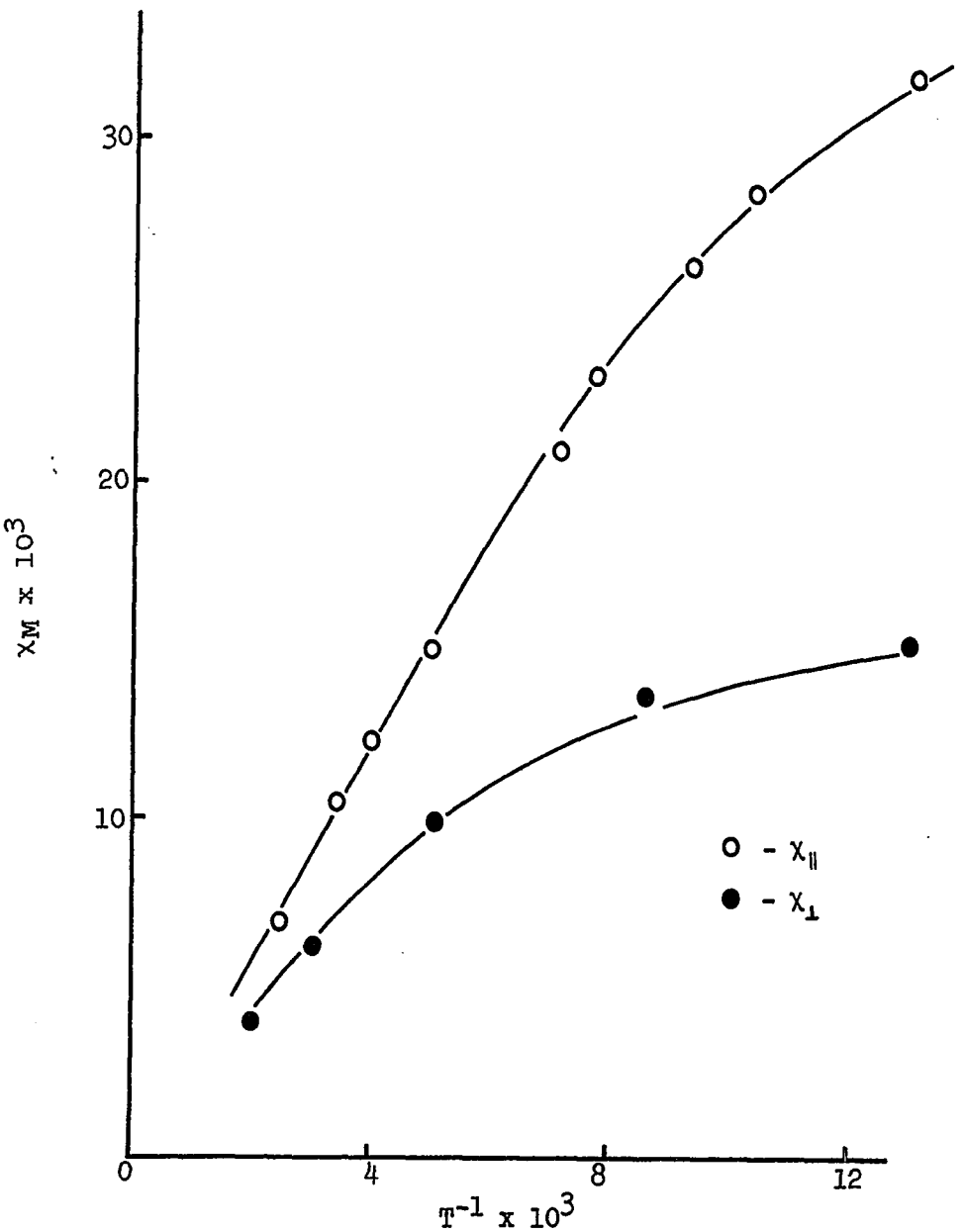

Figure 6. Magnetic Susceptibilities (Per Gm-Ion) of Ni^{2+}:ZnO

TABLE 7

PROPER WAVE FUNCTIONS (Ni^{2+}:ZnO) FOR $^3T_1(^3F)$ (λ = -170 cm^{-1})

$$\Psi'(^3F^3T_1A_1A_1) = 0.99066\Psi(^3F^3T_1A_1A_1) + 0.13267\Psi(^3F^3T_1T_2A_1) + 0.03086\Psi(^3F^3T_2T_2A_1) + 0.00588\Psi(^3F^3A_2T_2A_1)$$

$$\Psi'(^3F^3T_1T_1A_2) = 0.99377\Psi(^3F^3T_1T_1A_2) + 0.01550\Psi(^3F^3T_2A_2A_2) + 0.11039\Psi(^3F^3T_2T_1A_2)$$

$$\Psi'(^3F^3T_1T_1E_1) = 0.96988\Psi(^3F^3T_1T_1E_1) + 0.19056\Psi(^3F^3T_1EE_1) - 0.11377\Psi(^3F^3T_1T_2E_2) + 0.00304\Psi(^3F^3T_2T_2E_1) + 0.04375\Psi(^3F^3T_2EE_1) + 0.09024\Psi(^3F^3T_2T_1E_2) + 0.00478\Psi(^3F^3A_2T_2E_1)$$

$$\Psi'(^3F^3T_1T_1E_2) = 0.96988\Psi(^3F^3T_1T_1E_2) + 0.19056\Psi(^3F^3T_1EE_2) - 0.11377\Psi(^3F^3T_1T_2E_1) + 0.00304\Psi(^3F^3T_2T_2E_2) + 0.04375\Psi(^3F^3T_2EE_2) + 0.09024\Psi(^3F^3T_2T_1E_1) + 0.00478\Psi(^3F^3A_2T_2E_2)$$

$$\Psi'(^3F^3T_1EE_1) = -0.08861\Psi(^3F^3T_1T_1E_1) + 0.78518\Psi(^3F^3T_1EE_1) + 0.59115\Psi(^3F^3T_1T_2E_2) + 0.06616\Psi(^3F^3T_2T_2E_1) + 0.14404\Psi(^3F^3T_2EE_1) - 0.03253\Psi(^3F^3T_2T_1E_2) + 0.00220\Psi(^3F^3A_2T_2E_1)$$

$$\Psi'(^3F^3T_1EE_2) = -0.08861\Psi(^3F^3T_1T_1E_2) + 0.78518\Psi(^3F^3T_1EE_2) + 0.59115\Psi(^3F^3T_1T_2E_1) + 0.06616\Psi(^3F^3T_2T_2E_2) + 0.14404\Psi(^3F^3T_2EE_2) -$$

TABLE 7 (continued)

$$0.03253\Psi(^3F^3T_2T_1E_1) + 0.00220\Psi(^3F^3A_2T_2E_2)$$

$$\Psi'(^3F^3T_1T_2A_1) = -0.13555\Psi(^3F^3T_1A_1A_1) + 0.98268\Psi(^3F^3T_1T_2A_1) + 0.12633\Psi(^3F^3T_2T_2A_1) + 0.00096\Psi(^3F^3A_2T_2A_1)$$

$$\Psi'(^3F^3T_1T_2E_1) = 0.20493\Psi(^3F^3T_1T_1E_1) - 0.55472\Psi(^3F^3T_1EE_1) + 0.79078\Psi(^3F^3T_1T_2E_2) + 0.08589\Psi(^3F^3T_2T_2E_1) - 0.12955\Psi(^3F^3T_2EE_1) + 0.02495\Psi(^3F^3T_2T_1E_2) + 0.01354\Psi(^3F^3A_2T_2E_1)$$

$$\Psi'(^3F^3T_1T_2E_2) = 0.20493\Psi(^3F^3T_1T_1E_2) - 0.55472\Psi(^3F^3T_1EE_2) + 0.79078\Psi(^3F^3T_1T_2E_1) + 0.08589\Psi(^3F^3T_2T_2E_2) - 0.12955\Psi(^3F^3T_2EE_2) + 0.02495\Psi(^3F^3T_2T_1E_1) + 0.01354\Psi(^3F^3A_2T_2E_2)$$

Point Charge Calculations

If it is assumed that the surrounding ions of a particular cation can be considered to be point charges then it is quite a simple matter, in principle, to calculate the crystal field parameters D_q, D_4, and D_2 for a single crystal if the potential at a point (r, θ, φ) due to an ion located at (R, α, β) is expressed as a series of spherical harmonics.[28] The potential at (r, θ, φ) is then obtained by summing over all ions. This leads to Equations (IV-7 and IV-11) for V_t and V_c where

$$B_2^o = qe(\pi/5)^{\frac{1}{2}} \sum_i \frac{3\cos^2 \alpha_i - 1}{R_i^3}$$

$$B_4^o = \frac{qe(8\pi)^{\frac{1}{2}}}{9} \left\{ \sum_i \frac{3(2)^{\frac{1}{2}}[35\,\mathrm{Cos}^4 \alpha_i - 30\,\mathrm{Cos}^2 \alpha_i + 3]}{16\,R_i^5} + \right.$$

$$\left. \sum_i \frac{21\,\mathrm{Cos}\,\alpha_i\,\mathrm{Sin}^3 \alpha_i}{8\,R_i^5} \right\}$$

with

$$D_q = (-3/2)(1/14\sqrt{\pi})\langle r^4 \rangle qe(8\pi/81)^{\frac{1}{2}} \left\{ (-21/8) \sum_i \frac{\mathrm{Cos}\,\alpha_i\,\mathrm{Sin}^3 \alpha_i}{R_i^5} \right\},$$

$$D_4 = B_4^o \langle r^4 \rangle / 14\sqrt{\pi} \ ,$$

and (IV-16)

$$D_2 = B_2^o \langle r^2 \rangle / 14\sqrt{\pi}$$

The summations have been carried out to 20 Å for Dq and D_4 and out to 30 Å for D_2 is the case of ZnO by C. F. Dorman using a 1410 Computer. Unfortunately, using Watson's H-F wave functions[18] Weakliem found $\langle r^4 \rangle = 3.021$ for Ni^{2+} which gives a value which is much too low for Dq and D_4. If, however, the ratio of D_4/Dq is calculated and the experimental value of Dq is used then D_4 can be determined from Equation (IV-17). For D_2 it is necessary to use the value of $\langle r^2 \rangle = 1.133$ which was obtained using the H-F wave functions. This is not expected to give quantitative agreement with experiment.

For Ni^{2+}:ZnO it is found that $D_4 = -41$ cm^{-1} and $D_2 = -1.9$ cm^{-1} if all the ions out to 20 Å are considered. By moving the cation by +0.01 Å along the trigonal axis D_4 can be increased to only about -33 cm^{-1} and movement in any direction from this position decreases D_4. If, however, the three equivalent oxygen anions are moved towards the cation site by 0.027 Å relative to the unique anion on the trigonal axis, D_4 is reduced to -23 cm^{-1} which is the experimental value. This contraction of the lattice had been suggested by Weakliem[18] for Ni^{2+}:CdS to help explain its apparent optical isotropy. For the above contraction D_2 is calculated to be 24 cm^{-1} as compared to 10 cm^{-1} found experimentally. The values of D_4, D_2, and Dq using all the ions within a certain radius and no displacement of the cation, are

R_{max}	D_4 (cm^{-1})	D_2 (cm^{-1})	Dq (cm^{-1})
2 Å	-34	+11	$555\langle r^4\rangle$
8 Å	-43	-113	$534\langle r^4\rangle$
20 Å	-41	-2	$533\langle r^4\rangle$
21 Å	-42	-14	$533\langle r^4\rangle$
22 Å	-42	-7	$533\langle r^4\rangle$
30 Å		-4	
31 Å		-11	

The D_4 calculations were not extended further than 22 Å because of the convergence around -41 cm^{-1}. However, the values of D_2 are still varying considerably and the calculations were extended to 31 Å but the convergence is still poor because of the R^{-3} dependence. To obtain proper convergence the calculations should be extended to at least 100 Å which would require a tremendous amount of computer time. In view of the large uncertainty in the $\langle r^2\rangle$ calculation, the calculation to 100 Å is not justifiable.

If only the first layer of anions is used for the Ni^{2+}:CdS crystal then D_4 is found to be -8 cm^{-1} as compared to the experimental value of -2 cm^{-1}. In this case a contraction of 0.017 Å of the three nearest equivalent anions gives D_4 = -3 cm^{-1}. D_2 is nearly zero both experimentally and as calculated from the point charge model.

The contraction of a lattice when a substituent is added has been studied by Title[29] and by Kikuchi and Azarbayejani[30] in which a tentative model was proposed which

required a lattice expansion if the ionic radius of the substituent is greater than the host cation and a lattice contraction if it is less. The fact that the ionic radius of Ni^{2+} (0.70 Å) is less than that of Zn^{2+} (0.74 Å) and Cd^{2+} (0.94 Å) tends to substantiate the assumption of the contraction of the lattice for both ZnO and CdS crystals.

Discussion

The rather large reduction of the spin orbit coupling constant of Ni^{2+} in both crystals (-170 and -175 cm^{-1}) from the free ion value λ_o (-340 cm^{-1}) suggests that there is considerable covalent bonding present. Using a simple molecular orbital (MO) picture for the bonding between the nickel and the oxygen or sulfur ions, Tinkham[31] demonstrated that the ratio of λ/λ_o was equal to the product of the normalization constants of the LCAO of the unpaired electrons. A more exact calculation is almost impossible without making specific assumptions concerning the potential and the details of the wave functions. Experimentally it is found that

$$\left.\begin{aligned} N^2 &= 0.50 \\ N^2 &= 0.52 \end{aligned}\right\}, \quad \begin{aligned} &\text{CdS} \\ &\text{ZnO} \end{aligned}.$$

From the optical spectra[18] one can also determine B from the value of Δ_p which is given by 15B where B is the Racah coefficient defined by[18]

$$B = F_2 - 5F_4$$

Taking the free ion value of B as $B_0 = 1020\ cm^{-1}$ and B for the ZnO crystal as $770\ cm^{-1}$ (for CdS, B = 570) one finds the ratio of B/B_0 as

$$\left.\begin{aligned} B/B_0 &= 0.75 \\ B/B_0 &= 0.56 \end{aligned}\right\} \quad \begin{aligned} &Ni^{2+}:ZnO \\ &Ni^{2+}:CdS \end{aligned} .$$

While a simple model would indicate that B should be reduced by N^4 it has been found experimentally that for most 3d group elements, in octahedral symmetry at least, (B/B_0) is actually greater than (λ/λ_0).[33]

Since detailed calculations are not feasible at this time we can only conclude that there is covalent bonding present but that, nevertheless, the crystal field theory is able (using λ as an adjustable parameter) to account reasonably well for the magnetic data.

CHAPTER V

V^{3+} IN CORUNDUM

Recent work on the optical absorption spectra and the electron spin resonance experiments of the dilute crystalline salts of the transition elements has provided much information about the energy levels, the crystalline field, and the possible distortion of the geometry of the crystals due to impurity substitution.[34-38] For instance, in the case of the vanadium (V^{3+}) doped corundum crystals, the crystalline structure is primarily cubic with a small trigonal distortion[34,36] with electronic energy levels as shown in Figure 7. The $^3T_1$ state in the cubic field is split by the trigonal field into $^3A_2$ and ^3E levels with energy spacing Δ_T. The spin orbit coupling further splits the ground $^3A_2$ state into two components separated by δ, the zero-field splitting. The two parameters Δ_T and δ have been determined from the electron spin resonance absorption and from the optical spectra.[34-39] From the magnitudes of such crystal field parameters along with the intensities of the optical spectral bands for several transition metal ions in corundum single crystals, McClure was able to examine the validity of the point charge model of the crystal field theory as well as

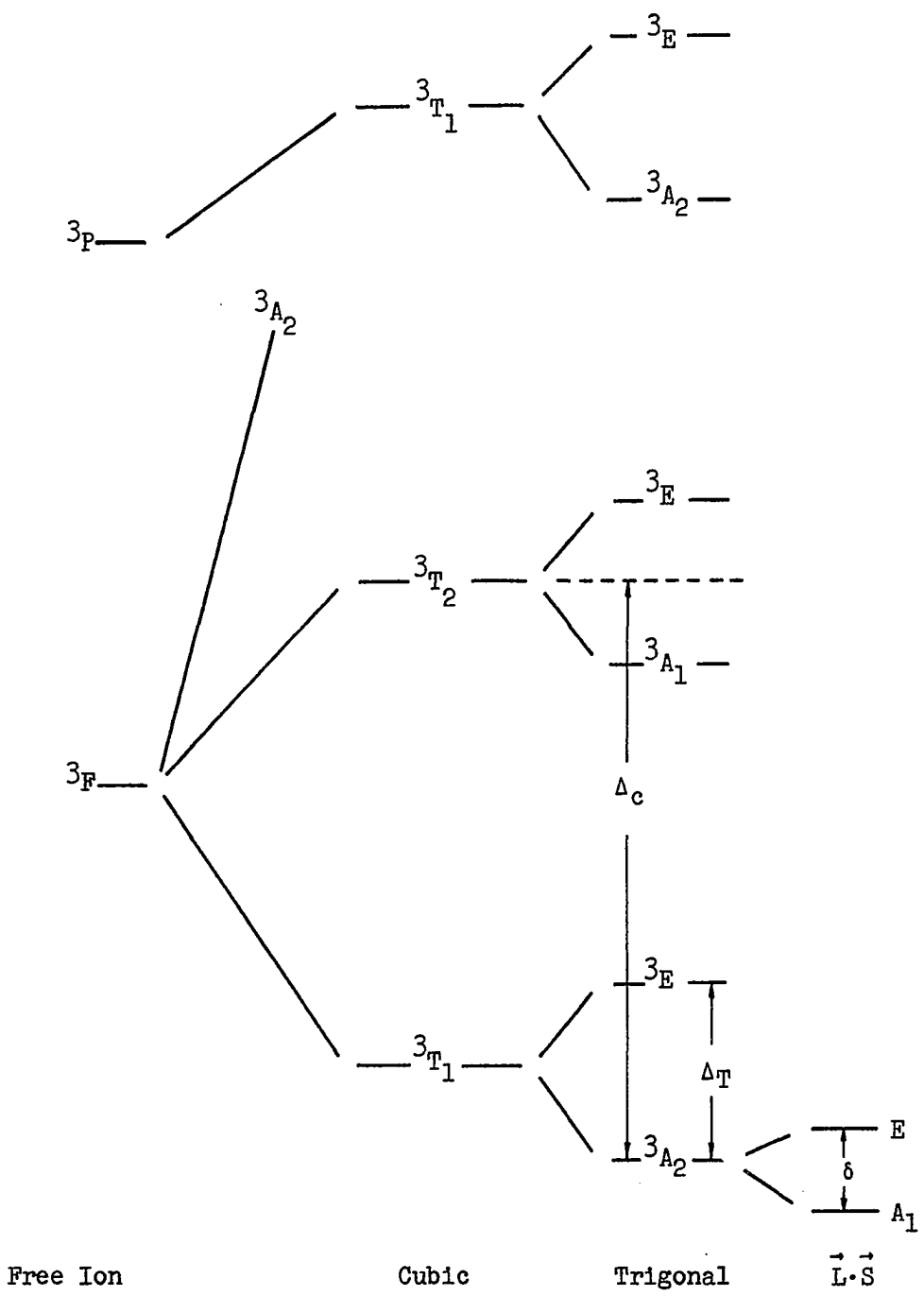

Figure 7. Energy Levels of V^{3+} in a Trigonal Field

the possibility of a slight shift of the sites of the impurity cations.[34] However, in most of the experiments, Δ_T and δ are generally determined from the temperature variations of the absorption intensity of the ESR and optical spectra. The difficulty of intensity measurements has greatly limited the accuracy of the values of these parameters. Thus Δ_T was given as 280 to 400 cm^{-1} from the ESR data in contrast to the optical results of 960 to 1200 cm^{-1}. The magnetic susceptibilities of the V^{3+}-doped corundum crystals have been measured from liquid helium temperature to 500°K along and perpendicular to the trigonal axis, from which Δ_T and δ are evaluated. Also an estimate of the spin-orbit coupling constant is obtained.

The magnetic properties of pure V_2O_3 have been investigated by several authors. The pure vanadium sesquioxide crystals become antiferromagnetic[40] at about 168°K. The use of diluted crystals makes it possible to study the paramagnetism at lower temperatures and provides more information about the crystalline field.

The magnetic susceptibility of vanadium alum has been investigated by Siegert and by van der Handel and Siegert.[41] Their measurements were made only for the average susceptibilities over the three crystalline axes. From the analysis of magnetic data Siegert and van der Handel have obtained a set of values for Δ_T and δ. Although the accuracy of the two parameters reported by these authors is limited by the

fact that all the susceptibility measurements were made below 300°K and that the mixing between the ^3F and ^3P states has been neglected in Siegert's theory, their results do lead to the significant conclusion that in vanadium alum the ground state, which resulted from the trigonal field splitting, is the $^3A_2$.

Experiment

The crystals of the V^{3+}-doped corundum were furnished by Dr. D. S. McClure.[34] Crystals of two different concentrations (0.092% and 0.73%) have been measured. The susceptibilities of both crystals have been measured for temperatures above 77°K. At lower temperatures the susceptibilities become so large that only the dilute sample was used.

The magnetic susceptibilities along the crystalline axes were measured by the Faraday balance. At very low temperature the magnetic anisotropy becomes so large that the geometrical configuration in which the trigonal axis of the crystal lies parallel to the magnetic field, is unstable. Thus $\chi_\perp$ has been measured from 500°K down to liquid helium temperature, but measurements of $\chi_\parallel$ are limited only to temperatures above 12°K. The magnetic susceptibilities (per gram sample) of V^{3+}-doped corundum are given in Table 8 and χ_i versus $(T + \theta_i)^{-1}$ is plotted in Figure 8 for the more concentrated sample for the 77-500°K temperature range where

$$\theta_\parallel = (\delta/3k) \qquad \text{and} \qquad \theta_\perp = (-\delta/6k) \qquad \text{(V-1)}$$

δ was taken as 8 cm^{-1} for this graph.[21,42]

TABLE 8

MAGNETIC SUSCEPTIBILITIES (PER GM. SAMPLE)
OF V^{3+}-DOPED CORUNDUM

Sample A. Concentration (0.73%)			
T°K	$\chi_{\parallel} \times 10^7$ (cgs-emu)	T°K	$\chi_{\perp} \times 10^7$ (cgs-emu)
77.3	4.70	77.3	4.08
88.0	3.68	88.0	3.23
91.0	3.49	103	2.26
121	1.92	109	1.96
127	1.68	118	1.60
138	1.25	130	1.11
145	1.04	137	0.89
155	0.75	145	0.72
156	0.73	154	0.49
202	-0.26	174	0.15
272	-0.93	217	-0.46
290	-1.14	253	-0.84
296	-1.16	296	-1.17
470	-1.96	430	-1.68
507	-2.11	501	-1.88

TABLE 8 (continued)

Sample B. Concentration (0.092%)			
T°K	$\chi_{\parallel}$ x 10^7 (cgs-emu)	T°K	$\chi_{\parallel}$ x 10^7 (cgs-emu)
295	-3.25	96.0	-2.61
282	-3.23	77.3	-2.39
134	-2.88	12.2	1.23

Sample B. Concentration (0.092%)			
T°K	$\chi_{\perp}$ x 10^7 (cgs-emu)	T°K	$\chi_{\perp}$ x 10^7 (cgs-emu)
295	-3.28	21.5	0.11
179	-3.12	18.6	0.80
125	-2.91	18.0	1.08
95	-2.70	16.0	1.50
77.3	-2.53	9.8	4.15
58	-2.32	8.25	6.70
56	-2.16	8.10	7.12
43.3	-1.65	6.70	8.72
35.9	-1.48	6.60	9.36
32.9	-0.95	5.4	12.00

For the low temperature range $\Delta\chi$ was measured by means of the anisotropy torsion balance. Tables 9 and 10 give the magnetic anisotropy (per gram sample) of the most dilute sample. In the first series of measurements the magnetic field was varied to produce a null effect. A plot of $\Delta\chi$ versus T for the temperature range 12-35°K is plotted in Figure 9. The magnetic anisotropy for the range 4-20°K was also measured using the constant field method and is compiled in Table 10 with the data plotted in Figure 10.

Theory

The detailed theoretical calculations for $V^{3+}:Al_2O_3$ were performed by Quade.[20,21] The energy level diagram for V^{3+} in a trigonal field is shown in Figure 7. The $^3T_1(^3F)$ level was found to be lowest and this level is split by V_t into $^3A_2$ and ^3E levels with $^3A_2$ being lowest. The $^3A_2$ level is then split in second order by $\vec{L}\cdot\vec{S}$ into A_1 and E levels with A_1 being lowest. Quade's procedure was to take the (30 X 30) matrix of the ^3F and ^3P levels and to first apply a transformation

$$\begin{matrix} {}^3F \\ {}^3P \end{matrix} \begin{pmatrix} a_1 & a_2 \\ -a_2 & a_1 \end{pmatrix}, \quad a_1 = 0.959, \; a_2 = 0.285 \qquad \text{(V-2)}$$

to eliminate the matrix elements of V_c between the ^3F and ^3P levels. Values of $\Delta_p = 9.00 \times 10^3$ and $\beta = 1.27 \times 10^3$ cm^{-1} were used in the matrix. The first order trigonal splittings for the $^3T_1$ states were found to be

TABLE 9

MAGNETIC ANISOTROPY (PER GRAM SAMPLE) OF V^{3+}-DOPED CORUNDUM

Sample B. Concentration (0.092%)			
T°K	$\Delta\chi \times 10^6$	T°K	$\Delta\chi \times 10^6$
4.2	1.300	16.4	.105
4.3	1.247	16.9	.083
8.1	.523	17.4	.077
8.5	.431	22.2	.037
8.65	.395	23.4	.028
9.2	.362	24.5	.021
10.5	.248	25.3	.018
11.1	.233	26.3	.016
13.3	.161	27.1	.012
13.9	.137	29.4	.008
14.7	.120	35.0	-.001

TABLE 10

MAGNETIC ANISOTROPY (PER GRAM SAMPLE) OF V^{3+}-DOPED CORUNDUM

Sample B. Concentration (0.092%)			
T°K	$\Delta\chi \times 10^6$	T°K	$\Delta\chi \times 10^6$
4.2	1.330	7.6	.533
4.5	1.165	8.1	.457
4.7	1.091	8.9	.405
4.9	1.058	9.2	.342
4.95	1.030	9.7	.304
5.2	.990	10.5	.257
5.3	.943	11.0	.250
5.45	.924	11.2	.209
5.6	.861	13.5	.148
5.8	.840	14.1	.143
5.95	.790	14.5	.112
6.5	.715	16.2	.095
7.05	.615	17.6	.074

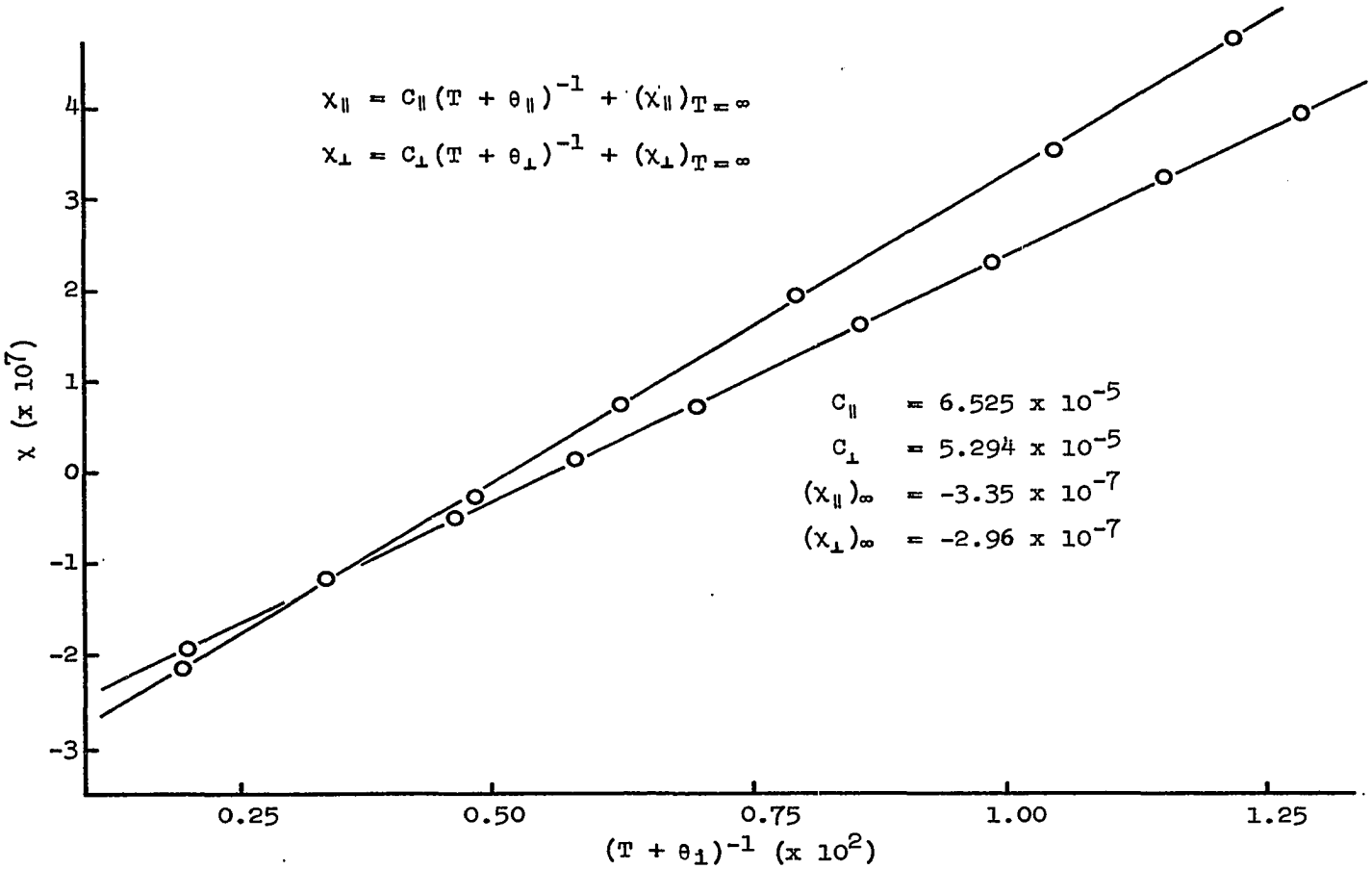

Figure 8. Magnetic Susceptibilities (Per Gm Sample) of the (0.73%) V^{3+}-Doped Corundum Crystal

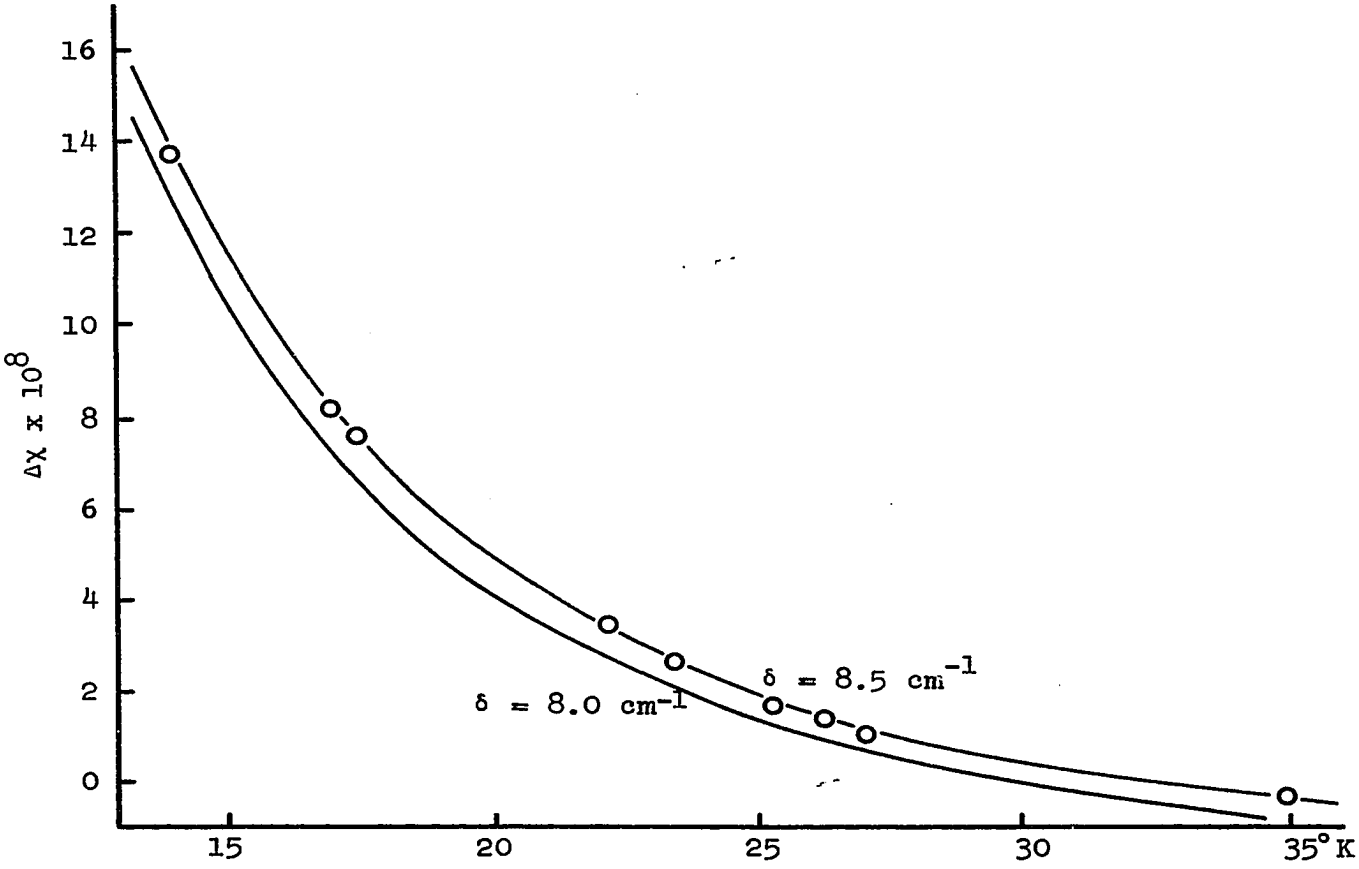

Figure 9. Magnetic Anisotropy (Per Gm Sample) of the (0.092%) V^{3+}-Doped Corundum Crystal from 12-35° K

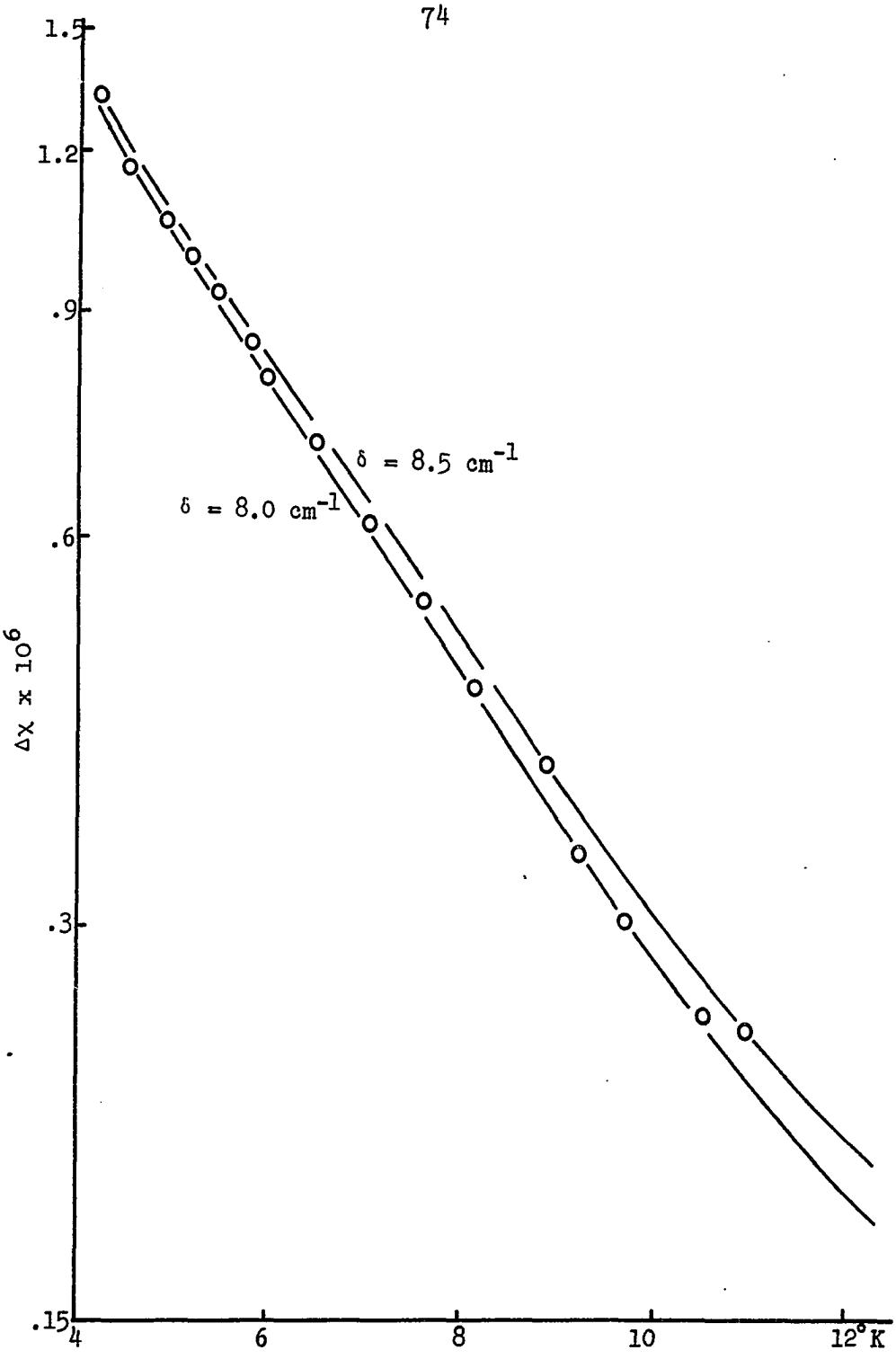

Figure 10. Magnetic Anisotropy (Per Gm Sample) of the (0.092%) V^{3+}-Doped Corundum Crystal from 4-12°K

$$
\begin{aligned}
&^3F: \quad \Delta_t = 8.3D_4 - 4.3D_2, \\
&^3P: \quad \Delta_t = 1.7D_4 - 5.8D_2.
\end{aligned}
\tag{V-3}
$$

Then a fourth order Van Vleck transformation[43] was applied to remove the matrix elements of V_t, $\lambda\vec{L}\cdot\vec{S}$ and $-\vec{\mu}\cdot\vec{H}$ connecting the $^3A_2$ ground state with the upper states. The following results were obtained[21]

$$
\begin{aligned}
g_\perp &= g - 2\alpha^2\lambda/\Delta_T - \alpha'^2\lambda/\Delta_c + \alpha^2(\alpha - 1)\lambda^2/\Delta_T^2 - \alpha\alpha'^2\lambda^2/\Delta_c\Delta_T \\
&\quad + 2\alpha^3(\alpha + 1)\lambda^3/\Delta_T^3 ,
\end{aligned}
\tag{V-4}
$$

$$
g_\parallel = g - (2 + \alpha)\alpha^2\lambda^2/\Delta_T^2 - 4\alpha'^2\lambda/\Delta_c - \alpha\alpha'^2\lambda^2/\Delta_c\Delta_T .
$$

The expressions for the susceptibility were found to be

$$
\begin{aligned}
\chi_\parallel &= 2NB\,\mu_o^2(g_\parallel^2/kT)\exp(-\delta/kT + 2NB\,\mu_o^2\{[2\alpha'^2/\Delta_c \\
&\quad + 2(\alpha+2)^2\alpha^2\lambda^2/\Delta_T^3] + 2[2\alpha'^2/\Delta_c + (\alpha+2)^2\alpha^2\lambda^2/\Delta_T^3]\exp(-\delta/kT)\},
\end{aligned}
\tag{V-5}
$$

$$
\begin{aligned}
\chi_\perp &= 2NB\,\mu_o^2(g_\perp^2/\delta)[1 - \exp(-\delta/kT)] + 2NB\,\mu_o^2[\alpha'^2/\Delta_c \\
&\quad + \alpha^2(1 - 10\alpha^2\lambda^2/\Delta_T^2)/\Delta_T] + 4NB\,\mu_o^2\exp(-\delta/kT)\{\alpha'^2/\Delta_c \\
&\quad + \alpha^2[1 - (3\alpha^2 + 2\alpha - 4)\lambda^2/\Delta_T^2]\Delta_T^{-1}\},
\end{aligned}
$$

where

$$
B = [1 + 2\exp(-\delta/kT)]^{-1} .
$$

Δ_c denotes the energy spacing between the ground state and

$^3T_2(^3F)$ and

$$\alpha = (3/2)a_1^2 - a_2^2 = 1.29,$$

$$\alpha' = (5/2)^{\frac{1}{2}}a_1^2 = 1.52, \qquad \text{(V-6)}$$

$$\alpha'' = a_1^2 - (3/2)a_2^2 = 0.80 .$$

An expansion of the susceptibility equations in powers of δ/kT resulted in

$$\chi_{\parallel} = \frac{2}{3} N \mu_o^2 \{g_{\parallel}^2[k(T + \delta/3k)]^{-1} + \frac{6\alpha'^2}{\Delta_c} + 4(\alpha + 2)^2\alpha^2\lambda^2/\Delta_T^3\}$$

and (V-7)

$$\chi_{\perp} = \frac{2}{3} N \mu_o^2 \{g_{\perp}^2[k(T - \delta/6k)]^{-1} + 3\alpha'^2/\Delta_c$$

$$+ 3\alpha^2[1 - 4(4\alpha^2 + \alpha - 2)\lambda^2/3\Delta_T^2]/\Delta_T\}$$

which are valid in the temperature range 77-500°K.

Analysis of Data

High Temperature Susceptibility

From an inspection of Equations (V-7) it is clear that the susceptibilities should have a Curie-Weiss behavior, that is

$$\chi = C(T + \theta)^{-1} + N\bar{\alpha}$$

Therefore,

$$C_{\parallel}/C_{\perp} = (g_{\parallel}/g_{\perp})^2$$

and since the ratio of $C_{\parallel}/C_{\perp}$ is found from Figure 8 to be

1.235, then

$$g_{\parallel}/g_{\perp} = 1.111 \pm 0.003 \ .$$

Assuming $g_{\parallel} = 1.915$, which is consistent with the value obtained from ESR measurements, $g_{\perp}$ is found to be

$$g_{\perp} = 1.725 \ .$$

The concentration can also be calculated using

$$N = (3kC_{\parallel})/(2 \mu_o^2 g_{\parallel}^2)$$

which gives (0.092%) and (0.73%) for the dilute and the concentrated samples, respectively.

The difference in the extrapolated intercept of $\chi_{\parallel}$ and $\chi_{\perp}$ at $T = \infty$ can be used to estimate Δ_T where

$$(\Delta\chi)_{T=\infty} = 3.9 \times 10^{-8}$$

from Figure 8 for the concentrated sample. If $\delta = 8$ cm^{-1} and $(\lambda/\Delta_T) = 0.08$ are considered to be reasonable estimates, then

$$\Delta_T = 1200 \pm 200 \text{ cm}^{-1} \ .$$

The diamagnetic corrections due to the Al_2O_3 and the V^{3+} ions are eliminated when $\Delta\chi$ is calculated. For temperatures above 300°K no deviation was discernable from the Curie-Weiss behavior and this can be interpreted as evidence for a large Δ_T since a low Δ_T would be expected to produce considerable deviation.

Low Temperature Susceptibility

The magnetic anisotropy $\Delta\chi$ can be written according to Equations (V-5) as

$$\Delta\chi = A[1 - (1 + R/x)\ \exp(-x^{-1})][1 + 2\ \exp(-x^{-1})] + (\Delta\chi)_{VV} \qquad (V\text{-}8)$$

where

$$A = 2N\ \mu_o^2\ g_\perp^2/\delta\ ,$$

$$x = kT/\delta\ ,$$

$$R = (g_\parallel/g_\perp)^2\ ,$$

and $(\Delta\chi)_{VV}$ is the difference in the Van Vleck terms.

Quade[21] found that for $0.3 < x < 0.7$ corresponding to temperatures between 4 and 9°K that a plot of $\ln(\Delta\chi)$ versus T was a straight line within about 3% and that in this range of (x) that

$$\frac{d}{dT}\ln(\Delta\chi) = (k/\delta\ \Delta\chi)\ \frac{d(\Delta\chi)}{dx}$$

where

$$\frac{d(\Delta\chi)}{dx}/\Delta\chi = 3.03,$$

and is independent of δ. Hence the slope is

$$\frac{d[\ln(\Delta\chi)]}{dT} = 3.03(k/\delta)\ .$$

In Figure 10 the $\ln(\Delta\chi)$ has been plotted versus T for

$\delta = 8$ and $8.5\ cm^{-1}$ along with the experimental points. A least squares analysis gives

$$\delta = 8.3 \pm 0.2\ cm^{-1} .$$

In Figure 9 the theoretical curves of $\Delta\chi$ versus T for $\delta = 8$ and $8.5\ cm^{-1}$ have also been plotted along with the experimental data and $\delta = 8.5\ cm^{-1}$ seems to give the best fit in this range. However, there is some uncertainty in $(\Delta\chi)_{VV}$ in this range and as the temperature measurements for $T < 12°K$ are not as accurate as for $T > 12°K$ the value of δ will be taken as $8.4\ cm^{-1}$ with a range of 8.2 to $8.5\ cm^{-1}$.

Crystal Field Parameters

From Equations (V-4) Quade found that

$$g_{\parallel}/g_{\perp} = 1 + \epsilon\alpha^2 + \epsilon^2[\alpha^4 - \alpha^3 - \tfrac{1}{2}\alpha^2] + \epsilon^3[\alpha^6 - (3/2)\alpha^5 - \alpha^4 + \alpha^3] + (\alpha'^2\lambda/2\Delta_c)[-3 + \epsilon(2\alpha - 4\alpha^2)]$$

and (V-9)

$$\delta = \lambda[\alpha^2\epsilon - 2\alpha^3\epsilon^2 - \alpha^4\epsilon^3] - (3/2)\alpha'^2\lambda^2/\Delta_c$$

where

$$\epsilon = \lambda/\Delta_T .$$

From Figure 11, which shows λ as a function of ϵ for several values of $g_{\parallel}/g_{\perp}$ and δ, it is possible to estimate

$$\lambda \cong 95\ cm^{-1}$$

$$\Delta_T \cong 1100\ cm^{-1}$$

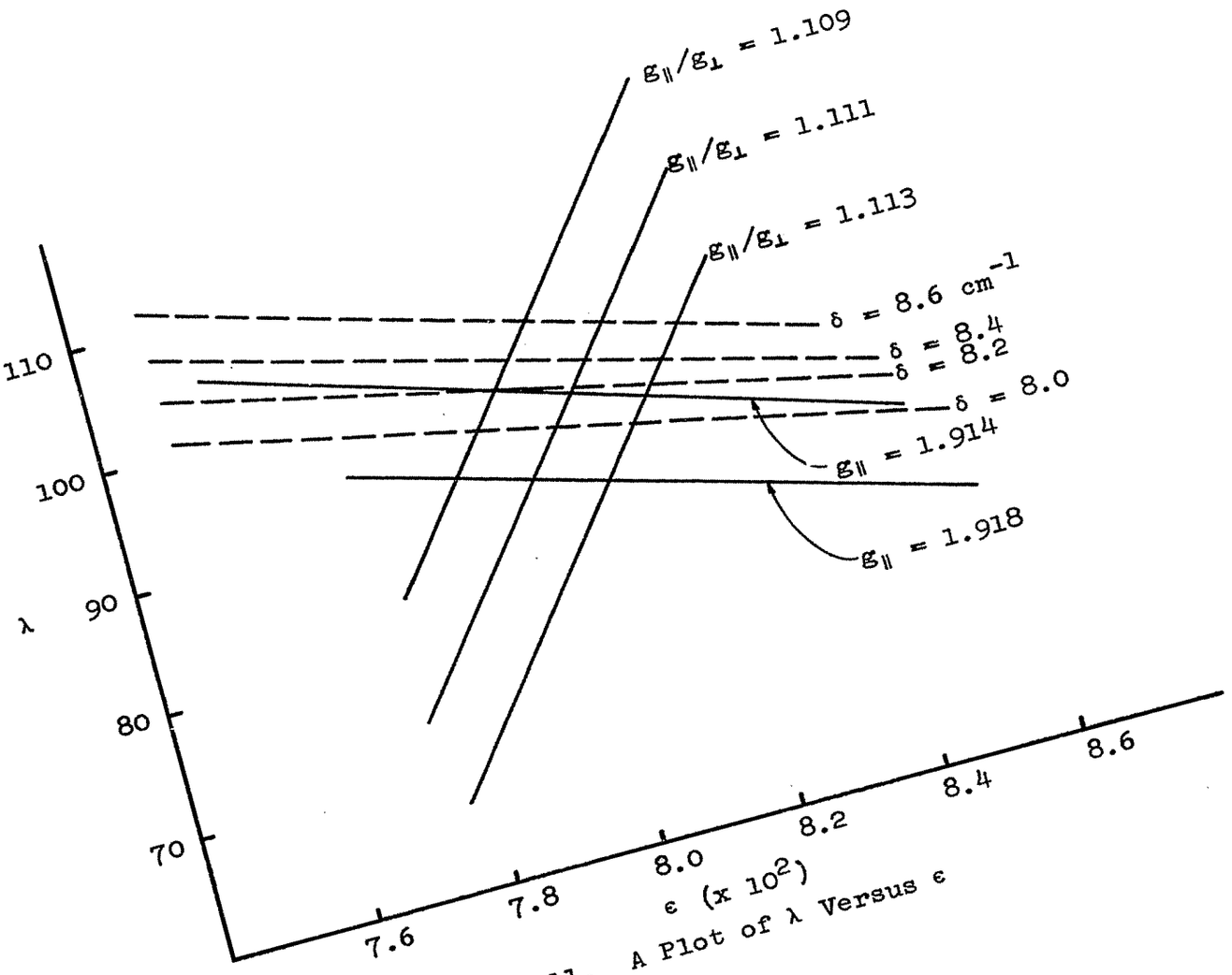

Figure 11. A Plot of λ Versus ϵ

If the trigonal splitting of the $^3T_1(^3P)$ state found in the optical spectrum is combined with this value of Δ_T it is possible to determine the two trigonal field parameters as

$$D_4 = 115.5 \text{ cm}^{-1}$$

and

$$D_2 = 32.7 \text{ cm}^{-1} .$$

Discussion

As in the case for Ni^{2+}, it is also found that the spin orbit coupling constant λ (95 cm^{-1}) is reduced from its free ion value of λ_o (104 cm^{-1}). This indicates that there is some covalent bonding between the central ion and the surrounding anions. The normalization constant squared is given by

$$N^2 = (\lambda/\lambda_o) = 0.91$$

while

$$(B/B_o) = 0.75 .$$

The value of N^2 is larger in this case than for Ni^{2+} which indicates that the bonding of V^{3+} in Al_2O_3 is more ionic than for Ni^{2+} in the semiconductors, ZnO and CdS. The corundum crystal is more ionic than either ZnO or CdS with Al_2O_3 (11.3 ev) having a much larger energy gap between the valence band and the conduction band than ZnO (3.3 ev) or CdS (2.5 ev).

In this case we see that B is reduced by a factor which is nearly N^4 as the simple MO theory indicates (Chapter 4). The experimental results are in qualitative agreement

with the idea that λ_o should be reduced by N^2 and B_o by N^4.

The point charge model has been used to calculate D_4 and D_2.[21] It was found necessary to displace the cation along the trigonal axis by less than 0.1 Å in order to obtain the experimental value of D_4 where $\langle r^4 \rangle$ is calculated from the experimental value of Dq and then this value used to calculate D_4. The calculation of D_2 suffers from the same deficiencies as in the case of Ni^{2+}. A displacement of the cation was not sufficient to account for the experimental value of D_2. For $V^{3+}:Al_2O_3$ the point charge model can presumably account for D_4 but not for D_2.

CHAPTER VI

Co^{2+} IN ZnO

Some recent work on the ESR[44] and optical absorption spectra[18,45] of Co^{2+} has provided some information on the energy levels and the crystalline field present when Co^{2+} ions are introduced into the ZnO lattice. As noted in Chapter IV, ZnO has a wurtzite structure with each atom having about it a tetrahedron of atoms of the opposite sort. Cobalt in octahedral sites[1] has been studied extensively and the ^4F level is found to be lowest as expected from Hund's rule. With V_c considered next it is found that $^4T_1$ lies lowest and $^4A_2$ highest. It is expected that in tetrahedral symmetry that the $^4A_2$ level will be lowest and this is found to be the case.[18] The $^4A_2$ level will not split in first order due to $\vec{L}\cdot\vec{S}$ but will in second order. The zero field splitting of Co^{2+}:ZnO has been reported as 5.5 ± 0.3 cm^{-1} by Estle and DeWit[44] from intensity measurements. The energy level diagram for Co^{2+} in a tetrahedral field is shown in Figure 12.

Experiment

The Co^{2+}:ZnO crystals were furnished by Dr. T. L. Estle of Texas Instruments, Inc. The concentration of the

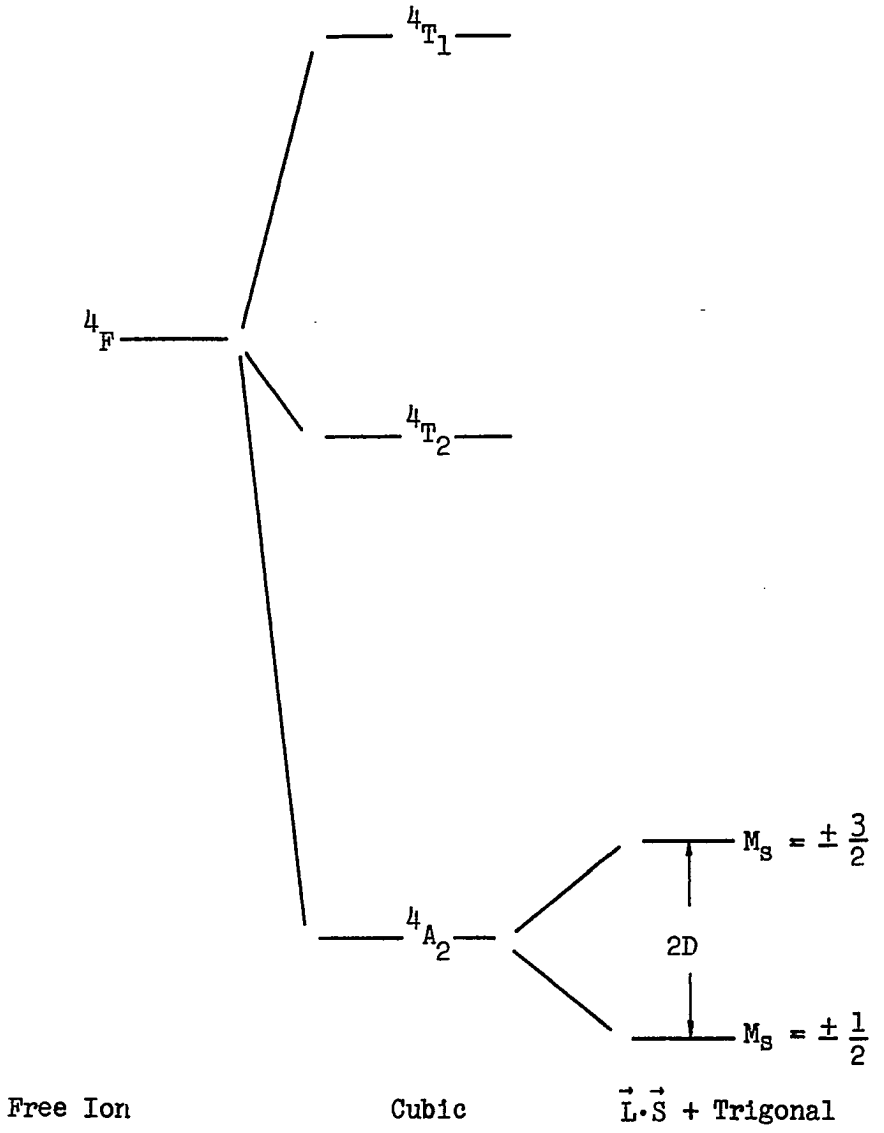

Figure 12. Energy Level Diagram of Co^{2+} in a Tetrahedral Field

Co^{2+} in the ZnO crystal is 0.037% as determined by the analysis of the magnetic data. The magnetic susceptibilities along the trigonal axis and perpendicular to it have been measured over the temperature ranges 9-300°K and 5.7-300°K, respectively. Table 11 gives the results obtained for $\chi_{\parallel}$ and $\chi_{\perp}$. As in the case of the $V^{3+}:Al_2O_3$, $\chi_{\parallel}$ could not be

TABLE 11

MAGNETIC SUSCEPTIBILITIES (PER GM SAMPLE) OF THE Co^{2+}-DOPED ZnO

T (°K)	$\chi_{\perp} \times 10^7$ (cgs-emu)	T (°K)	$\chi_{\parallel} \times 10^7$ (cgs-emu)
5.7	30.9	9.1	12.1
8.8	19.0	12.5	9.5
9.8	16.8	15.2	8.1
12.6	12.2	17.0	7.3
14.0	11.4	19.0	6.7
16.6	8.8	20.8	6.2
21.2	7.1	77.3	1.8
24.8	6.4	295.0	0.5
26.5	5.6		
77.3	2.0		
295.0	0.5		

measured below about 9°K because of the torque acting on the

sample which caused the crystal to rotate out of alignment. The magnetic anisotropy was measured on the torsion balance over the temperature range of 4.2 to 17°K. Above this range ($\Delta\chi$) is so small that no significant results could be obtained. Table 12 gives the results obtained for ($\Delta\chi$).

TABLE 12

MAGNETIC ANISOTROPY (PER GM-SAMPLE)
OF THE Co^{2+}-DOPED ZnO

T (°K)	$\Delta\chi \times 10^7$ (cgs-emu)	T (°K)	$\Delta\chi \times 10^7$ (cgs-emu)
4.2	24.2	7.3	9.3
4.6	20.5	7.7	8.9
4.8	19.9	7.9	8.1
4.9	18.4	8.8	6.4
5.2	16.9	10.0	5.0
5.5	15.3	13.0	3.4
5.8	13.7	18.0	1.9
6.2	12.4	23.0	1.3
6.8	10.8		

Theory

The theoretical work for the cobalt in zinc oxide crystal has been performed by Sanmann.[46] The crystal field theory is used as a suitable model where the crystalline field

is primarily cubic with a small trigonal component as for the other crystals. The Hamiltonian is also the same as Equation (IV-2). The ground state configuration for Co^{2+} is $(3d)^7$ with multiplets ^4F, ^4P, ^2G, ^2H, ^2P, ^2D, and ^2F in order of increasing energy. For the quartet states the cubic field (V_c) splits the levels into

$$^4F \rightarrow {}^4T_1 + {}^4T_2 + {}^4A_2$$
$$^4P \rightarrow {}^4T_1 \quad .$$

Neither $\lambda\vec{L}\cdot\vec{S}$ nor V_t splits the ground state ($^4A_2$) in first order but will in second, as shown in Figure 12.

Sanmann's procedure was to set up the (28 X 28) energy matrix in the cubic representation and apply a fourth order Van Vleck transformation to reduce the matrix elements between the ground state and the upper levels. The results obtained by Sanmann[46] for the magnetic susceptibilities are

$$\chi_{\parallel} = (N \mu_o^2 g_{\parallel}^2/4kT)(B)[1 + 9 \exp(-2D/kT)]$$

and

$$\chi_{\perp} = (N \mu_o^2 g_{\perp}^2)(B)[(1/kT) + (3/2D)\{1 - \exp(-2D/kT)\}]$$

if (VI-1)

$$(A_2 \tfrac{1}{2}|\mu_z|A_2 \tfrac{1}{2}) = (A_2 \tfrac{3}{2}|\mu_z|A_2 \tfrac{3}{2})/3$$

and

$$(A_2 \tfrac{1}{2}|\mu_x|A_2 \tfrac{3}{2}) = (A_2 \tfrac{1}{2}|\mu_x|A_2 -\tfrac{1}{2})(6)^{\frac{1}{2}}/2 \ .$$

Also

$$2D = 8\lambda^2/(15\beta)^2[19(5)^{\frac{1}{2}}D_2/6 + 5D_4/9] ,$$

$$g_{\parallel} = 2 - (8\lambda/15\beta) - 10(\lambda/15\beta)^2 + [152(5)^{\frac{1}{2}}D_2/9 - 760D_4/27](\lambda)(15\beta)^{-2} \qquad \text{(VI-2)}$$

and

$$g_{\perp} = 2 - (8\lambda/15\beta) - 10(\lambda/15\beta)^2 + [-76(5)^{\frac{1}{2}}D_2/9 - 880D_4/27](\lambda)/(15\beta)^{2}$$

where

$$\beta = 2\ Dq/3$$

which can be obtained from the optical spectra ($Dq = 390\ cm^{-1}$).[18]

Analysis of Data

Using Estle and DeWit's values[44] for $g_{\parallel}$ (2.2404) and $g_{\perp}$ (2.2790) to substitute into the susceptibility equations one can plot χ versus T for particular values of the zero field splitting (2D). The magnetic data can be fitted best with a value of 4 cm^{-1}. The theoretical curve using this value has been plotted in Figure 13 along with the experimental data. The experimental data have been corrected for the diamagnetism of the host crystal ($\chi_{ZnO} = 0.330 \times 10^{-6}$ per gram). Upon considering the experimental errors involved, the value for 2D is taken as $2D = 4 \pm 0.3\ cm^{-1}$ for this particular crystal (Texas Instruments - A-99).

The magnet anisotropy ($\Delta\chi$) for this crystal has been measured on the torsion balance and is plotted in Figure 14

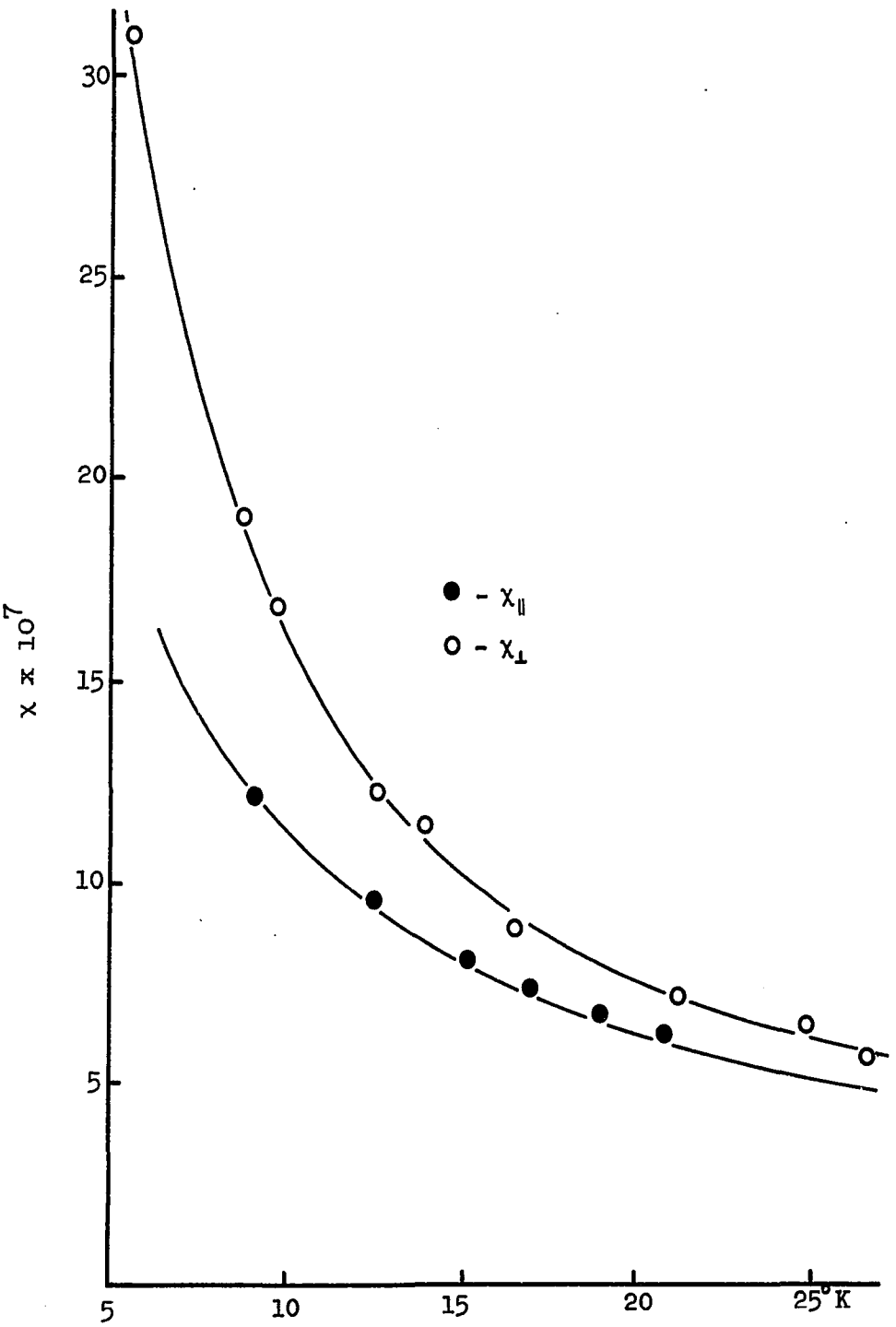

Figure 13. Magnetic Susceptibilities (Per Gm-Sample) of Co^{2+}:ZnO

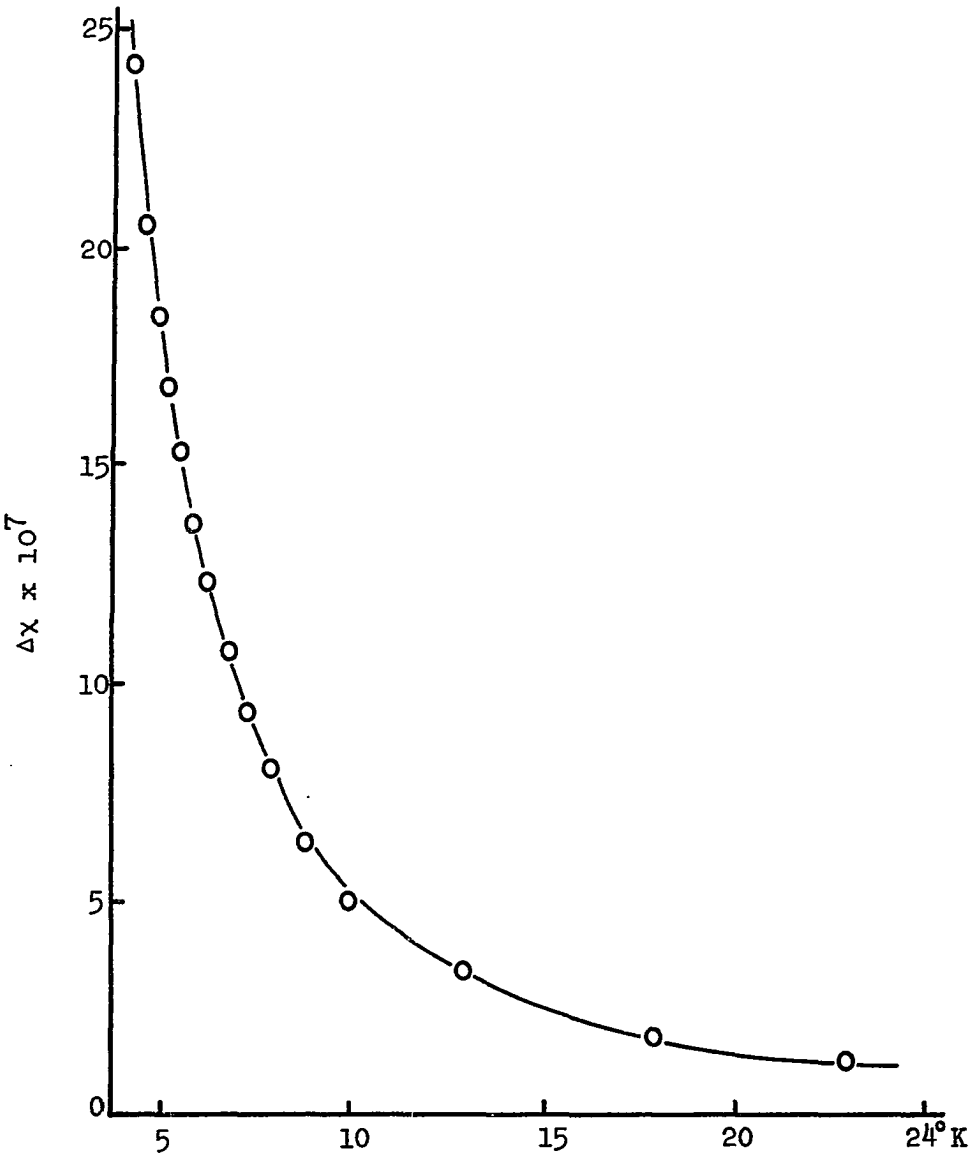

Figure 14. Magnetic Anisotropy (Per Gm-Sample) of Co^{2+}:ZnO

along with the theoretical values of $2D = 4\ cm^{-1}$. In this case the measurements are not too sensitive to changes in 2D and from the $\Delta\chi$ measurements it can only be concluded that $2D = 4 \pm 1\ cm^{-1}$. A value of $2D = 4 \pm 0.3\ cm^{-1}$ will be taken as the most probable value of the zero field splitting of this crystal. With this value of 2D, the experimental ESR value of Δg, and the relation obtained from Equations (VI-2) that $2D = -\lambda(\Delta g)$, λ was found to be $-104\ cm^{-1}$. D_4 and D_2 calculated from the above equations are $286\ cm^{-1}$ and $77\ cm^{-1}$, respectively.

Discussion

The value of 2D ($4\ cm^{-1}$) obtained from the magnetic data disagrees somewhat with the ESR value of $5.5\ cm^{-1}$ obtained by Estle and DeWit. The magnetic data is subject to certain errors which would tend to give a slightly lower value of 2D. The orientation of the crystal was determined by the X-ray lab at Texas Instruments and it is assumed that this is not in error ($\pm$ 1 degree). This was also checked by Dr. Dick Van der Helm at the University of Oklahoma. The alignment of the crystal in the magnetic field could be off by at most 5 degrees (more probably 1 degree) and, as the apparent values of the susceptibilities are given by

$$\chi_{\parallel}^{A} = (\mathrm{Cos}^2\,\theta)\chi_{\parallel} + (\mathrm{Sin}^2\,\theta)\chi_{\perp}$$

and (VI-3)

$$\chi_{\perp}^{A} = (\mathrm{Sin}^2\,\theta)\chi_{\perp} + (\mathrm{Cos}^2\,\theta)\chi_{\parallel}$$

where θ is the angle between the magnetic field and the trigonal axis of the crystal, the alignment would have to be off by as much as 20° which is clearly outside the experimental error.

In doping the crystals it is possible that there might be pairs or clusters of higher order which are coupled together by the exchange effect.[48] However, this should be quite small if the crystal is more or less doped throughout but if the doping is primarily on the outer layer of the crystal this would increase the number of coupled systems. While the pairs would tend to cancel out (antiferromagnetic coupling) at low temperatures, the triplets might make some contribution and since this effect is primarily isotropic the effect would be to decrease 2D.

In calculating the magnetic susceptibility it was assumed that

$$3(^4A_2\ \tfrac{1}{2}|\mu_z|\ ^4A_2\ \tfrac{1}{2}) = (^4A_2\ \tfrac{3}{2}|\mu_z|\ ^4A_2\ \tfrac{3}{2}) \ .$$

If the ratio of these matrix elements is changed from 3 to 3.16, and the susceptibility recalculated, the magnetic data can be fitted with $2D = 5.2\ cm^{-1}$. This would bring the experimental value of 2D as determined from the magnetic data within the experimental error of the ESR value. A value of u in Equation (VI-6) of 0.033 would give the ratio as 3.16 and while this is a rather large value it was found for Co^{2+}

in cubic ZnS that u = -0.005.

According to Estle (private communication)[44] the ESR data were analyzed using the spin Hamiltonian of the form

$$H = g_{\parallel}\mu_o H_z S_z + g_{\perp}\mu_o(H_x S_x + H_y S_y) + D[S_z^2 - (1/3)S(S+1)] + AS_z I_z + B(S_x I_x + S_y I_y) \quad \text{(VI-4)}$$

A correction term of the form

$$\frac{3g_{\perp}^2 \sin^2\theta\,(g_{\parallel}^2\cos^2\theta - 2g_{\perp}^2\sin^2\theta)}{8(g_{\parallel}^2\cos^2\theta + 4g_{\perp}^2\sin^2\theta)^{\frac{1}{2}}}\,\frac{\mu_o^3 H^3 M_S}{D^2} \quad \text{(VI-5)}$$

appears in the expression for the energy of the $M_S = \pm\frac{1}{2}$ levels and was used by Estle and DeWit in their calculations. The value of $g_{\perp}$ obtained at 9149 Mc/s was 2.2790 and at 23,796 Mc/s, $g_{\perp} = 2.2789$ using $2D = 5.5\ cm^{-1}$. A value of 2D was obtained using the temperature dependence of the intensity of the cobalt resonance at 1.3°K and 4.2°K. According to Estle this value was in agreement with the value obtained using the correction term.

Estle also pointed out that a term

$$u\mu_o[S_x^3 H_x + S_y^3 H_y + S_z^3 H_z - (1/5)(\vec{S}\cdot\vec{H})[3S(S+1) - 1]] \quad \text{(VI-6)}$$

had been ignored and that the actual g-values might be different from those given.[47] Also Co^{2+}:CdS could not be

analyzed using the same correction term and high accuracy cannot be claimed for the intensity measurement. Therefore, the value of 5.5 cm^{-1} for the zero field splitting could be somewhat in error.

Sanmann has recently made some calculations on the $^4T_1(^4F)$ band which indicate that 2D is close to 5 cm^{-1}. The reason for the discrepancy between the ESR and the magnetic data is not clear at the present time.

The values of λ, D_4, and D_2 which were calculated using the ESR and the magnetic data are

	ESR DATA	MAGNETIC DATA
λ	-143 cm^{-1}	-104 cm^{-1}
D_4	-44 cm^{-1}	286 cm^{-1}
D_2	76 cm^{-1}	77 cm^{-1}

The experimentally determined value of λ (-104 cm^{-1}) is decreased from its free ion value of λ_o (-178 cm^{-1}) which is quite at variance with the apparent increase of λ (-210 cm^{-1}) as determined by the optical spectrum.[18] It should be pointed out, however, that in the analysis of the optical data the effect of the trigonal field was not considered and it may be that λ was overestimated since the entire splitting of the $^4T_1(^4F)$ band was taken as being due to the spin-orbit splitting. Calculations by Sanmann[46] on this level indicate that λ is actually reduced if V_t is considered.

The ratio (λ/λ_o) is found to be 0.59 which is in

reasonably good agreement with the value obtained for Ni^{2+}:ZnO (0.52). If the ESR value of λ is used then (λ/λ_o) = 0.80 which is about the value obtained for Co^{2+} in the very ionic host crystal, MgO.[45] The ratio of (B/B_o) is 0.78 and since the experimentally determined values of (λ/λ_o) are expected to be less than (B/B_o) one might expect a lower value of λ than -140 cm^{-1}.

Using the point charge model, D_4 for ZnO crystals was calculated in Chapter IV where, for the undistorted crystals and no displacement of the Co^{2+} ion, D_4 is found to be -40 cm^{-1} if all ions out to 20 Å are considered and where the differences in Dq for the two cations are taken into consideration. If one accepts the ESR value of 2D then D_4 agrees with experiment with practically no change in the lattice parameters. This seems to be what one would expect upon examining the ionic radii of Co^{2+} (0.72 Å) and Zn^{2+} (0.74 Å). Since the ionic radii of Ni^{2+} (0.70 Å) is smaller than that of Co^{2+} one would expect the contraction of the lattice to be less in the case of Co^{2+} if the model of Kakuchi and Azarbavejani is correct.[30] In the case of D_4 (286 cm^{-1}) calculated from the magnetic data the three equivalent anions would have to collapse toward the cation by about 0.2 Å more than the unique anion. While the calculation of D_2 has not proven very successful it is of interest to note that in the case where there is very little contraction, $D_2 \sim 0$, while D_2 = 200 cm^{-1} for a 0.2 Å contraction. This is to be compared

with the experimental value of 76 cm^{-1}.

It would be desirable to measure $\chi_{\perp}$ and $\chi_{\parallel}$ all the way down to 4.2°K and this should be possible by a new Faraday balance being built by Yarger which is designed so that the sample will not rotate out of position. The data obtained at the lower temperatures for $\chi_{\parallel}$ should be very useful because of the large dependence on 2D in this range.

The quantitative agreement between the three sets of data from the E.S.R., optical, and magnetic measurements lacks something to be desired but by using more refined experimental techniques it may be that the agreement can be improved.

CHAPTER VII

YTTERBIUM GALLIUM GARNET

The energy levels associated with the crystalline field splittings of the rare earth ion in ytterbium gallium garnet have been studied in various laboratories by measurements of magnetic susceptibilities[49-52] and by optical spectroscopy.[53] As a first approximation the crystalline field can be taken as being cubic, and the ground manifold of Yb^{3+} ($^2F_{7/2}$) splits into three components, Γ_7 (ground state), Γ_8, and Γ_6.[51,53] The magnetic measurements made by Ball, Garton, Leak, and Wolf[51] at low temperatures indicate that the spacing, $\Gamma_8 - \Gamma_7$, between the ground and the first excited crystalline Stark level is 570 cm^{-1}. Similar results were also obtained by Ayant, Thomas, Cohen and Ducloz.[52] More recently from the study of the dependence of the intensity of the optical transitions on temperature, Wood[54] has reported two low-lying levels at 112 cm^{-1} and 308 cm^{-1} in addition to the one at 570 cm^{-1}. The main feature of this present work is that it extends to higher temperatures than previous investigations and so yields information on the location of the Γ_6 levels which do not combine magnetically with the ground state, and so do not enter at low temperatures.

Experiment

The susceptibility measurements were made with the Faraday balance and for temperatures above 300°K the furnace built by Segraves, which is similar to that of Garber, Henry, and Howe[59], was utilized. The accuracy of the susceptibility data is estimated to be about 1.5% for this sample. The measurements of temperature are accurate to 0.6% at temperatures below 750°K and to 3% for T greater than 750°K. Table 13 shows the experimental results above 29°K. The susceptibilities given there have been corrected for the diamagnetism of the crystals. The measurements obviously do not extend to low enough temperatures to reveal the anomalies at T ~ 0.2°K which were reported by Ball et al.[51] The diamagnetic contribution was estimated by measuring the magnetic susceptibility of the pure yttrium gallium garnet which gives -85×10^{-6} cgs-emu per gm-ion of the yttrium ion. The diamagnetic susceptibility of Yb^{3+}, however, differs slightly from that of Y^{3+} (by 6×10^{-6} cgs-emu per gm-ion).[55] Thus the diamagnetic correction of YbGaG is taken as -91×10^{-6} cgs-emu per gm-ion of Yb^{3+}. The results are displayed graphically in Figures 15 and 16.

Theory

The electronic configuration of the free ion Yb^{3+} is $(4d)^{10}(4f)^{13}(5s)^2(5p)^2$ which has one electron missing from the 4f shell. For a single hole in a 4f shell only a ^2F level is possible. The Hamiltonian is assumed to be

TABLE 13

MAGNETIC SUSCEPTIBILITIES (CGS-EMU/GM-ION OF Yb^{+++}) OF YbGaG

T (°K)	$\chi \times 10^3$ (cgs-emu)	T (°K)	$\chi \times 10^3$ (cgs-emu)
29.3	41.1	218	8.70
38.6	32.2	252	7.94
44.5	28.1	295	7.11
45.9	27.8	326	6.59
46.3	27.4	384	5.82
47.9	26.2	452	5.12
48.3	26.1	526	4.59
51.2	24.9	568	4.28
53.8	24.1	611	4.10
57.2	23.0	639	3.92
68.7	19.6	658	3.81
69.8	19.3	684	3.67
70.8	19.2	724	3.50
77.3	18.1	776	3.28
89.0	16.4	814	3.15
102.5	14.6	866	2.98
111	13.7	907	2.86
113	13.5	928	2.83
129	12.5	967	2.69
141	11.8	998	2.60

TABLE 13 (continued)

T (°K)	$\chi \times 10^3$ (cgs-emu)	T (°K)	$\chi \times 10^3$ (cgs-emu)
162	10.6	1038	2.50
181	9.92	1069	2.45
197	9.36	1109	2.37

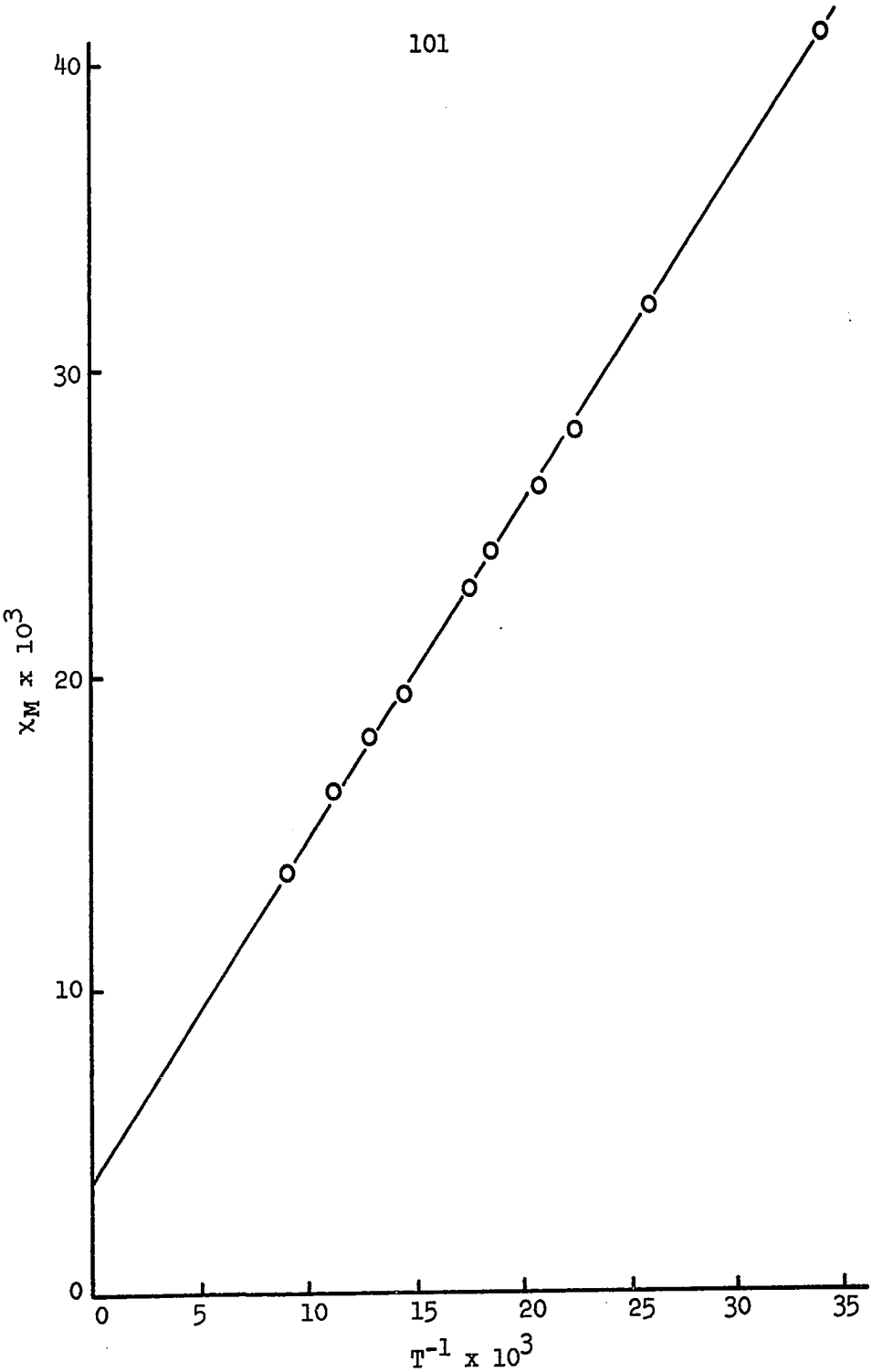

Figure 15. Magnetic Susceptibilities (Per Gm-Ion) of YbGaG from 29-1000°K

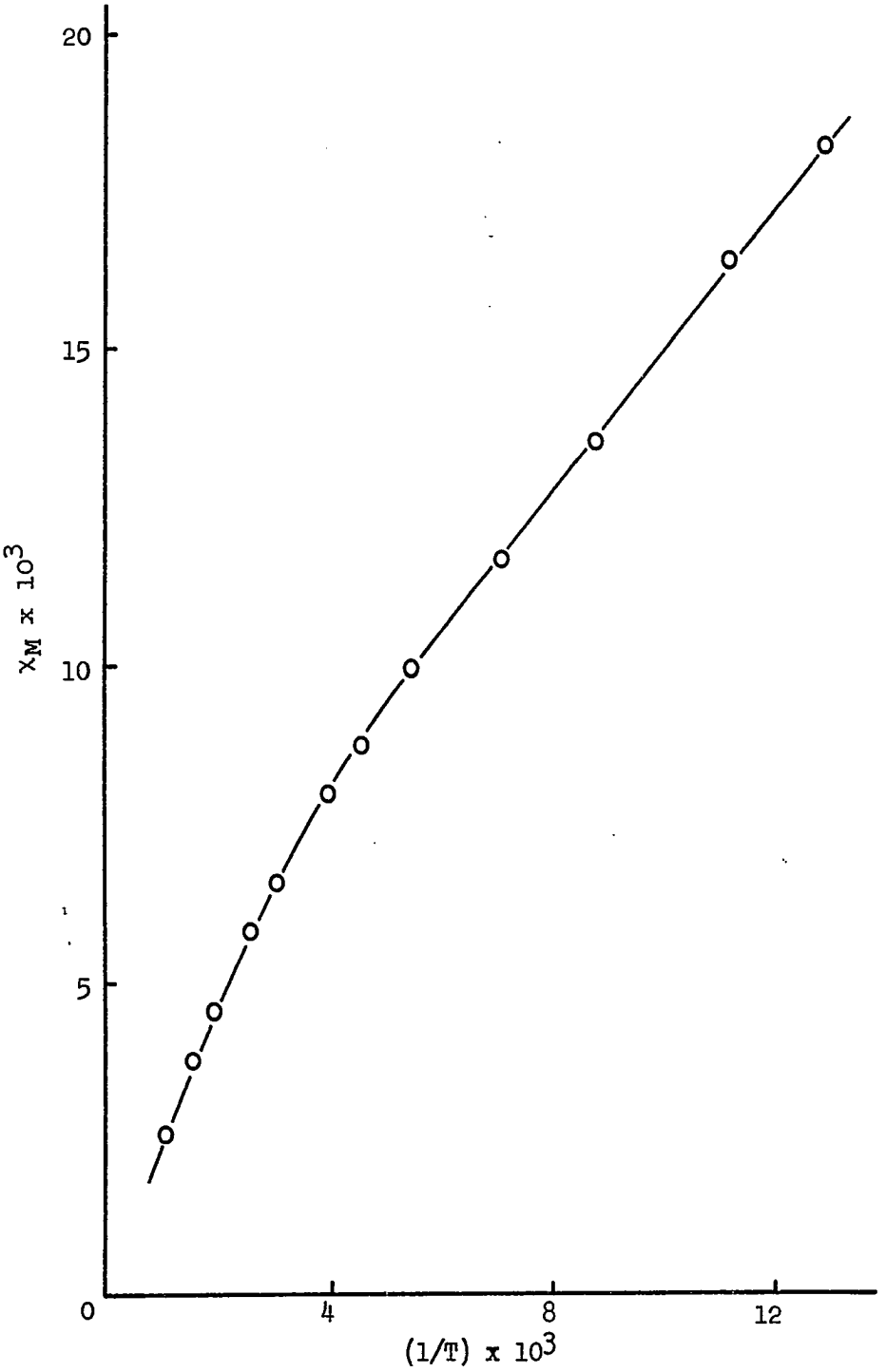

Figure 16. Magnetic Susceptibilities (Per Gm-Ion) of YbGaG from 77-1000°K

$$H = H_o + \lambda \vec{L}\cdot\vec{S} + V_c + \mu_o(\vec{L} + g_s\vec{S})\cdot\vec{H}$$

where, of course, H_o does not contain an electrostatic interaction term. Because of the very large value of the spin-orbit coupling constant (2940 cm^{-1}) the $\lambda\vec{L}\cdot\vec{S}$ splitting will be considered first rather than V_c which was larger for the iron group elements. The energy level scheme for Yb^{3+} in a cubic field is shown in Figure 17. The ^2F level will split under $\lambda\vec{L}\cdot\vec{S}$ into

$$^2F \rightarrow {}^2F_{7/2} + {}^2F_{5/2}$$

and under a cubic field

$$^2F_{7/2} \rightarrow {}^2\Gamma_6 + {}^2\Gamma_7 + {}^4\Gamma_8$$

$$^2F_{5/2} \rightarrow {}^2\Gamma_7 + {}^4\Gamma_8 \ .$$

The wave functions for the $(J\ M_J)$ representation are listed in Table 14 and are obtained using the Clebsch-Gordan coefficients for the one electron orbital and spin wave functions.

The cubic potential[53] will be taken as

$$V_c = V_4^o + (V_4^4 + V_4^{-4}) + V_6^o + (V_6^4 + V_6^{-4}) \ . \qquad \text{(VII-2)}$$

Pappalardo and Wood[53] have worked out the matrix elements of V_c in the $(J\ M_J)$ representation and these are given in Appendix VII for the $^2F_{7/2}$ manifold. Solving the energy matrix of V_c leads immediately to the eigenvalues and the eigenvectors of the matrix and allows one to obtain the cubic wave

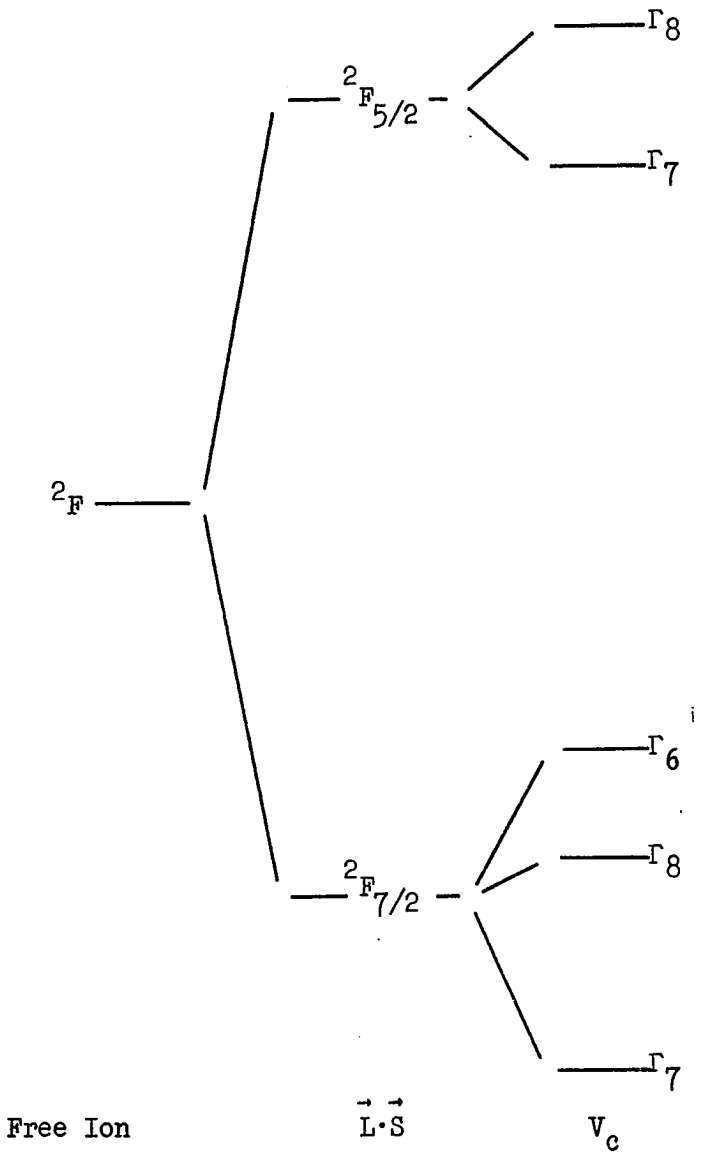

Figure 17. Energy Level Diagram of Yb^{3+} in a Cubic Field

TABLE 14

WAVE FUNCTIONS FOR Yb^{3+} IN THE (J M_J) REPRESENTATION*

$^2F_{7/2}$

$$\Psi_{(7/2,7/2)} = \psi_3{}^{\alpha}$$

$$\Psi_{(7/2,5/2)} = \sqrt{6/7}\ \psi_2{}^{\alpha} + \sqrt{1/7}\ \psi_3{}^{\beta}$$

$$\Psi_{(7/2,3/2)} = \sqrt{5/7}\ \psi_1{}^{\alpha} + \sqrt{2/7}\ \psi_2{}^{\beta}$$

$$\Psi_{(7/2,1/2)} = \sqrt{4/7}\ \psi_0{}^{\alpha} + \sqrt{3/7}\ \psi_1{}^{\beta}$$

$$\Psi_{(7/2,-1/2)} = \sqrt{3/7}\ \psi_{-1}{}^{\alpha} + \sqrt{4/7}\ \psi_0{}^{\beta}$$

$$\Psi_{(7/2,-3/2)} = \sqrt{2/7}\ \psi_{-2}{}^{\alpha} + \sqrt{5/7}\ \psi_{-1}{}^{\beta}$$

$$\Psi_{(7/2,-5/2)} = \sqrt{1/7}\ \psi_{-3}{}^{\alpha} + \sqrt{6/7}\ \psi_{-2}{}^{\beta}$$

$$\Psi_{(7/2,-7/2)} = \psi_{-3}{}^{\beta}$$

$^2F_{5/2}$

$$\Psi_{(5/2,5/2)} = -\sqrt{1/7}\ \psi_2{}^{\alpha} + \sqrt{6/7}\ \psi_3{}^{\beta}$$

$$\Psi_{(5/2,3/2)} = -\sqrt{2/7}\ \psi_1{}^{\alpha} + \sqrt{5/7}\ \psi_2{}^{\beta}$$

$$\Psi_{(5/2,1/2)} = -\sqrt{3/7}\ \psi_0{}^{\alpha} + \sqrt{4/7}\ \psi_1{}^{\beta}$$

$$\Psi_{(5/2,-1/2)} = -\sqrt{4/7}\ \psi_{-1}{}^{\alpha} + \sqrt{3/7}\ \psi_0{}^{\beta}$$

$$\Psi_{(5/2,-3/2)} = -\sqrt{5/7}\ \psi_{-2}{}^{\alpha} + \sqrt{2/7}\ \psi_{-1}{}^{\beta}$$

TABLE 14 (continued)

$\Psi_{(5/2,-5/2)} = -\sqrt{6/7}\,\psi_{-3}\alpha + \sqrt{1/7}\,\psi_{-2}\beta$

*The wave functions are described by J, M_J, M_l, and M_s where $\Psi_{(J,M_J)} = a\psi_{M_l}\alpha + b\psi_{M_l+1}\beta$ and α and β are defined as the spin wave functions described by $M_s = +\frac{1}{2}$ and $M_s = -\frac{1}{2}$, respectively.

functions.[53] These are listed in Table 15. The eigenvalues for the $^2F_{7/2}$ level are

$$\begin{aligned}(\Gamma_7) &= -18P - 72R \\ (\Gamma_8) &= 2P + 96R \\ (\Gamma_6) &= 14P - 120R\end{aligned} \qquad \text{(VII-3)}$$

with

$$P = 3\left(\frac{70}{9}\frac{ze^2\alpha_s}{R^5}\right)\left(\frac{2}{15 \times 77}\right)\langle r^4\rangle$$

and

$$R = 3\left(\frac{70}{9}\frac{ze^2\alpha_s'}{R^7}\right)\left(\frac{4}{13 \times 33 \times 63}\right)\langle r^6\rangle$$

according to Wood.[53] The matrix elements for $|\vec{L} + 2\vec{S}|$ are given in Appendix VIII for the $(J\ M_J)$ representation and in Table 16 for the cubic representation.

The magnetic susceptibility can now be calculated using the standard expression of Van Vleck[3] as

$$\chi = B\left\{\frac{4.0849}{\Delta_8} + \frac{2.164}{T} + \exp(-\Delta_8/kT)\left(\frac{3.5374}{T} + \frac{5.2952}{\Delta_6 - \Delta_8} - \frac{4.0849}{\Delta_8}\right) + \exp(-\Delta_6/kT)\left(\frac{1.3333}{T} - \frac{5.2952}{\Delta_6 - \Delta_8}\right)\right\} \qquad \text{(VII-4)}$$

where

$$B^{-1} = 2 + 4\exp(-\Delta_8/kT) + 2\exp(-\Delta_6/kT)$$

and Δ_8 and Δ_6 stand for the energy differences $\Gamma_8 - \Gamma_7$ and $\Gamma_6 - \Gamma_7$ (in units of cm^{-1}) respectively, and $k = 1/1.44$.

TABLE 15

CUBIC WAVE FUNCTIONS FOR Yb^{3+}

$^2F_{7/2}(\Gamma_7)$

$$\Psi_7^{(1)} = 1/2[\sqrt{3}\,\Psi_{(7/2,5/2)} - \Psi_{(7/2,-3/2)}]$$

$$\Psi_7^{(2)} = 1/2[\sqrt{3}\,\Psi_{(7/2,-5/2)} - \Psi_{(7/2,3/2)}]$$

$^2F_{7/2}(\Gamma_8)$

$$\Psi_8^{(1)} = (7/12)^{\frac{1}{2}}[\Psi_{(7/2,7/2)} - \sqrt{5/7}\,\Psi_{(7/2,-1/2)}]$$

$$\Psi_8^{(2)} = (7/12)^{\frac{1}{2}}[\Psi_{(7/2,-7/2)} - \sqrt{5/7}\,\Psi_{(7/2,1/2)}]$$

$$\Psi_8^{(3)} = 1/2[\Psi_{(7/2,5/2)} + \sqrt{3}\,\Psi_{(7/2,-3/2)}]$$

$$\Psi_8^{(4)} = 1/2[\Psi_{(7/2,-5/2)} + \sqrt{3}\,\Psi_{(7/2,3/2)}]$$

$^2F_{7/2}(\Gamma_6)$

$$\Psi_6^{(1)} = (5/12)^{\frac{1}{2}}[\Psi_{(7/2,7/2)} + \sqrt{7/5}\,\Psi_{(7/2,-1/2)}]$$

$$\Psi_6^{(2)} = (5/12)^{\frac{1}{2}}[\Psi_{(7/2,-7/2)} + \sqrt{7/5}\,\Psi_{(7/2,+1/2)}]$$

TABLE 16

MATRIX ELEMENTS OF $|\vec{L} + 2\vec{S}|$ FOR Yb^{3+} IN THE CUBIC REPRESENTATION

$|L_z + 2S_z|$

$\Psi_7^{(1)}$	$\Psi_8^{(2)}$
12/7	$8\sqrt{3}/7$
	-4/7

$\Psi_7^{(2)}$	$\Psi_8^{(4)}$
-12/7	$-8\sqrt{3}/7$
	4/7

$\Psi_8^{(1)}$	$\Psi_6^{(1)}$
44/21	$8\sqrt{35}/21$
	4/3

$\Psi_8^{(2)}$	$\Psi_6^{(2)}$
-44/21	$-8\sqrt{35}/21$
	-4/3

TABLE 16 (continued)

$|L_x + 2S_x|$

$\Psi_7^{(1)}$	$\Psi_7^{(2)}$	$\Psi_8^{(1)}$	$\Psi_8^{(2)}$	$\Psi_8^{(3)}$	$\Psi_8^{(4)}$	$\Psi_6^{(1)}$	$\Psi_6^{(2)}$
	-12/7	12/7			$4\sqrt{3}/7$		
-12/7			12/7	$4\sqrt{3}/7$			
12/7			20/21	$-8\sqrt{3}/21$			$-4\sqrt{35}/21$
	12/7	20/21			$-8\sqrt{3}/21$	$-4\sqrt{35}/21$	
	$4\sqrt{3}/7$	$-8\sqrt{3}/21$			12/7	$4\sqrt{105}/21$	
$4\sqrt{3}/7$			$-8\sqrt{3}/21$	12/7			$4\sqrt{105}/21$
			$-4\sqrt{35}/21$	$4\sqrt{105}/21$			4/3
		$-4\sqrt{35}/21$			$4\sqrt{105}/21$	4/3	

Analysis of Data

From Figures 15 and 16 it is seen that below 150°K, the magnetic susceptibilities fit very well to the equation

$$\chi = (C/T) + \alpha$$

with $C = 1.083$ and $\alpha = 0.00397$ which is in fairly good agreement with Wolf's results[51] of $C = 1.116$ and $\alpha = 0.00358$ (probably without diamagnetic correction) and the value of $C = 1.096$ calculated from the g-factors of the ESR data.[56] The discrepancies are more than likely caused by differing amounts of chemical purity.

As pointed out by Wolf[51], α is affected only by the Γ_8 levels but not by Γ_6. Using the experimentally determined value of α and making use of Equation (VII-4) for low temperatures

$$\alpha = 4.0849/2\Delta_8 \quad .$$

It is found that $\Gamma_8 - \Gamma_7 = 515$ cm^{-1} if it is assumed that the field is completely cubic.

The magnetic data at high temperature may be used to determine the position of the Γ_6 level. However, calculations show that χ is not very sensitive to $\Gamma_6 - \Gamma_7$; a satisfactory fit to the experimental data can be achieved by taking $\Gamma_6 - \Gamma_7 =$ anywhere between 700 and 900 cm^{-1}. The calculated susceptibilities obtained by using $\Gamma_6 - \Gamma_7 = 800$ cm^{-1} are shown in Figures 15 and 16 (solid curve) while Figure 18 shows

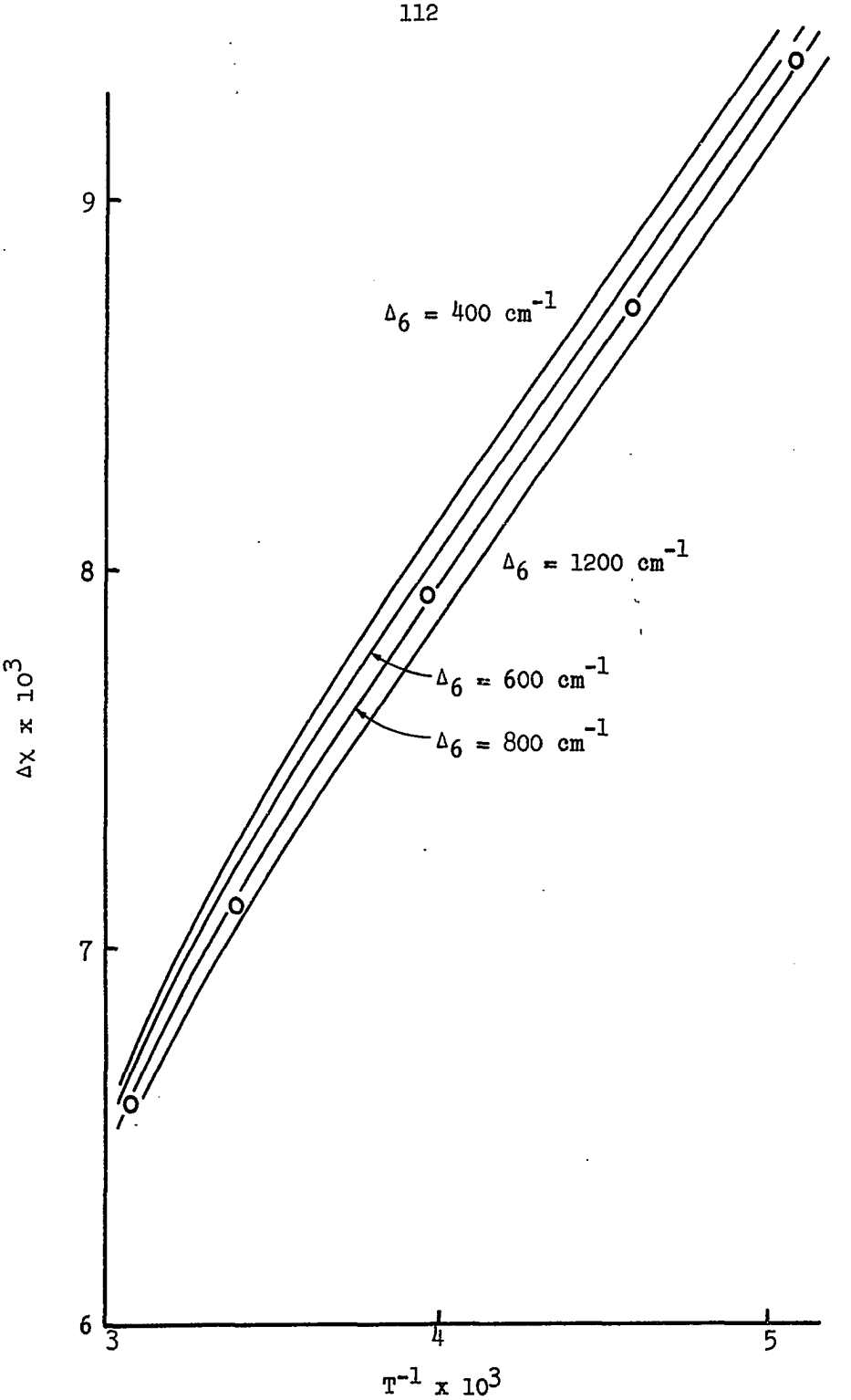

Figure 18. Magnetic Susceptibilities of YbGaG from 200-300°K

the susceptibilities over the temperature range of 200-300°K for different values of $\Gamma_6 - \Gamma_7$.

With the positions of Γ_6 and Γ_8 levels it is possible to determine the two crystal field parameters as

$$P = 25 \text{ cm}^{-1}$$

$$R = .08 \text{ cm}^{-1}$$

since $\Gamma_8 - \Gamma_7 = 20P - 168R$ and $\Gamma_6 - \Gamma_7 = 32P - 48R$.

Discussion

From the magnitude of α and the linear behavior of χ versus (1/T) at low temperatures it may be concluded that there are no crystalline Stark levels of Yb^{3+} below 515 cm^{-1}. The low-lying energy levels reported by Wood, therefore, should be attributed presumably to such effects as vibrational structure which have no appreciable effect on the magnetic properties. This interpretation is also supported by the fact that Tinkham[57] has recently observed absorption at 111 cm^{-1} for YbGaG and at 114 cm^{-1} for ErGaG which are identified as phonon transitions.

The position of the Γ_6 level will change further if one includes the effects of the crystalline fields of lower symmetry in the susceptibility formula. Also Γ_8 would be split by a lower field. It is interesting to note that Wood[53] reported two levels at 478 and 550 cm^{-1} and the effect of these two levels on α is the same as a single level at 512 cm^{-1} if both are components of the Γ_8 level. However, in the

absence of detailed information concerning the crystalline field this point will not be pursued.

Point charge calculations have been performed for this crystal[58] and the ratio of P/R was found to be -74. This ratio requires $\Gamma_6 - \Gamma_7 = 925\ cm^{-1}$ which certainly is very close to the experimental value. The ratio of P to R as calculated from the point-charge model is, therefore, in qualitative agreement with the experimental results.

CONCLUSIONS

A Faraday balance has been constructed in order to measure the magnetic susceptibilities of host crystals which have been doped with small amounts of paramagnetic ions over the temperature range of 5.7 to 1100°K. The accuracy of the susceptibility measurements obtained from the balance is about 1.5% and that of the temperature measurement is about 0.6%. For satisfactory performance of the balance the following conditions are to be met:

(i) The mass of the entire crystal is not to exceed one gram and the largest practical size is about 5 X 5 X 10 mm.

(ii) The product of the susceptibility and the mass of the sample is not to exceed 1.5×10^{-6} cgs-emu-gms. This quantity varies, of course, depending on the choice of the quartz spring. When the most sensitive spring is used, this maximum value reduces to 1.5×10^{-7}.

(iii) In the susceptibility experiments one is mainly interested in the variation of the susceptibility with respect to temperature. The minimum change in $m\chi$ should be about 1.5×10^{-8} for the temperature range of interest.

For most of the crystals which are available

commercially or grown for the special purpose of ESR and optical studies, these conditions are generally well satisfied.

For anisotropic samples at low temperatures it is necessary in some cases to use the torsion balance. The range of $(\Delta\chi)(m)$ is from 1×10^{-9} to 1.5×10^{-6} cgs-emu-gm. The temperature can be varied from 4.2 to 300°K but in these experiments only the temperatures from 4.2 to 35°K were useful.

The magnetic susceptibility has been used to determine energy levels from 4 cm^{-1} to 1100 cm^{-1}, and found to be quite effective for this purpose, particularly for those levels which could not be measured accurately by any other means. Thus in this work the zero field splitting for $V^{3+}:Al_2O_3$ was determined to be 8.4 cm^{-1} and for Co^{2+}:ZnO it was found to be about 4 cm^{-1}. The Van Vleck temperature independent susceptibility was used to locate the low-lying energy levels of 230 and 240 cm^{-1} for Ni^{2+}:CdS, 160 and 260 cm^{-1} for Ni^{2+}:ZnO, and 515 cm^{-1} for YbGaG. The trigonal splittings of the $^3T_1$ level of $V^{3+}:Al_2O_3$ was found to be 1100 cm^{-1}. The Γ_6 level of YbGaG was found to be about 800 cm^{-1} above the ground state.

In most cases it was possible, using the splittings associated with the trigonal field and $\lambda\vec{L}\cdot\vec{S}$, to calculate the spin-orbit coupling constant and the trigonal field parameters. The spin-orbit coupling constant for the doped semiconductors Ni^{2+}:ZnO (-175 cm^{-1}), Ni^{2+}:CdS (-170 cm^{-1}), and

Co^{2+}:ZnO (-104 cm^{-1}) were found to be reduced to about 50-60% of the free-ion values. The corresponding ratio of V^{3+}:Al_2O_3 is about 90%. These results are indicative of a considerable delocalization of the valence electrons of the transition element ions in the semiconducting host crystals.

The trigonal field parameters enable one to test the point charge model. The values of D_4 for Ni^{2+}:CdS (-2 cm^{-1}), Ni^{2+}:ZnO (-23 cm^{-1}), Co^{2+}:ZnO (286 cm^{-1}) and V^{3+}:Al_2O_3 (116 cm^{-1}) were found to be somewhat different from the calculated values using the point charge model. However, the differences can be explained by the assumption of a distortion of the lattice or by a displacement of the substituent. The available data do not allow one to calculate D_2 with any degree of accuracy. The results obtained for D_4 suggested a means of determining the manner in which a crystal will distort when a substituent is added.

APPENDIX I

CHARACTER TABLE FOR THE T_D AND O GROUPS

	E	$3C_2$	$6C_2$	$6C_4$	$8C_3$
A_1	1	1	1	1	1
A_2	1	1	-1	-1	1
E	2	2	0	0	-1
T_1	3	-1	-1	1	0
T_2	3	-1	1	-1	0
$\Gamma_{(L=0)}$	1	1	1	1	1
$\Gamma_{(L=1)}$	3	-1	-1	1	0
$\Gamma_{(L=2)}$	5	1	1	-1	-1
$\Gamma_{(L=3)}$	7	-1	-1	-1	1
$\Gamma_{(L=4)}$	9	1	1	1	0

$\Gamma_{(L=0)} \rightarrow A_1$

$\Gamma_{(L=1)} \rightarrow T_1$

$\Gamma_{(L=2)} \rightarrow E + T_2$

$\Gamma_{(L=3)} \rightarrow T_1 + T_2 + A_2$

$\Gamma_{(L=4)} \rightarrow T_1 + T_2 + E + A_1$

APPENDIX II

FREE ION WAVE FUNCTIONS* FOR $(3d)^8$ AND $(3d)^2$

L = 4

$$\Psi_{(4,4)} = \psi_2\varphi_2$$

$$\Psi_{(4,3)} = (1/2)^{\frac{1}{2}}(\psi_2\varphi_1 + \psi_1\varphi_2)$$

$$\Psi_{(4,2)} = (3/14)^{\frac{1}{2}}\psi_2\varphi_0 + (4/7)^{\frac{1}{2}}\psi_1\varphi_1 + (3/14)^{\frac{1}{2}}\psi_0\varphi_2$$

$$\Psi_{(4,1)} = (1/14)^{\frac{1}{2}}\psi_2\varphi_{-1} + (3/7)^{\frac{1}{2}}\psi_1\varphi_0 + (3/7)^{\frac{1}{2}}\psi_0\varphi_1 + (1/14)^{\frac{1}{2}}\psi_{-1}\varphi_2$$

$$\Psi_{(4,0)} = (1/70)^{\frac{1}{2}}\psi_2\varphi_{-2} + (8/35)^{\frac{1}{2}}\psi_1\varphi_{-1} + (18/35)^{\frac{1}{2}}\psi_0\varphi_0 + (8/35)^{\frac{1}{2}}\psi_{-1}\varphi_1 + (1/70)^{\frac{1}{2}}\psi_{-2}\varphi_2$$

$$\Psi_{(4,-1)} = (1/14)^{\frac{1}{2}}\psi_1\varphi_{-2} + (3/7)^{\frac{1}{2}}\psi_0\varphi_{-1} + (3/7)^{\frac{1}{2}}\psi_{-1}\varphi_0 + (1/14)^{\frac{1}{2}}\psi_{-2}\varphi_1$$

$$\Psi_{(4,-2)} = (3/14)^{\frac{1}{2}}\psi_0\varphi_{-2} + (3/7)^{\frac{1}{2}}\psi_{-1}\varphi_{-1} + (3/14)^{\frac{1}{2}}\psi_{-2}\varphi_0$$

$$\Psi_{(4,-3)} = (1/2)^{\frac{1}{2}}(\psi_{-1}\varphi_{-2} + \psi_{-2}\varphi_{-1})$$

$$\Psi_{(4,-4)} = \psi_{-2}\varphi_{-2}$$

L = 3

$$\Psi_{(3,3)} = (1/2)^{\frac{1}{2}}(\psi_2\varphi_1 - \psi_1\varphi_2)$$

APPENDIX II (continued)

$$\Psi_{(3,2)} = (1/2)^{\frac{1}{2}}(\psi_2\varphi_0 - \psi_0\varphi_2)$$

$$\Psi_{(3,1)} = (3/10)^{\frac{1}{2}}\psi_2\varphi_{-1} + (1/5)^{\frac{1}{2}}\psi_1\varphi_0 - (1/5)^{\frac{1}{2}}\psi_0\varphi_1 - (3/10)^{\frac{1}{2}}\psi_{-1}\varphi_2$$

$$\Psi_{(3,0)} = (1/10)^{\frac{1}{2}}\psi_2\varphi_{-2} + (2/5)^{\frac{1}{2}}\psi_1\varphi_{-1} - (2/5)^{\frac{1}{2}}\psi_{-1}\varphi_1 - (1/10)^{\frac{1}{2}}\psi_{-2}\varphi_1$$

$$\Psi_{(3,-1)} = (3/10)^{\frac{1}{2}}\psi_1\varphi_{-2} + (1/5)^{\frac{1}{2}}\psi_0\varphi_{-1} - (1/5)^{\frac{1}{2}}\psi_{-1}\varphi_0 - (3/10)^{\frac{1}{2}}\psi_{-2}\varphi_1$$

$$\Psi_{(3,-2)} = (\psi_0\varphi_{-2} - \psi_{-2}\varphi_0)(\tfrac{1}{2})^{\frac{1}{2}}$$

$$\Psi_{(3,-3)} = (\psi_{-1}\varphi_{-2} - \psi_{-2}\varphi_{-1})(\tfrac{1}{2})^{\frac{1}{2}}$$

L = 2

$$\Psi_{(2,2)} = (2/7)^{\frac{1}{2}}\psi_2\varphi_0 - (3/7)^{\frac{1}{2}}\psi_1\varphi_1 + (2/7)^{\frac{1}{2}}\psi_0\varphi_2$$

$$\Psi_{(2,1)} = (3/7)^{\frac{1}{2}}\psi_2\varphi_{-1} - (1/14)^{\frac{1}{2}}\psi_1\varphi_0 - (1/14)^{\frac{1}{2}}\psi_0\varphi_1 + (3/7)^{\frac{1}{2}}\psi_{-1}\varphi_2$$

$$\Psi_{(2,0)} = (2/7)^{\frac{1}{2}}\psi_2\varphi_{-2} + (1/14)^{\frac{1}{2}}\psi_1\varphi_{-1} - (2/7)^{\frac{1}{2}}\psi_0\varphi_0 + (1/14)^{\frac{1}{2}}\psi_{-1}\varphi_1 + (2/7)^{\frac{1}{2}}\psi_{-2}\varphi_2$$

$$\Psi_{(2,-1)} = (3/7)^{\frac{1}{2}}\psi_1\varphi_{-2} - (1/14)^{\frac{1}{2}}\psi_0\varphi_{-1} - (1/14)^{\frac{1}{2}}\psi_{-1}\varphi_0 + (3/7)^{\frac{1}{2}}\psi_{-2}\varphi_1$$

$$\Psi_{(2,-2)} = (2/7)^{\frac{1}{2}}\psi_0\varphi_{-2} - (3/7)^{\frac{1}{2}}\psi_{-1}\varphi_{-1} + (2/7)^{\frac{1}{2}}\psi_{-2}\varphi_0$$

APPENDIX II (continued)

L = 1

$$\Psi(1,1) = (1/5)^{\frac{1}{2}}\psi_2\varphi_{-1} - (3/10)^{\frac{1}{2}}\psi_1\varphi_0 + (3/10)^{\frac{1}{2}}\psi_0\varphi_1 - (1/5)^{\frac{1}{2}}\psi_{-1}\varphi_2$$

$$\Psi(1,0) = (2/5)^{\frac{1}{2}}\psi_2\varphi_{-2} - (1/10)^{\frac{1}{2}}\psi_1\varphi_{-1} + (1/10)^{\frac{1}{2}}\psi_{-1}\varphi_1 - (2/5)^{\frac{1}{2}}\psi_{-2}\varphi_2$$

$$\Psi(1,-1) = (1/5)^{\frac{1}{2}}\psi_1\varphi_{-2} - (3/10)^{\frac{1}{2}}\psi_0\varphi_{-1} + (3/10)^{\frac{1}{2}}\psi_{-1}\varphi_0 - (1/5)^{\frac{1}{2}}\psi_{-2}\varphi_1$$

L = 0

$$\Psi(0,0) = (1/5)^{\frac{1}{2}}\psi_2\varphi_{-2} - (1/5)^{\frac{1}{2}}\psi_1\varphi_{-1} + (1/5)^{\frac{1}{2}}\psi_0\varphi_0 - (1/5)^{\frac{1}{2}}\psi_{-1}\varphi_1 + (1/5)^{\frac{1}{2}}\psi_{-2}\varphi_2$$

---

*$\Psi(L,M_L) = \Sigma c_i \psi_{m_1}\varphi_{m_2}$

APPENDIX III

MATRIX ELEMENTS OF V_c IN THE (LM) REPRESENTATION IN UNITS OF β

^1G

M =	4(-4)	1(-1)	-2(2)
	2	$10(10)^{\frac{1}{2}}/7$	0
		9/7	-10/7
			-11/7

$E_{A_1} = E_{(G)} - 6\beta$

$E_E = E_{(G)} - 6\beta/7$

M =	3	0	-3
	-3	$-3(70)^{\frac{1}{2}}/7$	0
		18/7	$3(10)^{\frac{1}{2}}/7$
			-3

$E_{T_1} = E_{(G)} - 3\beta$

$E_{T_2} = E_{(G)} + 39\beta/7$

^3F

M =	3	0	-3
	-3	$3(10)^{\frac{1}{2}}$	0
		-6	$-3(10)^{\frac{1}{2}}$
			-3

M =	2(-2)	-1(1)
	7	$\pm 2(5)^{\frac{1}{2}}$
		-1

$E_{A_2} = E_{(F)} - 18\beta$

$E_{T_1} = E_{(F)} - 3\beta$

$E_{T_2} = E_{(F)} + 9\beta$

^1D

$M =$	$2(-2)$	$-1(1)$
		$\mp 20(2)^{\frac{1}{2}}/7$
		$-16/7$

$M =$	0
	$24/7$

$E_E = E_{(D)} - 36\beta/7$

$E_{T_2} = E_{(D)} + 24\beta/7$

^3P

$M =$	$1(0)(-1)$
	0

$E_{T_1} = E(P)$

^1S

$M =$	0
	0

$E_{A_1} = E(S)$

APPENDIX IV

CUBIC FIELD ORBITAL WAVE FUNCTIONS

$$\Psi_{(^1GA_1)} = \{(10)^{\frac{1}{2}}\Psi(4,3) + (7)^{\frac{1}{2}}\Psi(4,0) - (10)^{\frac{1}{2}}\Psi(4,-3)\}/3(3)^{\frac{1}{2}}$$

$$^1G$$

$$\Psi(^1GE^+) = \{(7)^{\frac{1}{2}}\Psi(4,4) + 2\Psi(4,1) + 4\Psi(4,-2)\}/3(3)^{\frac{1}{2}}$$

$$\Psi(^1GE^-) = \{-(7)^{\frac{1}{2}}\Psi(4,-4) + 2\Psi(4,-1) - 4\Psi(4,2)\}/3(3)^{\frac{1}{2}}$$

$$\Psi(^1GT_1^+) = \{-2\Psi(4,4) - (7)^{\frac{1}{2}}\Psi(4,1) + (7)^{\frac{1}{2}}\Psi(4,-2)\}/3(2)^{\frac{1}{2}}$$

$$\Psi(^1GT_1^o) = \{\Psi(4,3) + \Psi(4,-3)\}/(2)^{\frac{1}{2}}$$

$$\Psi(^1GT_1^-) = \{-2\Psi(4,-4) + (7)^{\frac{1}{2}}\Psi(4,-1) + (7)^{\frac{1}{2}}\Psi(4,2)\}/3(2)^{\frac{1}{2}}$$

$$\Psi(^1GT_2^+) = \{-2(7)^{\frac{1}{2}}\Psi(4,4) + 5\Psi(4,1) + \Psi(4,-2)\}/3(6)^{\frac{1}{2}}$$

$$\Psi(^1GT_2^o) = \{(7)^{\frac{1}{2}}\Psi(4,3) - 2(10)^{\frac{1}{2}}\Psi(4,0) - (7)^{\frac{1}{2}}\Psi(4,-3)\}/3(6)^{\frac{1}{2}}$$

$$\Psi(^1GT_2^-) = \{2(7)^{\frac{1}{2}}\Psi(4,-4) + 5\Psi(4,-1) - \Psi(4,2)\}/3(6)^{\frac{1}{2}}$$

$$^1D$$

$$\Psi(^1DE^-) = \{(2)^{\frac{1}{2}}\Psi(2,1) - \Psi(2,-2)\}/(3)^{\frac{1}{2}}$$

$$\Psi(^1DE^+) = \{\Psi(2,2) + (2)^{\frac{1}{2}}\Psi(2,-1)\}/(3)^{\frac{1}{2}}$$

$$\Psi(^1DT_2^+) = \{(2)^{\frac{1}{2}}\Psi(2,2) - \Psi(2,-1)\}/(3)^{\frac{1}{2}}$$

APPENDIX IV (continued)

$$\Psi(^1DT_2^0) = \Psi(2,0)$$

$$\Psi(^1DT_2^-) = \{\Psi(2,1) + (2)^{\frac{1}{2}}\Psi(2,-2)\}/(3)^{\frac{1}{2}}$$

^1S

$$\Psi(^1SA_1) = \Psi(0,0)$$

^3F

$$\Psi(^3F^3A_2) = \{-(2)^{\frac{1}{2}}\Psi(3,3) + (5)^{\frac{1}{2}}\Psi(3,0) + (2)^{\frac{1}{2}}\Psi(3,-3)\}/3$$

$$\Psi(^3F^3T_2^+) = \{\Psi(3,2) - (5)^{\frac{1}{2}}\Psi(3,-1)\}/(6)^{\frac{1}{2}}$$

$$\Psi(^3F^3T_2^0) = \{\Psi(3,3) + \Psi(3,-3)\}/(2)^{\frac{1}{2}}$$

$$\Psi(^3F^3T_2^-) = \{(5)^{\frac{1}{2}}\Psi(3,1) + \Psi(3,-2)\}/(6)^{\frac{1}{2}}$$

$$\Psi(^3F^3T_1^+) = \{-(5)^{\frac{1}{2}}\Psi(3,2) - \Psi(3,-1)\}/(6)^{\frac{1}{2}}$$

$$\Psi(^3F^3T_1^0) = \{(5)^{\frac{1}{2}}\Psi(3,3) + (8)^{\frac{1}{2}}\Psi(3,0) - (5)^{\frac{1}{2}}\Psi(3,-3)\}/3(2)^{\frac{1}{2}}$$

$$\Psi(^3F^3T_1^-) = \{-\Psi(3,1) + (5)^{\frac{1}{2}}\Psi(3,-2)\}/(6)^{\frac{1}{2}}$$

^3P

$$\Psi(^3P^3T_1^+) = \Psi(1,1)$$

$$\Psi(^3P^3T_1^0) = \Psi(1,0)$$

$$\Psi(^3P^3T_1^-) = \Psi(1,-1)$$

APPENDIX V

ENERGY MATRIX FOR $(3d)^2$ AND $(3d)^8$ IN CUBIC REPRESENTATION

A Levels

$^3F\,^3T_1^+S_1$	$^3F\,^3T_1^oS_o$	$^3FT_1^-S_{-1}$	$^3FT_2^+S_1$	$^3FT_2^oS_o$
$(3/2)\lambda + A$	$-(3/2)\lambda$		$-\frac{1}{2}(5)^{\frac{1}{2}}\lambda + R$	$-\frac{1}{2}(5)^{\frac{1}{2}}\lambda$
	B	$-(3/2)\lambda$	$\frac{1}{2}(5)^{\frac{1}{2}}\lambda$	
		$(3/2)\lambda + A$		$\frac{1}{2}(5)^{\frac{1}{2}}\lambda$
			$8Dq - \frac{1}{2}\lambda + C$	$\frac{1}{2}\lambda$
				$8Dq - D$

A Levels

$^3_F{}^3T_2^-S_{-1}$	$^3_F{}^3A_2S_o$	$^3_P{}^3T_1^+S_{-1}$	$^3_P{}^3T_1^oS_o$	$^3_P{}^3T_1^-S_1$
		$6\beta + D_4 - \frac{1}{5}(20)^{\frac{1}{2}}D_2$		
$\frac{1}{2}(5)^{\frac{1}{2}}\lambda$	S		$6\beta + \frac{8}{3}D_4 - \frac{8}{5}(5)^{\frac{1}{2}}D_2$	$6\beta + D_4 + \frac{1}{5}(20)^{\frac{1}{2}}D_2$
$\frac{1}{2}(5)^{\frac{1}{2}}\lambda$				$-(5)^{\frac{1}{2}}D_4 - 4D_2$
	-2λ			
$\frac{1}{2}\lambda$				
$8Dq - \frac{1}{2}\lambda + C$	2λ	$(5)^{\frac{1}{2}}D_4 - 4D_2$		
	$18Dq + F$			
		$\Delta_p + G - \lambda$	λ	
			$\Delta_p - 2G$	λ
				$\Delta_p + G - \lambda$

E Levels

$^3_F{}^3T_1^+S_{-1}$	$^3_F{}^3T_1^oS_1$	$^3_F{}^3T_1^-S_o$	$^3_F{}^3T_2^+S_{-1}$	$^3_F{}^3T_2^oS_1$
$A - (3/2)\lambda$			$\frac{1}{2}(5)^{\frac{1}{2}}\lambda + R$	
	B	$-(3/2)\lambda$		$(5)^{\frac{1}{2}}\lambda$
		A	$-(5)^{\frac{1}{2}}\lambda$	$\frac{1}{2}(5)^{\frac{1}{2}}\lambda$
			$8Dq + \frac{1}{2}\lambda + C$	
				$8Dq - D$

E Levels

$^3_F{}^3T_2^-S_o$	$^3_F{}^3A_2S_1$	$^3_P{}^3T_1^-S_{-1}$	$^3_P{}^3T_1^oS_1$	$^3_P{}^3T_1^+S_o$
$-(5)^{\frac{1}{2}}\lambda$		$6\beta + D_4 + \frac{1}{5}(20)^{\frac{1}{2}}D_2$		
$\frac{1}{2}(5)^{\frac{1}{2}}\lambda$	S		$6\beta + \frac{8}{3}D_4 - \frac{8}{5}(5)^{\frac{1}{2}}D_2$	
$-R$				$6\beta + D_4 + \frac{1}{5}(20)^{\frac{1}{2}}D_2$
		$-(5)^{\frac{1}{2}}D_4 - 4D_2$		
$\frac{1}{2}\lambda$	-2λ			
$8Dq + C$	2λ			$(5)^{\frac{1}{2}}D_4 - 4D_2$
	$18\ Dq + F$		$\frac{4}{3}(5)^{\frac{1}{2}}D_4 - 4D_2$	
		$\Delta_p + 6Dq + \lambda + G$		
			$\Delta_p + 6Dq - 2G$	λ
				$\Delta_p + 6Dq + G$

APPENDIX V (continued)

$$A = (17/3)D_4 + (5)^{\frac{1}{2}}D_2/10$$

$$B = -(13/3)D_4 - (5)^{\frac{1}{2}}D_2/5$$

$$C = (1/3)D_4 + \tfrac{1}{2}(5)^{\frac{1}{2}}D_2$$

$$D = -3D_4 + (5)^{\frac{1}{2}}D_2$$

$$R = (5)^{\frac{1}{2}}\{(-4/3)D_4 + (5)^{\frac{1}{2}}D_2/10\}$$

$$S = -(2/3)(5)^{\frac{1}{2}}D_4 + 2D_2$$

$$G = 7(5)^{\frac{1}{2}}D_2/5$$

$$F = -14D_4/3$$

APPENDIX VI

MATRIX ELEMENTS OF $\vec{L}$ AND $\vec{S}$ (UNITS OF $h/2\pi$)

(LM) REPRESENTATION

^3F

$(LM_L|L_z|LM_L) = M_L \ (=2, 1, 0, -1, -2)$

$(SM_S|L_z|SM_S) = M_S$

$(33|L_x|32) = \frac{1}{2}(6)^{\frac{1}{2}}$

$(32|L_x|31) = \frac{1}{2}(10)^{\frac{1}{2}}$

$(31|L_x|30) = \frac{1}{2}(12)^{\frac{1}{2}}$

$(30|L_x|3\text{-}1) = \frac{1}{2}(12)^{\frac{1}{2}}$

$(3\text{-}1|L_x|3\text{-}2) = \frac{1}{2}(10)^{\frac{1}{2}}$

$(3\text{-}2|L_x|3\text{-}3) = \frac{1}{2}(6)^{\frac{1}{2}}$

$(S1|S_x|S0) = \frac{1}{2}(2)^{\frac{1}{2}}$

$(S0|S_x|S\text{-}1) = \frac{1}{2}(2)^{\frac{1}{2}}$

^3P

$(LM_L|L_z|LM_L) = M_L \ (=1, 0, -1)$

$(SM_S|S_z|SM_S) = M_S \ (=1, 0, -1)$

$(11|L_x|10) = \frac{1}{2}(2)^{\frac{1}{2}}$

$(10|L_x|1\text{-}1) = \frac{1}{2}(2)^{\frac{1}{2}}$

$(S1|S_x|S0) = \frac{1}{2}(2)^{\frac{1}{2}}$

APPENDIX VI (continued)

$(SO|S_x|S\text{-}1) = \frac{1}{2}(2)^{\frac{1}{2}}$

CUBIC REPRESENTATION

$|L_z + gS_z|$

$^3P(^3T_1)$

$(T^+S_1|T^+S_1) = 1 + g$

$(T^+S_o|T^+S_o) = 1$

$(T^+S_{-1}|T^+S_{-1}) = 1 - g$

$(T^oS_1|T^oS_1) = g$

$(T^oS_o|T^oS_o) = 0$

$(T^oS_{-1}|T^oS_{-1}) = -g$

$(T^-S_1|T^-S_1) = -1 + g$

$(T^-S_o|T^-S_o) = -1$

$(T^-S_{-1}|T^-S_{-1}) = -1 - g$

$^3F(^3T_1)$

$(T_1^+S_1|T_1^+S_1) = 3/2 + g$

$(T_1^+S_o|T_1^+S_o) = 3/2$

$(T_1^+S_{-1}|T_1^+S_{-1}) = (3/2) - g$

$(T_1^oS_1|T_1^oS_1) = g$

$(T_1^oS_o|T_1^oS_o) = 0$

$(T_1^oS_{-1}|T_1^oS_{-1}) = -g$

$(T_1^-S_1|T_1^-S_1) = -(3/2) + g$

$(T_1^-S_o|T_1^-S_o) = -(3/2)$

$(T_1^-S_{-1}|T_1^-S_{-1}) = -(3/2) - g$

$^3F(^3T_1)$-$^3F(^3T_2)$

$(T_1^+|T_2^+) = -\frac{1}{2}(5)^{\frac{1}{2}}$

APPENDIX VI (continued)

$(T_1^o|T_2^o) = (5)^{\frac{1}{2}}$

$(T_1^-|T_2^-) = -\frac{1}{2}(5)^{\frac{1}{2}}$

$^3T_2(^3F)$

$(T_2^+S_1|T_2^+S_1) = -\frac{1}{2} + g$

$(T_2^+S_o|T_2^+S_o) = -\frac{1}{2}$

$(T_2^+S_{-1}|T_2^+S_{-1}) = -\frac{1}{2} - g$

$(T_2^oS_1|T_2^oS_1) = g$

$(T_2^oS_o|T_2^oS_o) = 0$

$(T_2^oS_{-1}|T_2^oS_{-1}) = -g$

$(T_2^-S_1|T_2^-S_1) = \frac{1}{2} + g$

$(T_2^-S_o|T_2^-S_o) = \frac{1}{2}$

$(T_2^-S_{-1}|T_2^-S_{-1}) = \frac{1}{2} - g$

$^3T_2(^3F)$-$^3A_2(^3F)$

$(T_2^o|^3A_2) = -2$

$|L_x + gS_x|$

$^3T_1(^3F)$

$(T_1^+M_S|T_1^oM_S) = -(3/4)(2)^{\frac{1}{2}}$

$(T_1^+M_S|T_1^-M_S) = 0$

$(T_1^oM_S|T_1^-M_S) = -(3/4)(2)^{\frac{1}{2}}$

$(T_1^+S_1|T_1^+S_o) = \frac{1}{2}g(2)^{\frac{1}{2}} = (T_1^+S_o|T_1^+S_{-1})$

$(T_1^oS_1|T_1^oS_o) = \frac{1}{2}g(2)^{\frac{1}{2}} = (T_1^oS_o|T_1^oS_{-1})$

$(T_1^-S_1|T_1^-S_o) = \frac{1}{2}g(2)^{\frac{1}{2}} = (T_1^-S_o|T_1^-S_{-1})$

$^3T_2(^3F)$

$(T_2^+M_S|T_2^oM_S) = \frac{1}{4}(2)^{\frac{1}{2}}$

APPENDIX VI (continued)

$(T_2^0 M_S | T_2^- M_S) = \frac{1}{4}(2)^{\frac{1}{2}}$

$(T_2^+ M_S | T_2^+ M_S) = 0$

$(T_2^+ S_1 | T_2^+ S_0) = \frac{1}{2}(2)^{\frac{1}{2}} g = (T_2^+ S_0 | T_2^+ S_{-1})$

$(T_2^0 S_1 | T_2^0 S_0) = \frac{1}{2}(2)^{\frac{1}{2}} g = (T_2^0 S_0 | T_2^0 S_{-1})$

$(T_2^- S_1 | T_2^- S_0) = \frac{1}{2}(2)^{\frac{1}{2}} g = (T_2^- S_0 | T_2^- S_{-1})$

$^3T_1(^3F) - ^3T_2(^3F)$

$(T_1^+ M_S | T_2^0 M_S) = -\frac{1}{4}(10)^{\frac{1}{2}}$

$(T_1^+ M_S | T_2^- M_S) = -\frac{1}{2}(10)^{\frac{1}{2}}$

$(T_1^0 M_S | T_2^+ M_S) = -\frac{1}{4}(10)^{\frac{1}{2}}$

$(T_1^0 M_S | T_2^- M_S) = \frac{1}{4}(10)^{\frac{1}{2}}$

$(T_1^- M_S | T_2^+ M_S) = -\frac{1}{2}(10)^{\frac{1}{2}}$

$(T_1^- M_S | T_2^0 M_S) = \frac{1}{4}(10)^{\frac{1}{2}}$

$^3A_2(^3F) - ^3T_2(^3F)$

$(^3A_2 M_S | T_2^+ M_S) = -(2)^{\frac{1}{2}}$

$(^3A_2 M_S | T_2^0 M_S) = 0$

$(^3A_2 M_S | T_2^- M_S) = (2)^{\frac{1}{2}}$

$^3T_1(^3P)$

$(T_1^+ M_S | T_1^0 M_S) = \frac{1}{2}(2)^{\frac{1}{2}}$

$(T_1^0 M_S | T_1^- M_S) = \frac{1}{2}(2)^{\frac{1}{2}}$

$(T_1^+ S_1 | T_1^+ S_0) = \frac{1}{2}(2)^{\frac{1}{2}} g = (T_1^+ S_0 | T_1^+ S_{-1})$

$(T_1^0 S_1 | T_1^0 S_0) = \frac{1}{2}(2)^{\frac{1}{2}} g = (T_1^0 S_0 | T_1^0 S_{-1})$

$(T_1^- S_1 | T_1^- S_0) = \frac{1}{2}(2)^{\frac{1}{2}} g = (T_1^- S_0 | T_1^- S_{-1})$

APPENDIX VII

MATRIX ELEMENTS OF V_c IN THE (JM_J) REPRESENTATION FOR Yb^{3+}

$^2F_{7/2}$

M_J =	7/2(-7/2)	$-\frac{1}{2}(\frac{1}{2})$
	7P + 6R	$(35)^{\frac{1}{2}}$(P - 18R)
		9P - 30R

M_J =	5/2(-5/2)	-3/2(3/2)
	-13P - 30R	$(3)^{\frac{1}{2}}$(5P + 42R)
		-3P + 54R

where $P = 3\left(\frac{70}{9}\right)\left(\frac{ze^2\alpha_s}{R^5}\right)\left(\frac{-2}{15 \times 77}\right)\langle r^4\rangle$

and $R = 3\left(\frac{70}{9}\right)\left(\frac{ze^2\alpha_s'}{R^7}\right)\left(\frac{4}{13 \times 33 \times 63}\right)\langle r^6\rangle$

APPENDIX VIII

MATRIX ELEMENTS OF $|\vec{L} + 2\vec{S}|$ IN THE (JM_J) REPRESENTATION FOR Yb^{3+}

$$^2F_{7/2}$$

$$|L_z + 2S_z|$$

$(7/2|7/2) = 4$

$(5/2|5/2) = 20/7$

$(3/2|3/2) = 12/7$

$(1/2|1/2) = 4/7$

$(-1/2|-1/2) = -4/7$

$(-3/2|-3/2) = -12/7$

$(-5/2|-5/2) = -20/7$

$(-7/2|-7/2) = -4$

$$|L_x + 2S_x|$$

$(7/2|5/2) = 4(7)^{\frac{1}{2}}/7$

$(5/2|3/2) = 8(3)^{\frac{1}{2}}/7$

$(3/2|1/2) = 4(15)^{\frac{1}{2}}/7$

$(1/2|-1/2) = 16/7$

$(-1/2|-3/2) = 4(15)^{\frac{1}{2}}/7$

$(-3/2|-5/2) = 8(3)^{\frac{1}{2}}/7$

$(-5/2|-7/2) = 4(7)^{\frac{1}{2}}/7$

APPENDIX IX

MATRIX ELEMENTS AND SUSCEPTIBILITY EQUATIONS FOR NICKEL IN TETRAHEDRAL SITES

If the energy matrix of the (^3F) states is solved using $\lambda = -175\ cm^{-1}$ and $K = -225\ cm^{-1}$ then the eigenvectors for the $^3T_1$ states are given by

$$\begin{bmatrix} A_{11} \\ A_{12} \\ A_{13} \\ A_{14} \end{bmatrix} = \begin{bmatrix} 0.9906 \\ 0.1327 \\ 0.0309 \\ 0.0059 \end{bmatrix} \qquad \begin{bmatrix} A_{21} \\ A_{22} \\ A_{23} \end{bmatrix} = \begin{bmatrix} 0.9938 \\ 0.0155 \\ 0.1104 \end{bmatrix}$$

$$\begin{bmatrix} A_{31} \\ A_{32} \\ A_{33} \\ A_{34} \\ A_{35} \\ A_{36} \\ A_{37} \end{bmatrix} = \begin{bmatrix} 0.9699 \\ 0.1906 \\ 0.1138 \\ 0.0030 \\ 0.0438 \\ 0.0902 \\ 0.0048 \end{bmatrix} \qquad \begin{bmatrix} A_{41} \\ A_{42} \\ A_{43} \\ A_{44} \\ A_{45} \\ A_{46} \\ A_{47} \end{bmatrix} = \begin{bmatrix} 0.0886 \\ 0.7852 \\ 0.5912 \\ 0.0662 \\ 0.1440 \\ 0.0325 \\ 0.0022 \end{bmatrix}$$

APPENDIX IX (continued)

$$\begin{bmatrix} A_{51} \\ A_{52} \\ A_{53} \\ A_{54} \end{bmatrix} = \begin{bmatrix} 0.1355 \\ 0.9827 \\ 0.1263 \\ 0.0010 \end{bmatrix} \qquad \begin{bmatrix} A_{61} \\ A_{62} \\ A_{63} \\ A_{64} \\ A_{65} \\ A_{66} \\ A_{67} \end{bmatrix} = \begin{bmatrix} 0.2049 \\ 0.5547 \\ 0.7908 \\ 0.0859 \\ 0.1295 \\ 0.0250 \\ 0.0135 \end{bmatrix}$$

and the eigenvalues are given by

$E(A_1) = -691.4\ cm^{-1}$ $\qquad$ $E(EE) = -29.6\ cm^{-1}$

$E(T_1A_2) = -531.1\ cm^{-1}$ $\qquad$ $E(T_2A_1) = 152.6\ cm^{-1}$

$E(T_1E) = -431.9\ cm^{-1}$ $\qquad$ $E(T_2E) = 86.5\ cm^{-1}$.

The components of the eigenvectors are labeled so that the first index represents the particular state with which it is associated and the second represents the component. The states A_1, T_1A_2, T_1E, EE, T_2A_1, and T_2E are represented by the numbers 1, 2, 3, 4, 5, and 6, respectively.

If the (A_1) and (T_2A_1) wave functions are represented by both (i) and (p); T_1E, (EE), and (T_2E) by (j), (l), and (m); and (T_1A_2) by both (q) and (k) then the matrix elements of $|\vec{L} + 2\vec{S}|$ are

APPENDIX IX (continued)

$|L_z + 2S_z|$

$$(p|L_z + 2S_z|q) = \left(\frac{-7\sqrt{6}}{6}\right)A_{p1}A_{q1} + \left(-\tfrac{1}{2}\sqrt{10}\right)A_{p1}A_{q3} + (-7/2\sqrt{3})A_{p2}A_{q1}$$
$$+ \left(-\tfrac{1}{2}\sqrt{10}\right)A_{p1}A_{q2} + \left(\tfrac{1}{2}\sqrt{5}\right)A_{p2}A_{q3} + \left(-\tfrac{1}{2}\sqrt{5}\right)A_{p3}A_{q1}$$
$$+ \left(-\tfrac{1}{2}\sqrt{3}\right)A_{p3}A_{q3} + (2/\sqrt{3})A_{p4}A_{q2} - (4/\sqrt{6})A_{p4}A_{q3}$$

$$(1|L_z + 2S_z|m) = \left(\tfrac{1}{4}\right)A_{11}A_{m1} + (-7/2\sqrt{6})A_{12}A_{m1} + (7/2\sqrt{6})A_{13}A_{m1}$$
$$+ (-7/2\sqrt{6})A_{11}A_{m2} + \left(-\tfrac{1}{4}\sqrt{2}\right)A_{13}A_{m2} + (7/2\sqrt{6})A_{11}A_{m3}$$
$$+ \left(-\tfrac{1}{4}\sqrt{2}\right)A_{12}A_{m3} + \left(\tfrac{1}{4}\right)A_{13}A_{m3} + \left(\tfrac{1}{4}\sqrt{5}\right)A_{11}A_{m4}$$
$$+ \left(\tfrac{1}{4}\sqrt{15}\right)A_{13}A_{m4} + \left(-\tfrac{1}{4}\sqrt{30}\right)A_{11}A_{m5} + \left(-\tfrac{1}{4}\sqrt{10}\right)A_{13}A_{m5}$$
$$+ \left(\tfrac{1}{4}\sqrt{15}\right)A_{11}A_{m6} + \left(-\tfrac{1}{4}\sqrt{10}\right)A_{12}A_{m6} + \left(-\tfrac{1}{4}\sqrt{5}\right)A_{13}A_{m6}$$
$$+ \left(\tfrac{1}{4}\sqrt{5}\right)A_{14}A_{m1} + \left(-\tfrac{1}{4}\sqrt{30}\right)A_{15}A_{m1} + \left(\tfrac{1}{4}\sqrt{15}\right)A_{16}A_{m1}$$
$$+ \left(-\tfrac{1}{4}\sqrt{10}\right)A_{16}A_{m2} + \left(\tfrac{1}{4}\sqrt{15}\right)A_{14}A_{m3} + \left(-\tfrac{1}{4}\sqrt{10}\right)A_{15}A_{m3}$$
$$+ \left(-\tfrac{1}{4}\sqrt{5}\right)A_{16}A_{m3} + (5/4)A_{14}A_{m4} + \left(-\tfrac{1}{4}\sqrt{6}\right)A_{15}A_{m4}$$
$$+ \left(\tfrac{1}{4}\sqrt{3}\right)A_{16}A_{m4} + (\sqrt{2})A_{17}A_{m4} + \left(-\tfrac{1}{4}\sqrt{6}\right)A_{14}A_{m5}$$
$$+ (-5\sqrt{2}/4)A_{16}A_{m5} + (-2/\sqrt{3})A_{17}A_{m5} + \left(\tfrac{1}{4}\sqrt{3}\right)A_{14}A_{m6}$$
$$+ (-5\sqrt{2}/4)A_{15}A_{m6} + (5/4)A_{16}A_{m6} + (\sqrt{6}/3)A_{17}A_{m6}$$
$$+ (\sqrt{2})A_{14}A_{m7} + (-2/3)A_{15}A_{m7} + (\sqrt{6}/3)A_{16}A_{m7}$$
$$+ (2)A_{17}A_{m7}$$

APPENDIX IX (continued)

$$|L_x + 2S_x|$$

$$(i|L_x + 2S_x|j) = (7/2\sqrt{3})A_{i1}A_{j1} + (-7/4\sqrt{6})A_{i2}A_{j1}$$
$$+ (-\sqrt{10}/8)A_{i3}A_{j1} + (\tfrac{1}{4})A_{i2}A_{j2} + (\tfrac{1}{4}\sqrt{15})A_{i3}A_{j2}$$
$$+ (-\sqrt{2}/8)A_{i2}A_{j3} + (\sqrt{30}/8)A_{i3}A_{j3} + (\sqrt{30}/8)A_{i2}A_{j4}$$
$$+ (5\sqrt{2}/8)A_{i3}A_{j4} + A_{i4}A_{j4} + (\tfrac{1}{4}\sqrt{5})A_{i2}A_{j5}$$
$$+ (\tfrac{1}{4}\sqrt{3})A_{i3}A_{j5} + A_{i4}A_{j5} + (\tfrac{1}{2}\sqrt{5})A_{i1}A_{j6}$$
$$+ (\sqrt{10}/8)A_{i2}A_{j6} + (-\sqrt{6}/8)A_{i3}A_{j6} + (-1/\sqrt{3})A_{i4}A_{j6}$$
$$+ A_{i3}A_{j7} + (\sqrt{2})A_{i4}A_{j7}$$

$$(k|L_x + 2S_x|j) = (\sqrt{2}/8)A_{k1}A_{j1} + (\sqrt{30}/8)A_{k3}A_{j1} + (7/4\sqrt{3})A_{k1}A_{j2}$$
$$+ (\tfrac{1}{4}\sqrt{5})A_{k3}A_{j2} + (-7/4\sqrt{6})A_{k1}A_{j3} + (\tfrac{1}{2}\sqrt{5})A_{k2}A_{j3}$$
$$+ (\sqrt{10}/8)A_{k3}A_{j3} + (-\sqrt{10}/8)A_{k1}A_{j4} + (\tfrac{1}{2}\sqrt{3})A_{k2}A_{j4}$$
$$+ (-\sqrt{6}/8)A_{k3}A_{j4} + (\tfrac{1}{4}\sqrt{15})A_{k1}A_{j5} + (\sqrt{6}/8)A_{k3}A_{j5}$$
$$+ (\sqrt{30}/8)A_{k1}A_{j6} + (-5\sqrt{2}/8)A_{k3}A_{j6}$$
$$+ (-\sqrt{6}/3)A_{k2}A_{j7} + (-1/\sqrt{3})A_{k3}A_{j7}$$

$$(l|L_x + 2S_x|m) = (7/4\sqrt{3})A_{l2}A_{m1} + (7/2\sqrt{6})A_{l3}A_{m1} + (7/4\sqrt{3})A_{l1}A_{m2}$$
$$+ (-\tfrac{1}{4})A_{l3}A_{m2} + (7/2\sqrt{6})A_{l1}A_{m3} + (\tfrac{1}{4})A_{l2}A_{m3}$$
$$+ (\tfrac{1}{4}\sqrt{10})A_{l1}A_{m4} + (\tfrac{1}{4}\sqrt{15})A_{l2}A_{m4} + (-\tfrac{1}{4}\sqrt{15})A_{l1}A_{m5}$$

APPENDIX IX (continued)

$$+ (\tfrac{1}{14}\sqrt{5})A_{13}A_{m5} + (\tfrac{1}{14}\sqrt{5})A_{12}A_{m6} + (-\tfrac{1}{14}\sqrt{10})A_{13}A_{m6}$$

$$+ (\tfrac{1}{14}\sqrt{10})A_{14}A_{m1} + (\tfrac{1}{14}\sqrt{15})A_{15}A_{m1} + (-\tfrac{1}{14}\sqrt{15})A_{14}A_{m2}$$

$$+ (\tfrac{1}{14}\sqrt{5})A_{16}A_{m2} + (\tfrac{1}{14}\sqrt{5})A_{15}A_{m3} + (-\tfrac{1}{14}\sqrt{10})A_{16}A_{m3}$$

$$+ (\tfrac{1}{14}\sqrt{3})A_{15}A_{m4} + (-\tfrac{1}{14}\sqrt{6})A_{16}A_{m4} + (\tfrac{1}{14}\sqrt{3})A_{14}A_{m5}$$

$$+ (-5/4)A_{16}A_{m5} + (-2/\sqrt{6})A_{17}A_{m5} + (-\tfrac{1}{14}\sqrt{6})A_{14}A_{m6}$$

$$+ (5/4)A_{15}A_{m6} + (1/\sqrt{3})A_{17}A_{m6} + (-2/\sqrt{6})A_{15}A_{m7}$$

$$+ (2/\sqrt{3})A_{16}A_{m7}$$

The matrix elements for the susceptibility equations using $\lambda = -175$ and $K = -225$ cm^{-1} are

$$|L_x + 2S_x|$$

(1|3) = 1.9582
(1|4) = -0.1353
(1|6) = 0.3792
(2|3) = 0.6152
(2|4) = 0.5279
(2|6) = -1.2040
(3|3) = 0.0929
(3|6) = 0.7567
(3|4) = 1.5335
(4|4) = -0.1923
(3|5) = -0.8676
(4|5) = 0.4612
(5|6) = -0.4876
(4|6) = 0.6957
(6|6) = 0.0912

APPENDIX IX (continued)

$|L_z + 2S_z|$

$(1|2) = -3.2778$ $\qquad$ $(4|4) = -0.0772$

$(2|5) = -1.6202$ $\qquad$ $(3|3) = -0.4490$

$(3|4) = -0.5836$ $\qquad$ $(4|6) = -0.1728$

$(3|6) = 1.1726$ $\qquad$ $(6|6) = 1.5441$

The susceptibility equations are

$$\chi_{\parallel} = 2NB \left[\frac{|(1|\mu_z|2)|^2}{\Delta_2} + \exp(-\Delta_2/kT) \left\{ - \frac{|(1|\mu_z|2)|^2}{\Delta_2} \right.\right.$$

$$\left. + \frac{|(2|\mu_z|5)|^2}{\Delta_5 - \Delta_2} \right\} + 2 \exp(-\Delta_3/kT) \left\{ \frac{|(3|\mu_z|3)|^2}{2kT} \right.$$

$$\left. + \sum_{i \neq 3} \frac{|(3|\mu_z|i)|^2}{\Delta_i - \Delta_3} \right\} + 2 \exp(-\Delta_4/kT) \left\{ \frac{|(4|\mu_z|4)|^2}{2kT} \right.$$

$$\left. + \sum_{i \neq 4} \frac{|(4|\mu_z|i)|^2}{\Delta_i - \Delta_4} \right\} + \exp(-\Delta_5/kT) \left\{ \frac{|(2|\mu_z|5)|^2}{\Delta_2 - \Delta_5} \right\}$$

$$\left. + 2 \exp(-\Delta_6/kT) \left\{ \frac{|(6|\mu_z|6)|^2}{2kT} + \sum_{i \neq 6} \frac{|(6|\mu_z|i)|^2}{\Delta_i - \Delta_6} \right\} \right] ,$$

$$\chi_{\perp} = 4NB \left[\sum_i \frac{|(1|\mu_x|i)|^2}{\Delta_i} + \exp(-\Delta_2/kT) \left\{ \sum_i \frac{|(2|\mu_x|i)|^2}{\Delta_i - \Delta_2} \right\} \right.$$

$$\left. + \exp(-\Delta_3/kT) \left\{ \frac{|(3|\mu_x|3)|^2}{2kT} + \sum_{j \neq 3} \frac{|(3|\mu_x|j)|^2}{\Delta_j - \Delta_3} \right\} \right.$$

APPENDIX IX (continued)

$$+ \exp(-\Delta_4/kT)\left\{\frac{|(4|\mu_x|4)|^2}{2kT} + \sum_{j\neq 4}\frac{|(4|\mu_x|j)|^2}{\Delta_j - \Delta_4}\right\}$$

$$+ \exp(-\Delta_5/kT)\left\{\sum_{i}\frac{|(5|\mu_x|i)|^2}{\Delta_i - \Delta_5}\right\}$$

$$+ \exp(-\Delta_6/kT)\left\{\frac{|(6|\mu_x|6)|^2}{2kT} + \sum_{j\neq 6}\frac{|(6|\mu_x|j)|^2}{\Delta_j - \Delta_6}\right\}\Bigg]$$

where

$$B^{-1} = 1 + \exp(-\Delta_2/kT) + 2\exp(-\Delta_3/kT) + 2\exp(-\Delta_4/kT)$$
$$+ \exp(-\Delta_5/kT) + 2\exp(-\Delta_6/kT)\ ,$$

and

$$i = 3,\ 4,\ 6$$
$$j = 1,\ 2,\ 3,\ 4,\ 5,\ 6\ .$$

In the susceptibility equations the energy spacing between the kth level and the ground level is represented by Δ_k and the numbers 1, 2, 3, 4, 5, 6 represent the A_1, T_1A_2, T_1E, EE, T_2A_1, and the T_2E levels, respectively.

LIST OF REFERENCES

1. Low, W., Paramagnetic Resonance in Solids (Academic Press Inc., New York, 1960).

2. McClure, D. S., Solid State Physics 9, 399(1959).

3. Van Vleck, J. H., The Theory of Electric and Magnetic Susceptibilities (Oxford University Press, London, 1932).

4. Griffith, J. S., The Theory of Transition - Metal Ions (Cambridge University Press, Cambridge, 1961).

5. Prather, J. L., Atomic Energy Levels in Crystals (U.S. Government Printing Office, Washington, 1961).

6. Wigner, E. P., Group Theory (Academic Press, New York, 1959).

7. Selwood, P. W., Magnetochemistry (Interscience Publishers, Inc., New York, 1956) 2nd ed.

8. Bates, L. F., Modern Magnetism (Cambridge University Press, New York, 1961), 4th ed.

9. Stout, J. W., and Griffel, M., J. Chem. Phys. 18, 1449 (1950).

10. Senftle, F. E., Lee, M. D., Monkewicz, A. A., Mayo, J. W., and Pankey, T., Rev. Sci. Instr. 29, 429 (1958).

11. Scott, R. B., Cryogenic Engineering (D. Van Nostrand Company, Inc., Princeton, N. J., 1959), p. 349.

12. Bunch, M. D., Powell, R. L. and Corruccini, R. J., NBS-CEL. Unpublished Data.

13. Stevens, K. W. H., Proc. Roy. Soc. A214, 237(1952).

14. Griffiths, J. H., and Owen, J., Proc. Roy. Soc. A213, 459 (1952).

15. Penrose, R. P., and Stevens, K. W. H., Proc. Phys. Soc. A63, 29(1950).

16. Wyckoff, R. W. G., Crystal Structures (Interscience Publishers, Inc., New York, 1948), Vol. 1.

17. Heiland, G., Mollwo, E., and Stöckman, F., Solid State Physics 8, 191(1959).

18. Weakliem, H. A., Phys. Rev. 36, 2117 (1962).

19. Pappalardo, R. and Dietz, R. E., Phys. Rev. 123, 1188 (1961).

20. Quade, C. R., The Paramagnetism of Crystals of Triply Ionized Vanadium, (Unpublished Masters' Thesis, Dept. of Physics, University of Oklahoma).

21. Brumage, W. H., Quade, C. R., and Lin, C. C., Phys. Rev. 131, 949 (1963).

22. Slater, J. C., Quantum Theory of Atomic Structure (McGraw-Hill Book Company, Inc. New York, 1960), Vol. II.

23. Condon, E. U., and Shortley, G. H., The Theory of Atomic Spectra (Cambridge University Press, Cambridge, 1959), pg. 77.

24. Ibid., 202.

25. Ibid., 177.

26. Ibid., 221.

27. Ibid., 48.

28. Prather, loc. cit., 3.

29. Title, R. S., Phys. Rev. 131, 2503(1963).

30. Kikuchi, C., and Azarbayejani, G. H., J. Phys. Soc. Japan 17, B-I, 453(1962).

31. Tinkham, M., Proc. Roy. Soc. A236, 549(1956).

32. Owen, J., Proc. Roy. Soc. A227, 183(1955).

33. Low, loc. cit., 101.

34. McClure, D. S., J. Chem. Phys. 36, 2757(1962).

35. Weakliem, H. A., and McClure, D. S., Suppl. J. Appl. Phys. 33, 347(1962).

36. Pryce, H. H. L., and Runciman, W. A., Discussions Faraday Soc. 26, 35(1958).

37. Zverev, G. M., and Prokhorov, A. M., JETP 13, 714(1961).

38. Rei, D. K., Soviet Phys. Solid State 3, 1606(1962).

39. Foner, S. and Low, W., Phys. Rev. 120, 1585(1960).

40. Fox, G., J. Phys. radium 12, 156(1951).

41. Siegert, A., Physica 4, 138(1937); Van der Handel, J., and Siegert, A., 4, 871(1937).

42. Low, loc. cit., 75.

43. Kemble, E. C., The Fundamental Principle of Quantum Mechanics (Dover Publication, New York, 1958), p. 394.

44. Estle, T. L. and DeWit, M., Bul. Amer. Phys. Soc. II, 6, 445(1961).
Estle, T. L. (Private Communication).

45. Pappalardo, R., Wood, D. L., and Linares, Jr., R. C., J. Chem. Phys. 35, 2041(1961).

46. Sanmann, E. E., Paramagnetism of Cobalt-Doped Crystalline Salts, (Unpublished Master's Thesis, Dept. of Physics, University of Oklahoma);
Sanmann, E. E., Brumage, W. H., and Lin, C. C., Bul. Am. Phys. Soc. II, 8, 118(1963).

47. Ham, F. S., Ludwig, G. W., Watkins, G. D., and Woodbury, H. H., Phys. Rev. Letters 5, 468(1960).

48. Brumage, W. H., Yarger, C. R., and Lin, C. C., Phys. Rev., (to be published).

49. Cohen, J., and Ducloz, J., J. Phys. radium 20, 402(1959).

50. Ayant, Y., and Thomas, J., Compt. rend. 248, 387(1959).

51. Ball, M., Garton, G., Leask, M. J. M., and Wolf, W. P., Proceedings of the VII International Conference on Low Temperature Physics (University of Toronto Press, 1961), p. 128.

52. Ayant, Y., Thomas, J., Cohen, J., and Ducloz, J., J. Phys. radium 22, 63S(1961).

53. Pappalardo, R., and Wood, D. L., J. Chem. Phys. 33, 1734 (1960).

54. Wood, D. L., J. Chem. Phys. 39, 1671(1963).

55. Selwood, P. W., Magnetochemistry (Interscience Publishers, Inc., New York, 1956), 2nd ed., p. 78.

56. Boakes, D., Garton, G., Ryan, D., Wolf, W. P., Proc. Phys. Soc. (London) 74, 663(1959); J. W. Carson and R. L. White, J. Appl. Phys. 31, 53S(1960).

57. Sievers, III, A. J., and Tinkham, M., Phys. Rev. 129, 1995(1963).

58. Brumage, W. H., Lin, C. C., and Van Vleck, J. H., Phys. Rev. 132, 608(1963).

59. Garber, M., Henry, W. G., and Hoeve, H. G., Cand. J. Phys. 38, 1595(1960).